

**NANOFABRICATION AND CHARACTERIZATION
OF ADVANCED MATERIALS AND DEVICES**

By

Viacheslav Manichev

A dissertation submitted to the

School of Graduate Studies

Rutgers, The State University of New Jersey In

partial fulfillment of the requirements

For the degree of

Doctor of Philosophy

Graduate Program in Chemistry and Chemical Biology

Written under the direction of

Eric Garfunkel

And approved by

New Brunswick, New Jersey

May, 2018

ABSTRACT OF THE DISSERTATION

Nanofabrication and Characterization of Advanced Materials and Devices

By VIACHESLAV MANICHEV

Dissertation Director:

Eric Garfunkel

The development of novel materials has been central to enabling technological change that has affected humankind in many positive ways, and a few negative ones. From the utilization primitive stone tools to the smelting of iron and other metals to the introduction of semiconductor devices we continuously bring new materials and devices into everyday life. Their introduction has been accelerating during the past century, in part because of our much more sophisticated understanding of the basic atomic scale nature of materials. Today, the development of new material requires that we fully understand their atomic composition and structure and the unique properties that they may hold: mechanical, electronic, magnetic, optical, etc. This understanding requires that we employ sophisticated atomic scale characterization techniques. Helium Ion Microscopy (HIM) is one such technique, a novel microscopy method introduced over the past decade that empowers researcher not only to image sample surfaces with sub-nanometer resolution but to directly probe insulating samples.

This thesis introduces the new technique of Helium Ion Microscopy and demonstrates its use in a few rather different applications. It also describes a new method that we developed to enable nanoscale elemental analysis.

Direct visualization of previously inaccessible insulating samples has enabled us to image the nanoscale effects of a newly discovered drug. A series of images offers a vivid set of evidence of restoration of ischemia damaged kidney structures in rats. In another study we proposed a new mechanism for the growth of coral calcium carbonate skeletons, where (in combination with several other analytical tools) Helium Ion Microscopy produced images not only of excellent scientific value but also of high aesthetic beauty as acknowledged by publications in Science, Nature, and the New York Times.

We have further helped the development of Helium Ion Microscopy by introducing a new method of *in-situ* elemental analysis. Based on a time of flight principle, our novel detector system is capable of providing compositional analysis of samples in addition to high-resolution imaging (essentially nano-scale Rutherford backscattering). Working in the 30 keV He⁺ energy regime, our time of flight detector system collects backscattered He particles, then by measuring the energy loss that occurs during the backscattering process we can identify the elements in the target. This is a substantially more sensitive and quantitative technique with higher spatial resolution compared to Energy Dispersive X-ray spectroscopy in SEMs, the most important established technique.

Acknowledgements

During my graduate career I was blessed to have not one, not two but three advisors who guided me with dedication and patience. I would like to thank Torgny Gustafsson who welcomed me in his lab and provided every opportunity to succeed. I am also indebted to Leonard Feldman for his continuous guidance and advice. I am grateful to Eric Garfunkel who first helped recruit me to Rutgers, and then later brought me into the GGF (Garfunkel, Gustafsson, Feldman) group, and advised me often during my years at Rutgers.

During my time in the exceptionally diverse GGF lab, I have met many people who mentored and helped me to learn vacuum techniques and instrumentation, ion beam physics, physical chemistry, surface and interface science and many more aspects of how to perform first rate research. I would like to thank Hang Dong Lee and Can Xu for extensively training me on Medium Energy Ion Scattering accelerator and Helium Ion Microscope. Yi Xu trained me on atomic layer deposition instruments and Gang Liu helped me understand device fabrication and measurements from the electrical engineer's perspective. Feixiang Luo, Aleksandra Biedron, Mengjun Li, Shinjae Hwang and Anders Laursen are wonderful and supportive group members. I would like to thank Ryan Thorpe and Sylvie Rangan for answering countless questions and always willing to help. I am grateful to Bill Schneider and Eric Paduch in the machine shop who built and modified much of my specialty instrumentations, Alexei Ermakov who's skills and knowhow brought many of my experiments to fruition, Albert Schultz and Damon Barbacci from company Ionwerks, who patiently and thoroughly worked with me on the time of flight system and with whom we successfully overcame numerous technical challenges, and Alexander Livernois and Margarita Rivers, two stellar undergraduates with whom I was lucky to work with on several

projects. I am also thankful to Hazel Szeto and Shaoyi Liu for educating me on nephrology and providing an opportunity to contribute to a medical discovery, and to Paul Falkowski and Stanislas Von Euw for a very exciting and well publicized collaboration on corals.

Finally, I would like thank my wife Alina and our whole family for the contentious support and encouragement throughout the years of graduate school.

Table of contents

Abstract.....	ii
Acknowledgements.....	iv
List of Figures.....	viii
List of Tables.....	x
List of Acronyms	xi
Chapter 1: Introduction.....	1
1.1 Helium Ion Microscopy	1
1.2 Lithography	4
1.3 Novel detector system for elemental identification.....	7
1.4 Imaging applications of helium ion microscope	9
Chapter 2: Background.....	11
2.1 Development of ion beam tools	11
2.2 Focusing ion beams.....	12
2.3 Kinematics.....	14
2.4 The helium ion microscope.....	16
Chapter 3: Time-of-Flight elemental analysis in HIM	22
3.1 Introduction	22
3.2 Background	23
3.3 Elemental identification efforts with the helium ion microscope	24
3.4 Rutgers time of flight system.....	25
3.5 Results.....	31
3.6 Current Performance of the Rutgers ToF scheme	35

3.7	Future work.....	37
3.8	Conclusions	38
Chapter 4: Mitochondria protection after acute ischemia prevents prolonged upregulation of IL-1b and IL-18 and arrests CKD		39
4.1	Introduction	39
4.2	Results.....	45
4.3	Discussion	54
4.4	Concise Methods	59
Chapter 5: Biological control of aragonite formation in stony corals		63
5.1	Introduction	63
5.2	Features common to all stony corals.....	64
5.3	Spatial distribution of the SOM and Orientation of the skeletal fibers.....	66
5.4	Chemical heterogeneity in the mineral phase.....	68
5.5	Relation between the initial mineral deposits and the SOM in the COCs	70
5.6	Detection of carbonates at the mineral-organic interfaces	70
5.7	Investigation into the mineral-organic interface	72
5.8	Precipitation pathway of coral aragonite	76
5.9	Transformation from ACC to aragonite	78
5.10	Chemical composition of the initial mineral deposits	80
5.11	Conclusions	84
Citations		86

List of Figures

1.1	Interaction volume simulations of electron and helium beams.....	2
1.2	SEM cross section of silicon sample implanted with He.....	3
1.3	Free standing graphene nanoribbon	5
1.4	10 nm lines made by exposing Sn based photoresists with 30 keV He	6
1.5	Schematic of the Rutgers ToF system.....	8
1.6	Proof of principle ToF spectrum	9
2.1	Trajectories' lengths of backscattered particles.....	15
2.2	Scheme of the HIM column	16
2.3	Simulation of the total stopping power for electron and He	18
2.4	Simulation of Ion-induced Secondary electrons.....	19
2.5	Simulation of electron-induced Secondary Electrons.....	20
3.1	Sample RBS spectrum	26
3.2	Commercial depleted Si detector from Ortec	26
3.3	Secondary Electron Detector	28
3.4	Microchannel plates in chevron orientation	28
3.5	Position Sensitive Detector (PSD)	29
3.6	Scheme for position determination of the ion hit.....	30
3.7	ToF analysis of hafnium oxide stack	33
3.8	Dose dependence study of Pt	34
3.9	Beam spot size vs area scanned.....	34
3.10	Analysis of the Pt peak.....	35
3.11	EDX analysis of the Pt sample	37
4.1	Progression of interstitial fibrosis and glomerulosclerosis	40

4.2	Reduction of inflammation after acute renal ischemia	41
4.3	Reduction of endothelial injury after acute ischemia	42
4.4	Glomerular capillary compression and damage	44
4.5	Podocyte stress after acute ischemia	46
4.6	Podocyte foot processes after acute ischemia	48
4.7	Ischemia-induced mitochondria damage in podocytes.....	51
4.8	Persistent upregulation of autophagy in podocytes.....	52
4.9	Mitophagy in proximal tubules after acute ischemia	54
4.10	Mitochondria-associated membranes in proximal tubules.....	55
4.11	Mitochondrial integrity and inflammasome activation	56
5.1	Morphological skeletal features common to all stony corals.....	65
5.2	Structural and chemical characterization of the centers of calcification	67
5.3	Images of organic material in a COC.....	69
5.4	Spatial correlations between proton and carbon species in coral skeleton.....	73
5.5	Observations of the initial mineral deposits in coral skeleton	77
5.6	Images of the trabecula units	79
5.7	Observation of an incremental growth line of the mineral phase	81
5.8	Images of the crystal growth process	82
5.9	Variations in the chemical composition across the trabeculae	83
5.10	Coral aragonite crystal	83
5.11	A working model for biomineralization in stony corals	85

List of Tables

2.1	Calculated electromagnetic rigidity ratios.....	13
4.1	Experimental study groups	39

List of Acronyms

Å	Ångströms
ACC	Amorphous calcium carbonate
AKI	Acute kidney injury
ATP	Adenosine triphosphate
BSE	Backscattered electron
CDK	Chronic kidney disease
CLM	Cathodoluminescence microscopy
COCs	Centers of calcification
CP	Cross polarization
CRM	Confocal Raman microscopy
DAMPs	Danger-associated molecular patterns
dCRA	Deposits of Centers of Rapid Accretion
DIC	Dissolved inorganic carbon
EBSD	Electron backscatter diffraction
EDX	Energy-Dispersive X-ray spectroscopy
EELS	Electron energy-loss spectroscopy
EMZ	Early mineralized zone
ER	Endoplasmic reticulum
FIB	Focused Ion Beam
HIM	Helium Ion Microscope
keV	Kilo electron volts
MeV	Mega electron volts
MCPs	Microchannel Plates

mg-ACC	Magnesium-rich Amorphous calcium carbonate
NLR	Nod-like receptors
NMR	Nuclear magnetic resonance
OMM	Outer mitochondrial membrane
PIXE	Particle Induced X-Ray Emission
PLM	Polarized light microscopy
PMMA	Poly(methyl methacrylate)
PR	Photoresist
PSD	Position sensitive detector
RBS	Rutherford Backscattering Spectrometry
ROS	Reactive oxygen species
SAED	Selected area electron diffraction
SE	Secondary electrons
SED	Secondary electron detector
SEM	Scanning Electron Microscopy
SIMS	Secondary Ion Mass Spectrometry
SOM	Skeletal organic matrix
STIM	Scanning Ion Transmission Mode
TDC	Time to Digital Conversion
TEM	Transmission Electron Microscopy
ToF	Time-of-Flight
UUO	Unilateral ureteral obstruction
WDS	Wavelength dispersive X-ray spectroscopy
XPS	X-ray photoemission spectroscopy

Chapter 1

Introduction

1.1 Helium Ion Microscopy

“If Moore’s law continues, electronic devices will consume more than half the world’s energy budget within 20 years. To prevent that, we need a fundamentally new material”¹. While this statement refers specifically to semiconductor devices used in computing and telecommunications, the need for new materials extends well beyond that area. Solar energy conversion has already benefited immensely from advances in silicon processing and clever device fabrication, mainly learned from the electronics industry. A new class of hybrid (organic/inorganic) perovskites materials are showing efficiency rates competitive with silicon solar cells². Biocompatible and bioactive materials are revolutionizing medicine by creating more durable joint replacements³ and glucose-measuring contact lens sensors that change color in response to blood sugar levels⁴. Optimization of new material and device (often nano-scale) now requires that researchers employ a complementary set of powerful characterization tools and techniques. In order to create more sophisticated materials researchers are often required to work in ever decreasing dimensions (i.e. Moore’s rule)⁵. To improve our ability to see and understand at the atomic scale we have to continuously hone our analytical tools and characterization methods to achieve higher spatial, time and energy resolution, greater sensitivity and also introduce new capabilities to existing instruments.

The Helium Ion Microscope (HIM) is one of the latest additions to the ion beam and microscopy toolbox. HIM utilizes He ions (we work at ~30 keV) capable being focused down to a small spot (a few Ångströms in diameter). Upon interacting with the sample, secondary electrons (SEs) are emitted, detected and counted. By rastering the ion beam across the sample, one can obtain images of sample surfaces. Among the advantages of the HIM are a probe as small as 3 Å in diameter, a much larger depth of focus when compared to SEM and the all but unique capability to image non-conducting samples without a deposited metal overlayer.

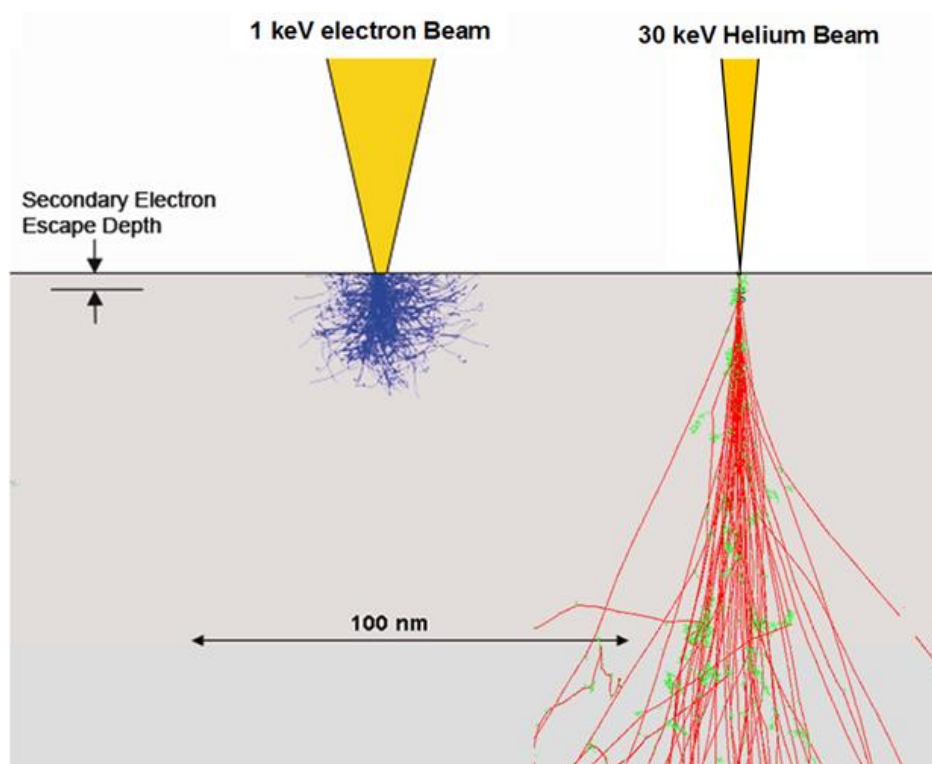


Figure 1.1 Interaction volume simulations of electron and helium beams⁶

Similarly to SEM imaging detection, secondary electrons (SEs) are produced in the HIM and then normally collected by a Everhart-Thornley detector⁷. HIM technology has a number of advantages over SEM: significantly better contrast ratio due to the higher SE yield per ion, larger depth-of-focus due to considerably smaller convergence angle of the beam (Figure 1.1), the ability

to image insulators via electron flood gun charge neutralization, and *in situ* sample modification by native He and Ne ion milling or by Ga ions upon introducing an additional ion gun. These advantages are beginning to be recognized by the community and have started to generate tremendous impact across several scientific fields: medicine⁸, marine biology⁹, electrical and device engineering¹⁰, materials science¹¹, chemistry¹² - the list is growing.

Upon interaction with the sample, He ions provide positive charge which is normally dissipated if the sample is conductive. Most of the energy of the incident ions is released as heat in the sample, with some lost to the kinetic energy of backscattered or sputtered ions or neutrals, or to emitted electrons. When dealing with insulating materials, the problem of charging arises. A large concentration of positive charges on the surface of a material being imaged can diminish the secondary electron yield. Therefore, insulating areas appear black during imaging.

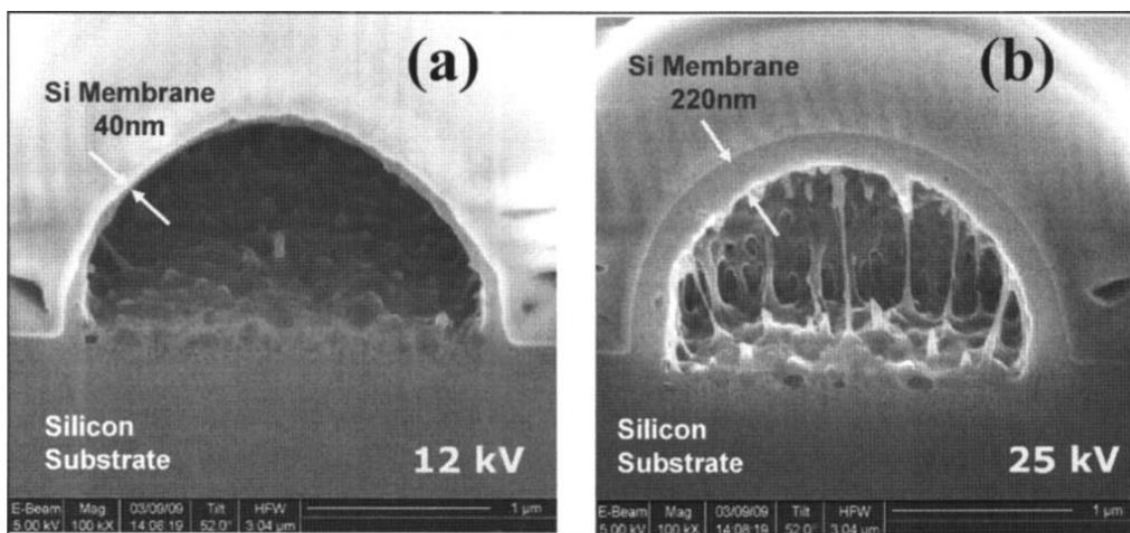


FIGURE 1.2 SEM cross section of silicon sample implanted with a He ion dose of 1.3×10^{18} ion/cm² at beam energies (a) 12 keV and (b) 25 keV¹¹

In an SEM, insulating materials are often coated with a thin conductive film of gold, platinum or carbon to neutralize any charge buildup. However, even a thin adlayer can hide important functional features and in some cases may completely conceal small objects. In HIM

the charging problem is mitigated with the addition of a low energy electron flood gun, rastered alternately with the He beam. This effectively neutralizes positive charge and makes it possible to obtain clear, high-resolution images of insulating objects such as oxides, polymers and biological samples without surface modification.

While imaging with HIM, it is important to consider also He interactions with the atomic nuclei in the sample. Even though the probability of He transferring enough energy to eject (sputter) atoms from the sample is relatively low, damage to the sample can be observed, especially at higher doses. Hence, it is essential to keep in mind the balance between clear, high-resolution images (increased He ion dose) and minimizing sputtering, as well as He implantation effects (Figure 1.2)¹¹.

1.2 Lithography

In some cases, seemingly deleterious the ion-solid nuclear interactions displacing atoms can be utilized to the benefit of the researcher. For instance, by delivering beams able to generate atomic displacements to predetermined areas, patterns such as words, images or even functional devices can be generated.

Ion milling is one approach to lithography in which an energetic beam of atoms impinges on the surface of a sample and sputters away material. This approach is the basis behind Focused Ion Beam (FIB) milling. Conventionally, FIB utilizes a beam of gallium ions with a relatively large beam spot size (~ tens of nanometers in diameter). Advantages of using a gallium beam include the comparatively high speed of milling due to the high Ga mass, the relative ease of generating Ga ions, and the availability of commercial equipment, making it a well-established technique with decades of presence on the market. However, for delicate modifications or chemically active

surfaces, Ga is not an ideal solution as the implantation of Ga can react with the material forming new compounds and introduce unwanted chemical properties to the sample.

HIM offers sub-nanometer He and nanometer Ne beam probes for milling and imaging of sample surfaces. Noble gasses are chemically inert and do not react with the target. A significantly smaller probe size (0.3 nm) opens up opportunities in nanostructure fabrications such as graphene nanoribbons (Figure 1.3), Josephson junctions¹³, and plasmon resonators¹⁴. However, He and Ne will not replace Ga and other heavy ion beams since they are relatively light atoms and have low milling speeds. One can draw a comparison to the sandpaper grit sizes, where a heavy metal beam acts as rough and fast abrasion, then a neon beam is used to engrave finer features and finally a Helium beam is used for fine polishing of the structure with nanometer precision.

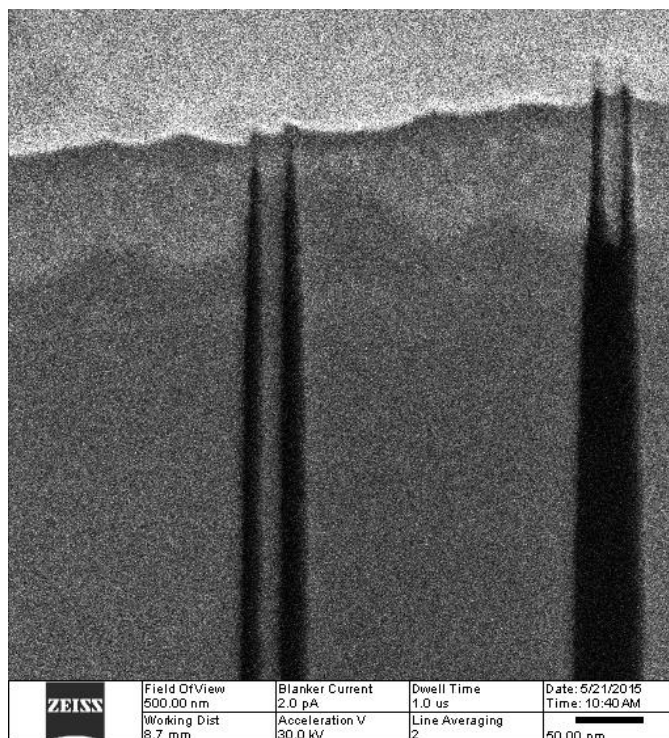


FIGURE 1.3 Free standing graphene nanoribbon 20 nm wide (left) with a gold electrode (top) and a broken ribbon (right)

A helium beam can also be used to expose photoresist (PR). Thus similar to e-beam photolithography, we can utilize conventional photoresists and a HIM beam to produce intricate

high resolution patterns. An advantage of He ions compared to electrons is the significantly lower dose needed for exposure. For the commonly used resist Poly(methyl methacrylate) or PMMA, we need only a single He ion per nm^2 to effectively expose the PR^{12, 15-16}. Such sensitivity is an order of magnitude higher than that obtained with electrons, although in some cases the statistical uncertainty associated with such a high sensitivity per ion can require a high dose. The significantly higher spatial resolution of the He beam can also produce much finer features. In our laboratory, we routinely achieve 10 nm lines^{12, 16} (Figure 1.4).

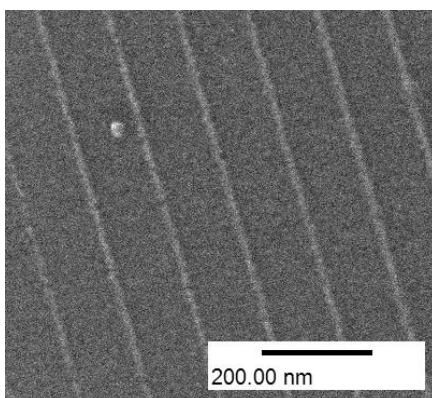


Figure 1.4 10 nm lines¹⁶ made by exposing Sn based photoresists with 30 keV He

Ion beam induced deposition is another capability of the HIM and has also been applied in our laboratory. This method requires a flow of a chemically reactive vapor (usually an organometallic species) near the sample and uses the kinetic energy of the beam to dissociate the carbonyl ligands and deposit metal on to the sample. By rastering the beam we can control the amount and position of new features thus generating patterns on the sample.

These new lithographic techniques imply a powerful material modification tool where samples can be modified in a highly controlled manner.

1.3 Novel Detector System for Elemental Identification

Elemental analysis of materials by alpha particles (He nuclei) or protons is a very mature field. Rutherford Backscattering Spectrometry (RBS) started with experiments done by Geiger and Marsden under the guidance of Rutherford at the beginning of the 20th century. Today we usually backscatter He or H ions at energies ranging from hundreds of thousands electron volts (keV) to a few million electron volts (MeV). At this range of energies, the ion-sample interaction can be described as a classical two body collision and the backscattered ion energies are straightforward measures of the masses and concentrations of the individual atoms in the target. Depleted silicon detectors or electrostatic detectors can collect the backscattered particles and provide sufficient energy resolution to separate signals from different elements. However, for projectile energies of a few tens of keV (the range at which Helium Ion Microscopes operate) standard detectors fail to produce enough energy resolution and/or have limited collection efficiencies. Therefore, we have designed and built a unique time-of-flight (TOF) detection system that successfully performs elemental analysis in the 30 keV regime designed for operation with the HIM.

Our ToF system is based on a start signal associated with the emission of secondary electrons originating from an impinging He ion (essentially instantaneous with the arrival of the projectile) and a stop signal from the detection of the actual backscattered He ion (Figure 1.5). By measuring the time delay between the start and stop signals over a known path length we obtain the energy of the backscattered He ion, which, in turn, yields the mass of the sample atom associated with the scattering event, hence elemental identification.

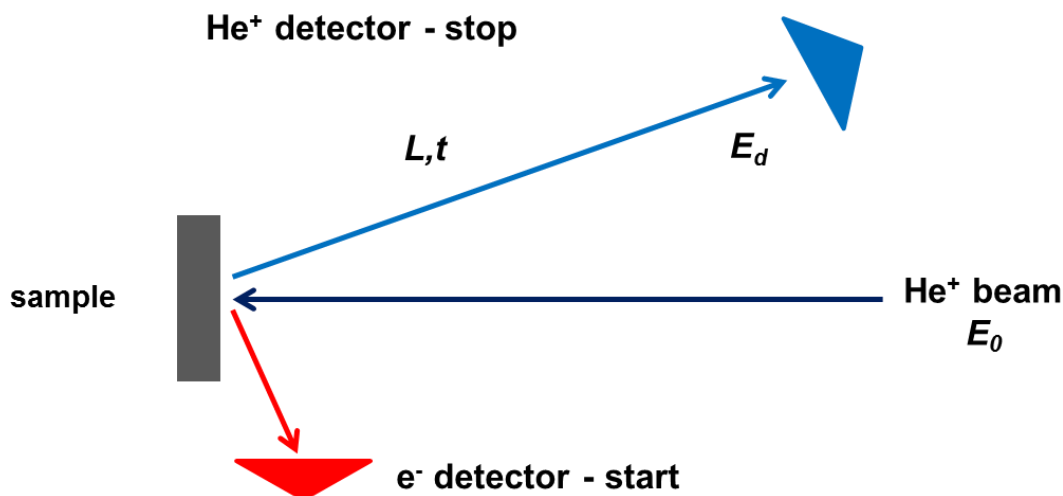


FIGURE 1.5 Schematic of the Rutgers ToF system. A steady He^+ beam (less than a 1 pA current) is impinging on the sample producing SEs and backscattering events, both collected by corresponding detectors.

For the start signal, the system employs a customized set of electronic lenses, which first accelerate the secondary electrons from the sample and then focus the resulting beam onto a stack of two microchannel plates. The electronics are specifically designed to handle the high incidence rates of order $10^5/\text{s}$ to $10^7/\text{s}$. The lens system is also intended to minimize electron path length dispersion to retain high time resolution. A crucial advantage of using a He beam is that the secondary electron yield per incident He ion is larger than one so that essentially every backscattered event will also generate SEs.

Straightforward ion scattering kinematics for our ion detector indicates that a time resolution of 1 ns with a 130 mm flight path will yield an energy resolution of 1 keV. The resolution can be improved further with a longer flight path. The current resolution would permit mass analyses that would separate a heavy metal from silicon, but further improvements (discussed in the later sections) will allow for separation of $^{69, 71}\text{Ga}$ from ^{75}As , and ^{12}C from ^{13}C . This would correspond to ~ 1.0 nm depth resolution in silicon, better in higher Z materials. We note that the random count rate is not directly determined by the time resolution but rather the time limits of

the Time-to-Digital Converter (TDC). As such, real to random rates of better than 10:1 have been demonstrated (Figure 1.6).

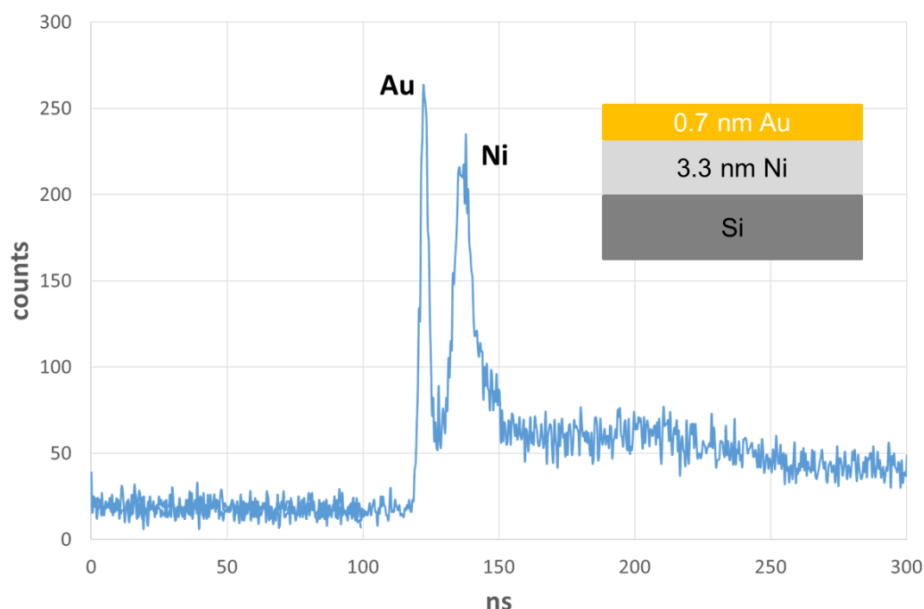


FIGURE 1.6 First proof of principle of the Rutgers-Ionwerks ToF spectrum for a 0.7 nm Au film on 3.3 nm of Ni on an Al_2O_3 substrate taken with a $10\ \mu\text{m}$ beam spot size and uncorrected for finite detector size and kinematic effects.

1.4 Imaging Applications of the Helium Ion Microscope

The primary application of the HIM is to generate high-spatial-resolution images of sample surfaces. Improved secondary electron (SE) yield when compared with SEM and the ability of imaging insulators without a conductive overcoating (discussed in section 2.3), allow for faster and more detailed imaging of samples. Biological samples require sophisticated preparation protocols¹⁷ in order to prepare the material for the high vacuum environment of the SEM imaging chamber. This is also true for the HIM as it operates at $\sim 1\text{e-}7$ torr in the imaging chamber. However, even after water substitution with formalin, common protocols demand a conductive layer to be deposited for standard SEM imaging. The deposition is usually done by evaporating a hot metal or alloy onto the sample, which unfortunately may create stress and

deform sensitive materials and also generate a non-uniform overlayer that masks small features. With Helium Ion Microscopy, the coating step is completely omitted and the researcher has unfettered access to the sample surface.

Chapter 4 demonstrates new evidence of successful treatment of kidney damage in rats with a recently developed drug. During this project I worked closely with the drug discovery team at Weill Cornell Medicine (a medical school) optimizing the sample preparation protocol and conducting exhaustive imaging of kidney tissues. We observed pronounced morphological changes at the submicron level in the kidney structure that correspond to degradation and healing of tissues due to damage and treatment with new medication. Chapter 4 is based on reference [8].

Chapter 5, based on reference [9], describes a previously unexplained mechanism of calcification of a calcium carbonate coral skeleton. The HIM played a central role by providing an unprecedented topological view of the centers of calcification and the morphological variations in skeleton structures. Obtained images were used as a platform for further spectroscopic analyses with solid state Magnetic Nuclear Resonance, EDX and spatially resolved Raman scattering. HIM images from this project were published in the New York Times¹⁸ and selected for Nature's short list of sharpest science shots¹⁹.

Chapter 2

Background

2.1 Development of ion beam tools

As of this writing (spring 2018), Carl Zeiss Microscopy holds the world record for energetic He⁺ beam spot size. Their commercially available Helium Ion Microscope routinely produces a probe of about 0.3 nm in diameter generating spectacular images as demonstrated in later chapters. However, the journey to the 0.3 nm beam was not a quick or obvious one.

Conventional RBS MeV instruments usually operate with a beam spot size on the order of hundreds of micrometers. In a 1998 paper, Watt et al²⁰ reviewed the state of the art of alpha particle probes, citing spot sizes ranging from 50 to several 100s of nanometers. The highest resolution reported was 50 nm for 2 MeV alpha particles in the MARC microprobe facility at the University of Melbourne. “These claims, however, have been undermined not only by the lack of a common and generally accepted resolution standard [but] also by the lack of a consistent approach between groups regarding a recognized method of beam spot measurement”. To conclude: The method to determine the resolution and therefore the beam spot size varies between techniques and operators. In the case of RBS and PIXE (Particle Induced X-Ray Emission), one group reports²⁰ that a beam was scanned across a sample with metallic features of various sizes. Resulting maps were analyzed, and a beam spot size was extracted by Gaussian fitting. A resolution of 400 nm was reported. In another study²⁰ with energetic protons in the Scanning Ion Transmission Mode (STIM), a beam was passed across a hole of about 1 μm in diameter from which the beam size was determined to be 130 nm.

2.2 Focusing Ion Beams

Virtually every instrument that generates focused particle beams relies on magnetic and electrostatic lenses. These lenses are usually fashioned in two configurations: quadrupole or disk (toroid). The choice of electrostatic or magnetic lens is usually based on the particle used and its energy range. Magnetic lenses are mainly used to focus 20 - 200 keV electrons and light ions. Electrostatic lenses are widely employed with heavier particle beams starting from protons and alpha particles. Quadrupole lenses are usually more suited for heavier charged particles accelerated to higher energies and can be either magnetic or electrostatic.

To understand how each type of lens is selected let us consider the electromagnetic case and calculate magnetic rigidities (resistance to deflection) of selected charged particles. The force on the particle is calculated via the Lorentz equation:

$$F_B = Bqv \quad (2.1)$$

for a particle with charge q , non-relativistic velocity v , and mass m in a magnetic field B . Then, the acceleration toward the center or the focusing action can be written as:

$$Bqv = \frac{mv^2}{\rho} \quad (2.2)$$

where ρ is the radius of the lens. From here we can find the rigidity of the beam $B\rho$, in units of momentum per unit charge:

$$B\rho = \frac{mv}{q} \quad (2.3)$$

Or for the nonrelativistic energy of the particle T:

$$B\rho = \frac{\sqrt{2mT}}{q} \quad (2.4)$$

Now we can compare the magnetic rigidity of 30 keV electrons, protons, He⁺, Ne⁺, and Ga⁺.

Particle @ 30keV	e ⁻	p ⁺	He ⁺	Ne ⁺	Ga ⁺
Relative electromagnetic beam rigidity	1	43	86	192	356

Table 2.1 Relative electromagnetic rigidity ratios based on the formula 2.4 for particles accelerated to 30 keV

By examining table 2.1, we can immediately see how much stronger a magnetic field is required to focus high-mass particles effectively. Even though it is possible to build strong magnetic lenses (they usually reduce chromatic aberrations better than electrostatic ones), such lenses would be very large in size and weight and prohibitively expensive outside large particle accelerators.

A similar exercise can be performed for electrostatic rigidity by starting with the electric force equation:

$$F_E = qE \quad (2.5)$$

$$qE = \frac{mv^2}{\rho} \quad (2.6)$$

$$qE = \frac{2T}{\rho} \quad (2.7)$$

Immediately we notice that electrostatic rigidity does not depend on the particle mass, only on the charge (and energy). This means that only moderate electrostatic fields are required

for effective focusing. Zeiss, therefore, installed two electrostatic lenses in the HIM: a condenser and an objective lens, located near the source and the sample respectively.

However, even with an electrostatic lens, a conventional liquid Ga source FIB may generate a probe several nanometers in diameter at best. One, and perhaps the most important, reason for this is the large size of the source (emittance) – hundreds of nanometers to a few microns in diameter. For conventional noble gas sources, the problem is even worse since gases are usually ionized via an electron, or radio frequency, generated plasma, therefore creating an even larger ion source.

The beam emittance is a property determined by the product of momentum and position of the particles. In this way, a beam of particles in three dimensions forms a six-dimensional property, the emittance, preserved throughout the beam trajectory. An understanding of high beam emittance²¹ starts by recalling Liouville's theorem which states that the beam emittance is preserved even after manipulation (lensing, aperturing, etc.). The implication is that a beam with a large emittance (large source) cannot be focused to a small beam spot. The HIM, with its single atom source (discussed in section 2.4) provides a very small emittance and hence optimum focusing.

2.3 Kinematics

The energy transfer in elastic collisions between atoms is very well understood and has been employed in RBS for many years. Equations 2.8 and 2.9 describe the kinematics of the probing particle in an elastic collision with a target atom. The energy transfer is accounted for by the kinematic factor (k) below, where E_0 is the initial energy of the projectile and E_1 is its energy after the collision (the backscattering event). This energy loss depends on the masses of the atoms involved (m_1 being the projectile and m_2 the target) and θ is the backscattering angle.

Therefore in order to calculate the mass of the target atom, one has to know the energy of the probing beam and the position of the detector relative to the sample and probing beam.

$$E_1 = k \cdot E_0 \quad (2.8)$$

$$k = \left(\frac{m_1 \cos \theta_1 \pm \sqrt{m_2^2 - m_1^2 (\sin \theta_1)^2}}{m_1 + m_2} \right)^2 \quad (2.9)$$

As described above, it is essential to understand the geometry of the detection system responsible for the collection of the backscattered particles well. In case of a time of flight set up, such knowledge is needed not only to account for the kinematic spread due to the variation in backscattering angles but also to account for the time variation due to differences in the lengths of the trajectories (Figure 2.1). This phenomenon is especially important when using flat large area detectors. However, both of these variations can be accounted for in the post processing if the detector has position sensitivity.

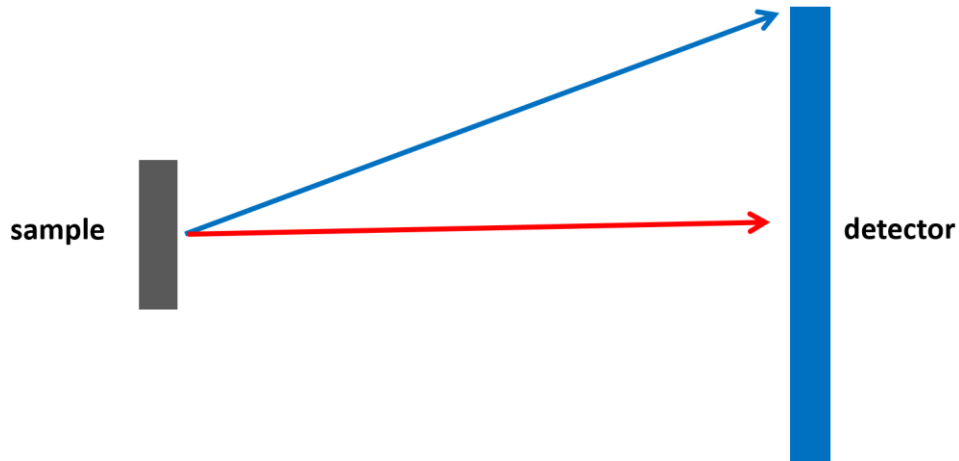


Figure 2.1 Variations in trajectory lengths of backscattered particles will introduce uncertainty in the time of flight measurement. In our case the time it take for 28 keV He ion to reach the center of the detector is about 1.5 ns shorter than reaching the edge.

2.4 The Helium Ion Microscope

The key components of the helium ion microscope are the ion source, the extractor electrode, the ion optics, and the secondary electron detector (Figure 2.2).

For a long time the large emittance of field emission ions sources prevented microscopists from focusing ion beams to small spots, thus making He Ion based microscopy impractical. However, one solution was developed in 2000 – 2005 period by the ALIS Corporation (a small startup in the Boston area, now part of Carl Zeiss Microscopy). To create such a source, a thin metallic wire had to be sharpened to atomic dimensions. Sharpening was done by manipulating the stability of certain facets on a crystalline material using chemical etching, heating and electrostatic fields using an undisclosed proprietary process. The source they invented had a diameter equivalent to a single atom, $\sim 3 \text{ \AA}$.

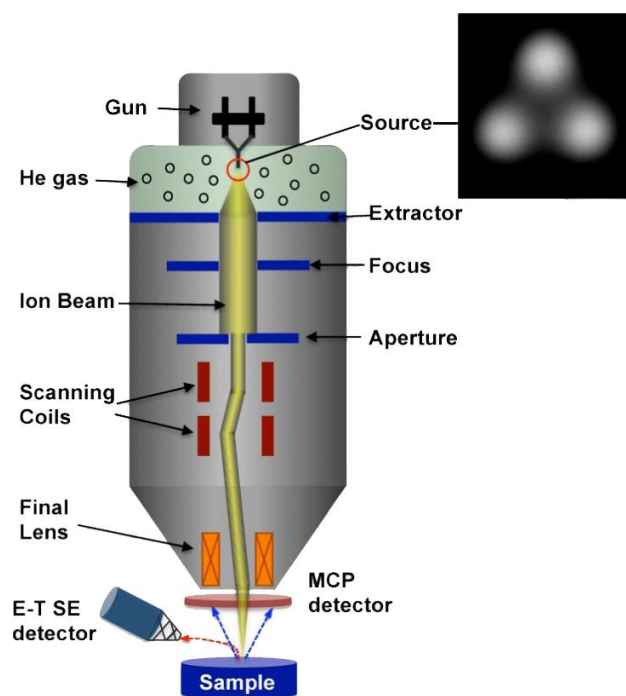


FIGURE 2.2 Scheme of the HIM column²²

The ion source therefore consists of a very sharp monocrystalline metal needle (the exact composition is a closely guarded trade secret but is widely believed to be W or a W alloy) with the

tip of the needle ~ 100 nm in diameter and a further tapered with only three atoms (referred to as a trimer) at the very end. The three-atom configuration allows greater stability and consequently longer operation times relative to that of a single atom. The needle is cooled with solid nitrogen to ~ 75 K. This serves two purposes: it reduces vibrations in the source, as they may result in blurring of the image, and also reduces background gases by acting as a cold trap. The needle is connected to a positive high voltage power supply tunable from +5 keV to +30 keV. The high voltage applied to the atomically sharp source generates a very high electric field (~ 4.4 V/Å) in the area of the trimer resulting in field ionization of gas molecules. The field ionization potential of He is the highest of any element, resulting in background gases being field ionized further away from the tip and then accelerated away, therefore, protecting the source from contaminants, and resulting in a longer tip lifetimes (up to 3 weeks in our lab). When operating with Ne, due its lower ionization potential, the electric field near the source has to be reduced to preserve the optimal size of the source, therefore, contaminants in the vacuum will be ionized closer to the tip with higher probability of damaging it, significantly shortening source lifetimes.

Right below the tip is the grounded metal electrode – the extractor. Upon ionization, an ion is instantly accelerated away from the tip through a hole in the extractor electrode. As the source ends in three atoms, three beams result. To select a single beam the column is physically tilted, so that only one beam is passing through the extractor and the alignment optics, preserving an ultimate beam source essentially the size of a single atom. Further below the beam is aligned, focused and rastered on the sample.

Once reaching the sample, the incident He ions interact mainly with electrons in the substrate. Since the He mass is much larger than that of the electrons, the He ions do not deviate much from the initial trajectory creating a very small interaction volume during the first 10 nm of material compared to the incident electrons in an SEM (Figure 2.3). Some electrons are ejected

from the sample (secondary electrons SE) and attracted to and counted by the detector. The SEs have energies sharply peaked at just a few electron volts²³, and the SE emission probability is, as will be discussed below, larger than in an SEM.

As the He ion has significantly higher momentum when compared to an electron of similar acceleration, we expect He to deposit a notably higher amount of energy onto the sample. Equation 2.10 describes the production of secondary electrons by incident charged particles. Below, n is the number of secondary electrons and dE/dx is the rate of energy loss as particles travel through the sample. Electrons (secondary) emitted with trajectories directed away from the sample (into the vacuum) originate from a mean depth represented by λ (usually ~ 5 -10 nm or less. The average energy of these secondary electrons described by ϵ can be from 0 to 20 eV.

$$n \approx \left(\frac{dE}{dx} \right) * \frac{\lambda}{\epsilon} \quad (2.10)$$

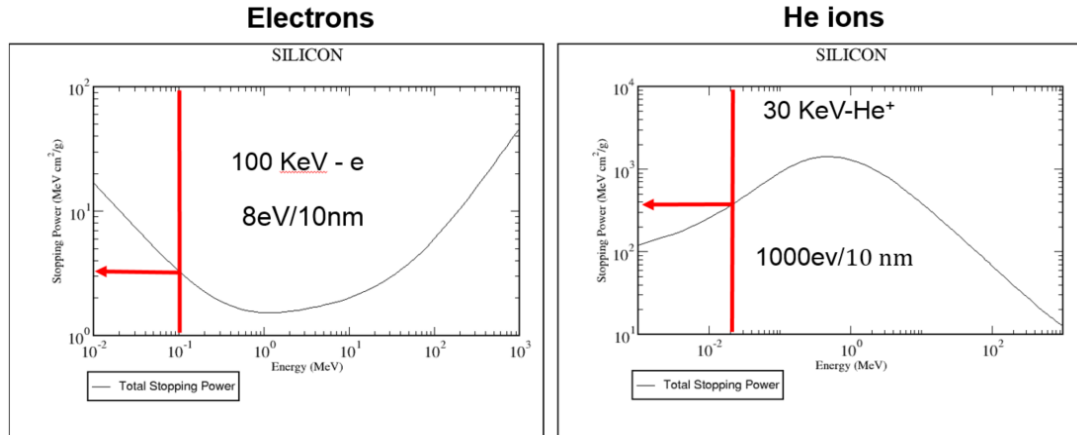


Figure 2.3 Simulation of the total stopping power for electron and He obtained from NIST²⁴. The red arrow indicates the approximate energy of the particle corresponding to the label within each of two graphs.

The amount of energy deposited by a particle is related to the number of SEs ejected from the sample. For example, using the IONiSE Monte Carlo program, David Joy²⁵ demonstrated that

the number of secondary electrons generated from the He beam (Figure 2.4) is significantly higher than SEs generated by an SEM beam in the first 10 nm (Figure 2.5).

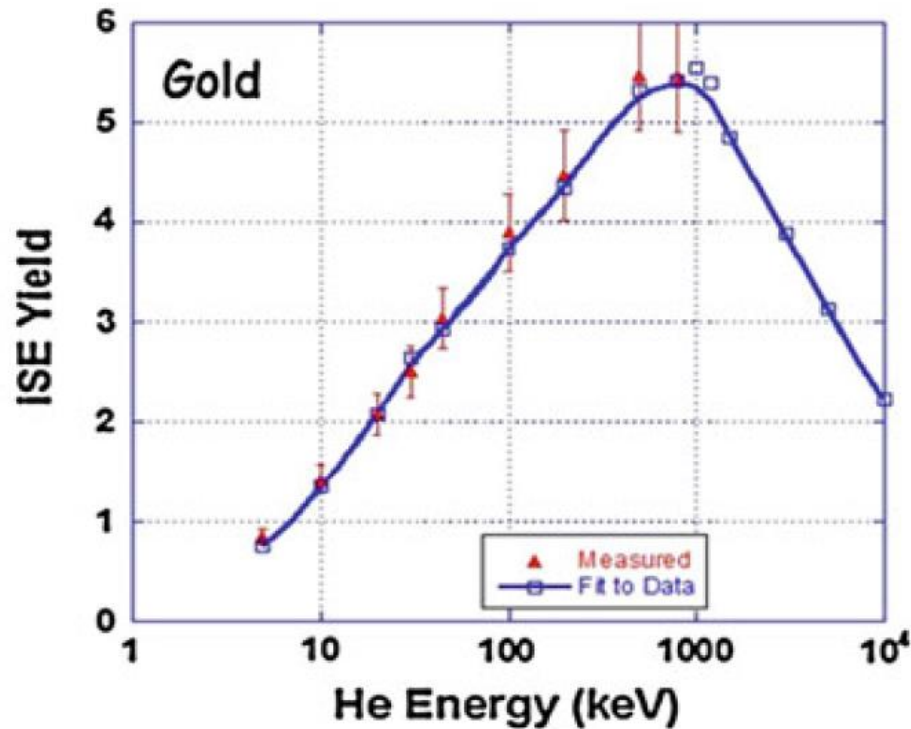


Figure 2.4 IONISE Monte Carlo simulation of Ion-induced Secondary electrons (ISE) as a function of He ion energy²⁵.

When comparing HIM to conventional SEM, one can also understand that the latest trend in SEM technology is to use lower primary beam energies. As the energy of the electron is reduced, its stopping power is increased; therefore more energy is deposited in the top layer of the sample. This increases the number of SE that can be collected by the detector (Figure 2.5). Furthermore, a lower incident electron energy brings the ratio of the number of electrons excited deep in the sample to those ejected (SE) closer to one, reducing charge accumulation. Such an approach has become increasingly important in the SEM community for imaging insulating materials.

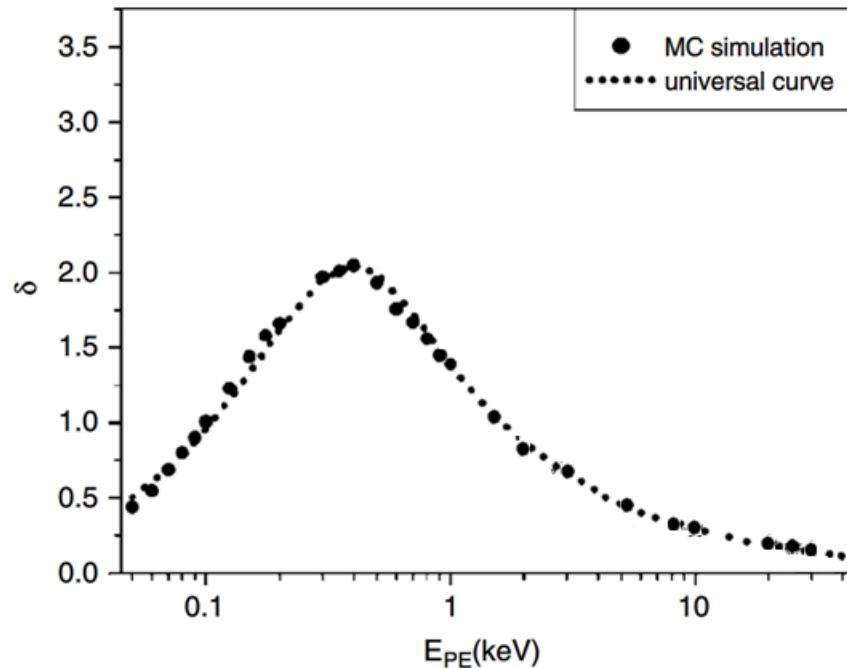


Figure 2.5 Monte Carlo simulation of electron-induced Secondary Electron (ISE) yield (δ is the ratio of number of electrons impinging onto the sample vs. electrons ejected) as a function of energy of the primary beam on an Al substrate ²⁶. To achieve a 1 to 1 ratio for electron in vs. SE out, many modern SEMs are capable of operating at < 1 keV.

One of the several advantages of HIM relative to SEM is the ability to image insulators without a conductive overlayer. Virtually any vacuum compatible samples can be imaged without commonly used gold, platinum or carbon adlayers. HIM utilizes positively charged He ions to probe the samples. Due to the very high ionization potential of He, it tends to fill its own vacant 1s shell first; then while traveling through the sample, He transfers some of its momentum to the sample electrons. Some of the excited electrons gain enough energy to escape into the vacuum as SEs. These SEs are then collected by the detector and used in the formation of the image. However, if the sample is an insulator, continuous deposition of positive charge will result in the accumulation of that charge in the imaging area and significantly diminished production of SEs and therefore inhibiting image formation. To alleviate positive charge accumulation, Zeiss introduced an electron flood gun that turns on between He beam scans and showers the sample

with low energy (~ 700 eV) electrons. As the image formation is usually done in lines or frames and requires many scans to build enough statistics for a clear image, the flood gun is used intermittently between line or frame scans of the primary beam. On the other hand, SEM deposits electrons onto the sample therefore negatively charging the surface. In insulators, this phenomenon translates to too many electrons ejected from the sample and saturation of the detector. In principle, a flood gun with positive ions (perhaps low energy noble gas ions) could be implemented in the SEM, but so far this has not occurred.

Chapter 3

Time-of-Flight Elemental Analysis in HIM

3.1 Introduction

The Helium Ion Microscope (HIM) is the first successful He probe scanning microscope. Today (2018), there are close to 100 instruments operating across the globe. As discussed above, the HIM carries a number of advantages for imaging over conventional scanning electron microscopes (SEMs). For example, the probe spot size of a state of the art HIM is on the order of 3 Ångströms, and is thus capable of providing excellent spatial resolution. Additionally, HIM is able to image insulating samples directly—without deposition of a conductive adlayer—opening up access to the surfaces of insulating materials. For many in the community, particularly those studying biological samples, the ability to image without a masking overlayer presents the opportunity to explore features heretofore incapable of being imaged. Several other properties such as significantly enhanced focal depth and high secondary electron yield contribute to the quality and sharpness of the images obtainable with the HIM.

In its first decade of use, the HIM has been primarily limited to simple imaging, lacking a variety of add-ons available for SEM, in particular elemental analysis, where Energy-Dispersive X-ray (EDX) spectroscopy provides spatially resolved elemental composition of the sample surfaces. Unfortunately, a ~30 keV He beam is not capable of efficiently exciting core-shell electrons in the target. Thus there is a need for an alternative approach if nanoscale elemental information is desired.

In this chapter, I describe a Time of Flight (ToF) based technique for elemental analysis integrated into the Helium Ion Microscope. This approach uses a continuous ion beam at very low currents and measures the ToF of the backscattered He ions. Both electrons and He ions/atoms emitted from the sample during the scattering process are collected by two separate detectors. In the method we have developed, electrons serve as a starting signal, while the ions serve as a stop signal (described in much more detail below). From the difference between the stop and start timestamps, the time of flight, and thus the energy, of the scattered He ions can be determined. The energy of the He ions in turn identifies the masses, and thus the chemical elements that comprise the material from which the He is being scattered. The experiment is thus a nanoscale equivalent to Rutherford backscattering. Energy resolved backscattered Helium particles provide a quantitative method of elemental mapping with spatial (x and y) resolution of ~ 100 nm and with a depth resolution of ~ 3 nm with our current system. Better detection and better ion and electron optics should improve resolution.

3.2 Background

Elemental analysis with ion beams can be accomplished today by a variety of very well established techniques. However, very few of these techniques can provide spatial resolution, and none can approach the spatial resolution achievable with the HIM.

Micro-RBS and micro-PIXE (Rutherford Backscattering Spectrometry and Particle Induced X-Ray Emission) are two techniques that are often combined in a single instrument. An MeV particle beam is scanned across the sample producing backscattered ions and x-ray emission characteristic of the target material. Both techniques are very well established but require a dedicated particle accelerator and are limited to a few μm spatial resolution as described in chapter 2.

Secondary Ion Mass Spectrometry (SIMS) is another very well established method of elemental analysis with spatial and depth resolution. Heavy ions such as Ga, Cs and Ar are accelerated onto the sample at a few keV removing material. The ejected fragments are collected and their masses measured. SIMS provides a depth resolution of a few nanometers and a spatial resolution of about 60 nm. A group in Luxemburg has demonstrated the possibility of using Ne and He beams in a HIM system for SIMS analysis with significantly higher lateral resolution²⁷, however the milling speed and therefore efficiency of the process is not comparable with conventional heavy ion SIMS.

Transmission Electron Microscopy (TEM) – Electron energy-loss spectroscopy (EELS) is a technology that today provides the highest spatial resolution (in many cases sub-atomic) and the ability to identify elements by measuring the energy loss of transmitted electrons. The combination of imaging and elemental identification makes this method very attractive. However, the preparation of samples that are only a few tens of nm thick and the extended analysis time can sometimes be prohibitive.

Secondary Electron Microscopy (SEM) - Energy Dispersive X-Ray Spectroscopy (EDX) is a very common technique. It is a quick and easy analysis method that combines topological imaging of conducting samples and high-energy electron-induced X-ray analysis for elemental identification with a lateral resolution of $\sim 1 \mu\text{m}$. The disadvantages of the technique are modest lateral resolution and the limited scope of samples (only conducting materials).

3.3 Elemental Identification Efforts with the Helium Ion Microscope

As HIM technology matures, the need to answer more complex problems has become increasingly apparent. One such problem is the lack of quantitative elemental identification that takes advantage of the superb spatial resolution of the microscope.

As mentioned above, a group in Luxemburg has designed an HIM with an integrated SIMS apparatus that primarily uses sophisticated magnetic fields applied within the microscope and multiple detectors to resolve the masses of secondary ions ejected from the sample²⁸. Their approach is much less destructive than conventional SIMS due to use of light ions such as He and Ne vs. O₂, Cs, Ar or C₆₀. Lack of milling speed is compensated by very good spatial resolution in all 3 dimensions, approaching ~100s of nanometers laterally and a few nanometers in depth.

A group in Dresden has reported a slightly different approach. They use a Time-of-Flight principle where the time is determined by blanking the primary beam²⁹ for which they built an ultra-high speed beam-blanking device. Since they know when the beam is allowed to hit the sample, they are able to easily measure the time-of-flight of the backscattered He particles into a multi-channel-plate detector. The main limitation of this method lies in the speed of the blanker as it is difficult to rapidly ramp the voltage on the blanking plates. The best reported time resolution is 17 nanoseconds with 54 nm lateral resolution for a thick sample.

3.4 Rutgers Time of Flight System

Our group has, in collaboration with Ionwerks Inc, developed a Time-of-Flight detector system that operates continuously at low beam currents. The design is based on the principles of Rutherford Backscattering Spectroscopy (RBS). Usually, RBS operates at millions of electron volts on the primary beam (Figure 3.1).

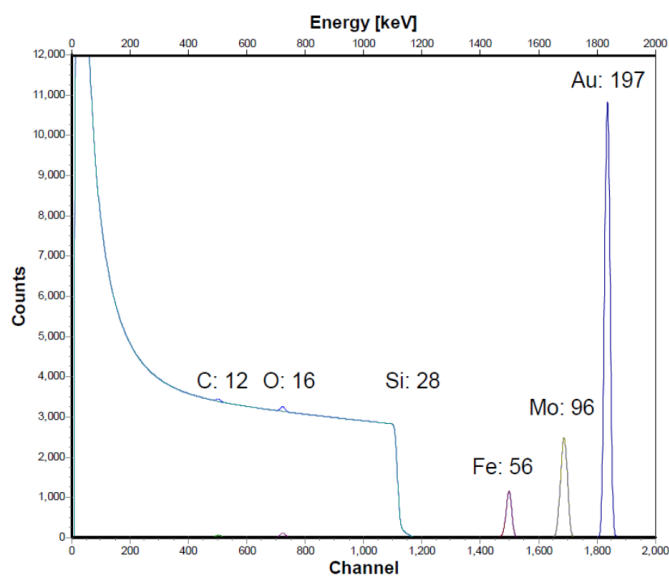


Figure 3.1 Sample RBS spectrum taken with a 2 MeV He beam.

2 MeV energy allows for large peak separation and an inexpensive depleted-silicon detector with a resolution of about 15 keV can be used (Figure 3.2)³⁰.



Figure 3.2 Commercial depleted Si detector from Ortec³⁰, commonly used for RBS and high-energy particle detection.

Unfortunately, HIM operates at a fraction of the conventional RBS energy and there is no available detector on the market capable of producing a useful spectrum in the 30 keV regime. In order to effectively separate peaks, the detector has to have a resolution of about 0.1 keV. Therefore, a new detector system had to be designed and constructed.

The system we designed consists of two detectors recording the time for the backscattered ion to travel a known distance from the sample to the detector. One detector collects secondary electrons (the start signal), while another records backscattered ions (the stop signal). The time it takes for a backscattered He particle (ion or neutral) to reach the ion detector is proportional to its energy and can be calculated by equation 3.1, where m is the mass of the probing particle, L is the distance from the sample to the ion detector and t is the time of flight.

$$E_d = \frac{1}{2} m \left(\frac{L}{t} \right)^2 \quad (3.1)$$

Then by calculating the difference in energy between the primary beam and the backscattered particle the elemental identity of the target atom can be determined as described above.

Figure 3.3 shows the secondary electron detector (SED) responsible for the collection of the secondary electrons. Once the sample is loaded into the HIM chamber, the SED is rotated into position about 0.5 mm above the sample surface. The design of the electrostatic elements allows it to efficiently bend and focus SEs onto the microchannel plate for detection and timestamping. Each electrostatic element has an assigned power supply, nine in total, which can be adjusted to optimize the electron trajectories to minimize the time spread in the start signal.

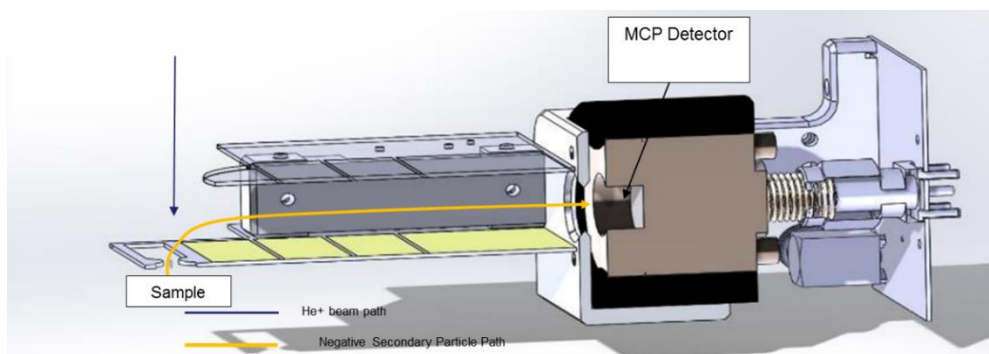


Figure 3.3 The Secondary Electron Detector mounted on the rotary stage.

The stop signal is generated by scattered He ions detected by a large (~ 4 cm diameter) position sensitive detector (PSD). The detector consists of a dual set of Microchannel Plates (MCPs) in a chevron orientation and located approximately 13 cm from the sample surface. This length corresponds to a flight time of ~ 110 ns for a 30 keV He ion. The solid angle from the sample to the detector is approximately 0.073 steradians. However, the detector operates at about 51% efficiency due to the fact that the regions between the channels (Figure 3.4) do not detect particles. This reduces the real solid angle to approximately 0.037 Steradians. The large area PSD minimizes the total incident beam requirement for a statistically significant analysis.

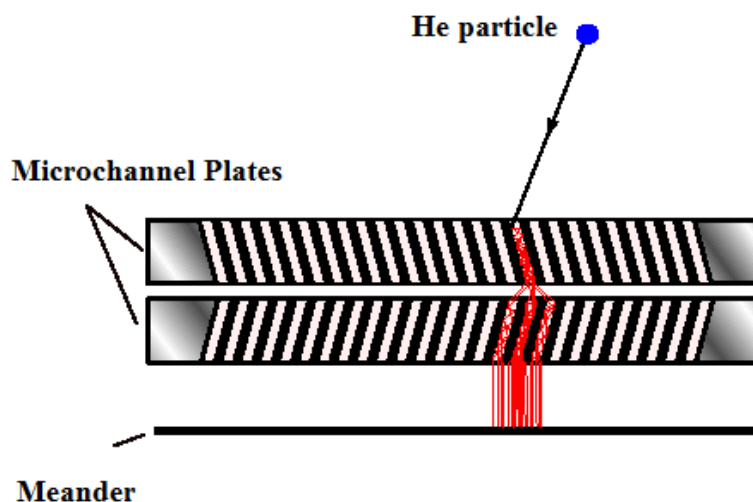


Figure 3.4 Standard microchannel plates in chevron orientation³¹. The signal is generated only when the particle can trigger an electron cascade in one of the channels. Otherwise, the signal is lost.

The microchannel plates in the PSD are coupled to a ~ 15 ns X and Y meander array visible in figure 3.5. The size of the detector imposes a time delay dependent on the hit position of the ion. The meander array gives us knowledge of the position of the incoming ion and therefore allows for corrections for slightly different flight and for kinematic corrections inherent in ion backscattering. Once the backscattered particle hits the PSD, it triggers the software to process and match accumulated signals from both the PSD and SED as described in figure 1.3.

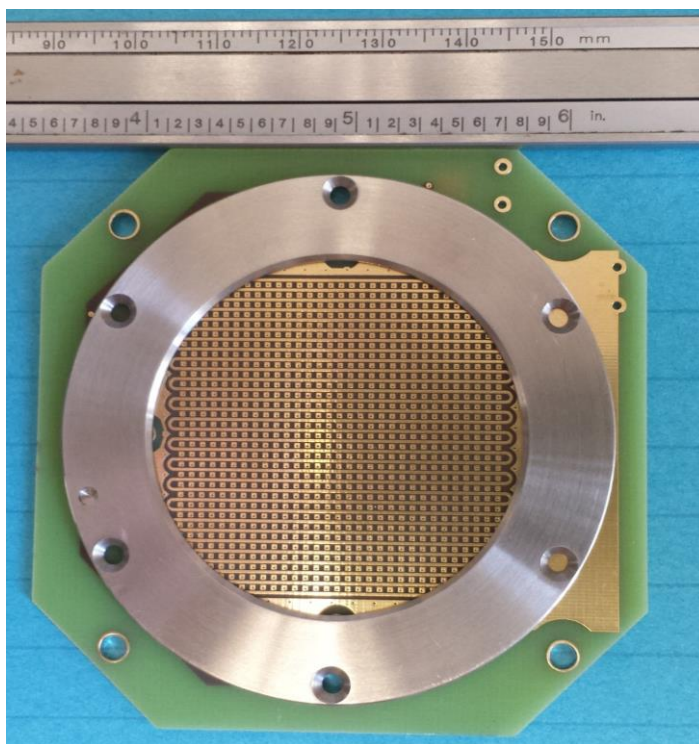


Figure 3.5 The Position Sensitive Detector (PSD). In this image the microchannel plates are removed, exposing the meander array that provides position sensitivity.

The software is written in C# and designed to operate within a virtual time window of about $1 \mu\text{s}$ (at a 1pA ion current we expect to only have six ions impinging onto the sample per $1 \mu\text{s}$). At such low currents, we expect to have one or two electron events on the SED and a single triggering ion event coming from the PSD. In case no ion event is recorded, the electron data are discarded. If an ion event is recorded, the software calculates the difference in the timestamps

between the electron and the ion event and builds up a chart of this. Additionally, every ion event is recorded with its position information with respect to the detector area. Since the detector is a flat microchannel plate, ion trajectories originating from the sample onto the center of PSD vs. its edge will have different flight times (for 28 keV He this difference is ~ 2 ns). Furthermore, an additional variation of backscattering energies will arise from their angular distribution based on equation 2.9, commonly referred to as the kinematic spread. The position sensitivity in our detector allows us to account for such geometrical factors in calculating the ToF for each ion while maintaining a large solid angle.

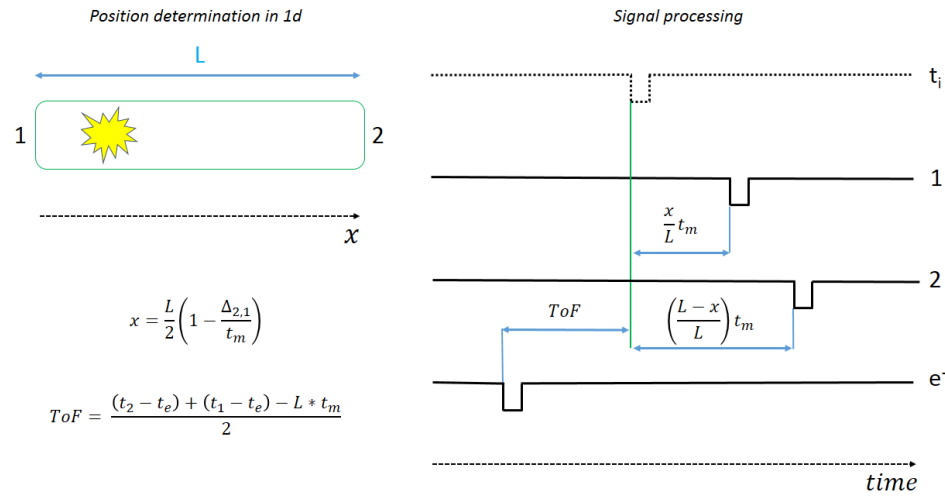


FIGURE 3.6 Position determination of an ion hit in a 1D case. t_i is the virtual signal denoting the real Time of Flight, channels 1 and 2 are the two opposite outputs of the meander wire. e^- is the electron start signal. t_m is the “meander time” associated with a position dependent time delay on the actual ion arrival time. $\Delta_{2,1}$ is the difference in time between signals on channels 2 and 1.

The electron start signal and the four ion signals (two to define X and two to define Y) are coupled to an HPTDC8-PCI time to digital converter (TDC, 25 ps resolution board made by Cronologic GmbH & Co. KG) for energy/time analysis and position definition. A one-dimensional schematic of the time sequence array is shown in figure 3.6. Time delays with respect to the electron determine the ToF and time differences between the ion signals on the meander

determine the position of the ion hit on the channel plate. The overall design time resolution is 0.4 ns. Early results (Figure 1.6), uncorrected for finite detector effects, show 2 ns time resolution.

3.5 Results

Damage and sputtering of the sample limit the sensitivity. Generally, the detected flux of backscattered particles can be calculated using equation 3.2,

$$Y = \sigma(\theta) \times \Omega \times Q \times \Delta N \quad (3.2)$$

where $\delta(\theta)$ is the scattering cross section, Ω the solid angle of the detector, Q the number of incident particles and $N\Delta t$ the number of target atoms. In order to obtain a detection limit in the ToF measurement, one can use equation 3.2 to calculate the flux that is needed to obtain the desired number of counts in the detector – Y . If we arbitrarily set 150 counts in the detector as a statistically significant signal this will require 3.6×10^7 He ions impinging on the sample in our geometry. The next step is to account for sputtering effects. 3.6×10^7 He atoms will sputter about 1×10^6 atoms of Pt from the sample. Now we can determine the smallest area that will contain the required number of Pt atoms. The Pt density is 6.6×10^{22} atoms/cm³ and assuming a 1 nm thick layer of Pt, the smallest area is about 150 nm by 150 nm. The largest uncertainty in this calculation is the sputtering yield of the thin 1 nm layer vs. a bulk metal substrate. We have measured (see below) the decay of the signal as a function of dose for a 1 nm Pt film, which indicate a factor of four difference (0.044 vs 0.01)³² compared to the literature value for a semi-infinite film (Figure 3.10). As discussed below this is still more than one order of magnitude more sensitive than can be expected in an EDX measurement, and it is possible to do significantly better.

The first demonstration of the Rutgers ToF system was performed on a structure composed of a 0.7 nm thick layer of gold on top of a 3.3 nm layer of nickel on a silicon substrate

(Figure 1.6). The thin peak at 110 ns corresponds to the gold layer and the slightly thicker signal at 140 ns to Ni. This spectrum was accumulated on an area of about 200 by 200 μm and took ~ 1 minute to collect. We minimized the kinematic spread by selecting a small region of the detector.

We next demonstrate that the ToF spectra can yield information about elemental composition of the substrate as a function of depth from the surface. We show here results for a dielectric stack consisting of 5 ultrathin layers of HfO_2 interlaid with SiO_2 (Figure 3.7). We can clearly see 5 peaks corresponding to the Hf in the HfO_2 layers. The decreasing plateau that starts around 200 ns is from the silicon substrate. However, at the current noise levels, it is impossible to distinguish any silicon peaks. Based on experiences from conventional RBS data, the substrate yield should be increasing in intensity as we shift to lower energies. Yet when looking at the time spectrum one sees the opposite effect. This is explained by classical mechanics, equation 3.3, where a decrease in the speed of the particle is proportional to the square root of the decrease in its energy. In other words, each reduction of energy will cause a larger decrease in speed and thus a longer time of flight. This phenomenon can also explain the asymmetry that can be observed, especially on the Ni peak (figure 1.6).

$$E = \frac{1}{2}mv^2 \quad (3.3)$$

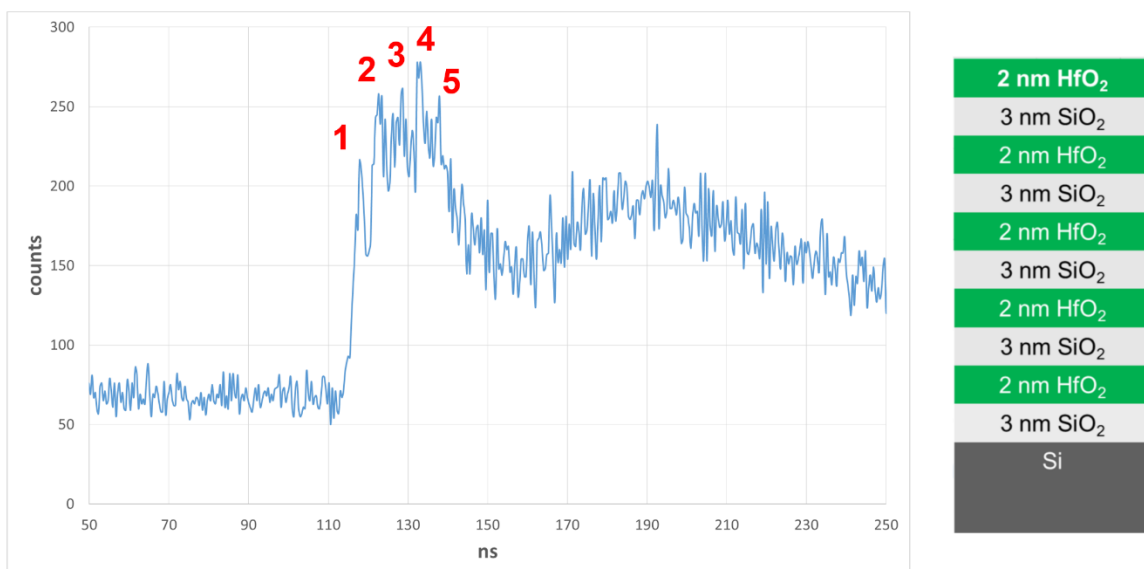


Figure 3.7 ToF spectrum for a hafnium oxide/silicon oxide multi-layer stack. Similar conditions as in figure 1.6

As a He ion has a larger mass than an electron, it will induce atomic displacements which can be described as sputtering, resist free lithography or ion beam damage. In order to understand the limitations of the system, we performed an analysis of a 1 nm platinum layer, deposited on a silicon dioxide surface using e-beam evaporation as a function of dose (Figure 3.8). The thickness of the sample was confirmed with angle-resolved XPS and RBS. The He ion beam was scanned over the same area multiple times, delivering a controlled dose on each scan. Time of Flight spectra were acquired simultaneously and the decrease in intensity of the platinum peak with increasing ion dose was measured. In these experiments the dose required to completely eliminate the signal is above 5×10^{17} ions/cm² which allows us to determine the damage-related sensitivity of this method (under these conditions). One important caveat is our incomplete understanding of the ion beam spot and its size. The Pt sample was analyzed with an area of 500 by 500 nanometers divided into a 500 by 500 pixel grid, which means that each pixel is ~ 1 nm² (Figure 3.9). However, Zeiss claims that the beam spot size is about 3 Ångströms, which, if true, would imply a significant reduction in the actual irradiated area. This problem was solved by

slightly defocusing the beam. Unfortunately there is then no reliable way of measuring the beam spot size and it thus represents an ambiguity in our calculation.

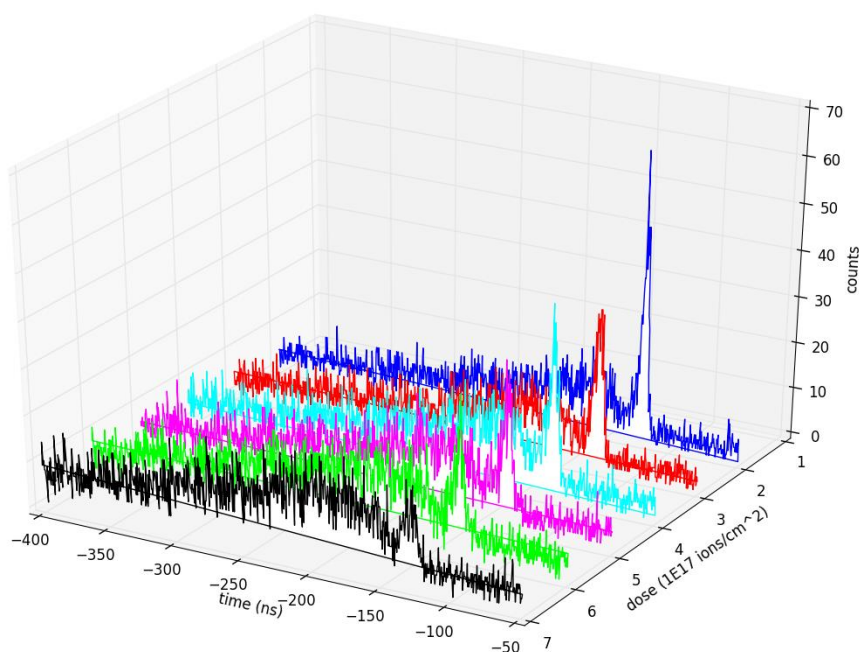


Figure 3.8 Dose dependence study of 1 nm Pt on Si. The Pt signal decay and broadening are observed as the ion dose is increased, indicating layer intermixing and Pt sputtering.

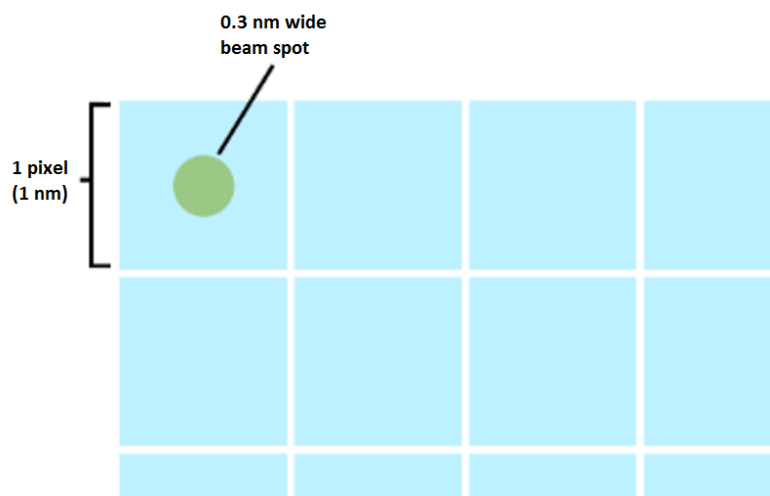


Figure 3.9 Beam spot size vs area scanned. 500 nm field of view at 1 nm per step.

3.6 Current Performance of the Rutgers elemental identification scheme

Beam induced sample deterioration

The detection limit was determined based on the Pt sputtering experiment described above (Figure 3.8). By measuring the decrease of the Pt signal as a function of ion dose, an effective sputtering coefficient for 30 keV He ions was derived. The resulting value is 0.01 (the literature values for a bulk Pt sample is 0.04)³². Our measured sputtering coefficient therefore did show a difference from the bulk Pt value³² by a factor of four. In figure 3.10, the Pt peak demonstrates a deviation from a steady decrease at higher doses. We hypothesize that the increase of the Pt peak area for longer times is primarily due to ion beam mixing and uncertainty in the ion beam position. In the case of ion beam mixing, we can reasonably expect that the Helium ions may be burying some of the Platinum into the substrate, slowly increasing the sputtering of Si and decreasing sputtering of Pt. Changes in the relative importance of forward knock-on and sputtering yield as a function of time could yield to changes in surface Si to Pt ratio (as we have repeatedly observed).

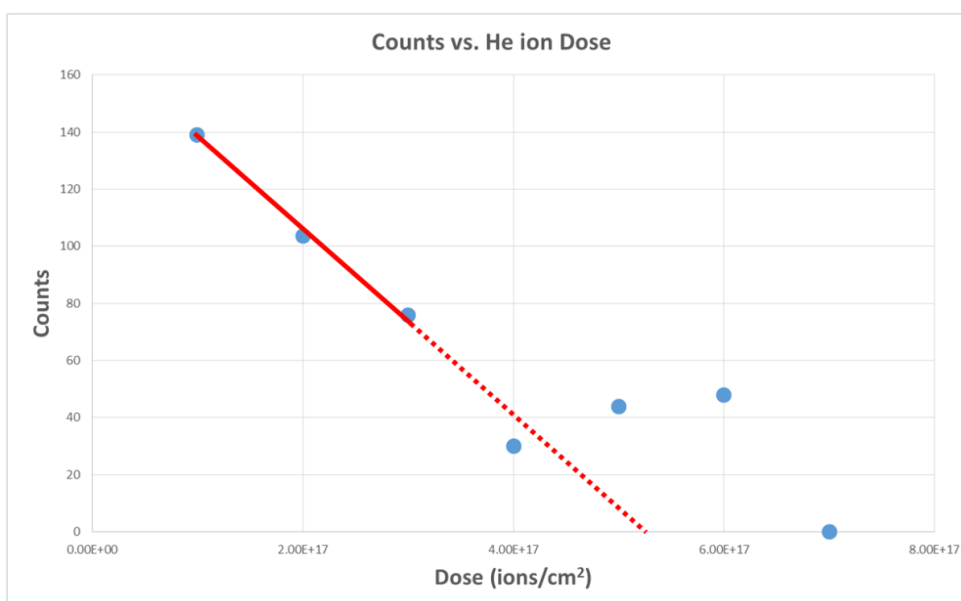


Figure 3.10 Analysis of the Pt peak as a function of He dose. The red solid line indicates the best fit for the first 3 points and the dotted line is the extrapolation.

As for uncertainties associated with the ion beam position, we do not know the reproducibility of the precise location of the ion beam within the pixel (Figure 3.9). As discussed above, our beam spot is smaller than the size of a pixel for our best resolution images, so any small fluctuations in the instrument such as nm size mechanical vibration can cause a slight beam spot shift and expose new areas on the sample. For these reasons, we only use our first three data points in figure 3.10 to give the best indication of the effective sputtering coefficient.

Additional deviations from the expected straight line in the data that appear with increased dose seem to have similar slopes to that of the first three data points. This supports our hypothesis that either platinum initially becomes buried in the substrate and later emerges again as Si is sputtered away, or different areas on the sample are exposed—if not both.

Time and energy resolution

To determine the time and therefore energy resolution, the width of the Au peak for the 0.7 nm Au sample (Figure 1.6) was analyzed. The kinematic spread is minimized by selecting a sub-region of the detector: a tenth of the size of the whole (4 cm in diameter) PSD. The best measured time resolution for our system is then 2 ns or 1.1 keV. Our target resolution of 200 ps (0.11 keV) can be achieved by increasing the flight time.

Sensitivity

In order to compare our elemental sensitivity by other techniques, SEM being the most relevant, we prepared thin (0.7 nm) gold and (1 nm) platinum samples by evaporation. They were then analyzed using a 20 keV electron beam in a Zeiss Gemini SEM using an Oxford x-ray detector. For both samples (Figure 3.11) EDX was not able to identify any thin metal signals because electrons have a very low cross section to ionize core shell electrons in the material, so few X-rays

are emitted. Additionally, EDX requires a very large electron flux (currents in the microampere range), while helium analysis is done with beam currents six orders of magnitude lower. However, even neglecting the difference in analysis currents for each technique and keeping the same analysis time (between 30 seconds and 3 minutes), He ion beam ToF analysis demonstrates much higher sensitivity to the surface layers of a sample. When coupled to the quantitative nature of the backscattering analysis, HIM ToF demonstrates a higher surface sensitivity for thin layers or small concentrations of elements on or in materials, at least compared to this SEM.

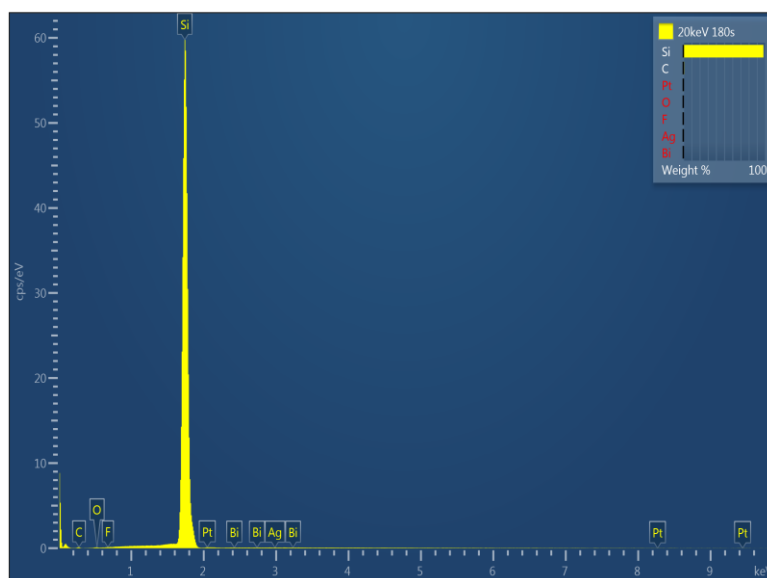


Figure 3.11 EDX analysis of the 1 nm Pt sample described above. Total area analyzed is 1 μm^2 with 20 keV electrons on a Zeiss Gemini SEM. Analysis of 1 nm Au samples showed very similar results. The expected position of a possible Pt signal is given at the right.

3.7 Future Work

The next generation HIM – ToF system should provide significantly better performance if rather straightforward improvements are incorporated into the system. A larger PSD will make collection much more efficient. Smaller collection times will reduce the dose needed (and therefore damage due to sputtering, ion mixing and sample swelling).

Additionally, re-designing the secondary electron detector will result in faster and more efficient electron collection. The current design does not result in all electron trajectories arriving

at the same time, which translates into a broadening of the signal. As we target 200 ps resolution for our entire system, more efficient electron collection must be addressed.

If smaller data collection times are needed, higher beam currents should be used. One then needs to increase the upper threshold for the number of electrons counted per second.

Furthermore, a longer path for backscattered ions will dramatically enhance peak separation—especially for heavier elements. As shown in equation 2.9, the kinematic factor implies a larger separation in backscattering energy for lighter elements. Correspondingly, the peak separation is worse for heavier elements. An elongated flight path will alleviate this and even let us to be able to separate ^{12}C and ^{13}C isotopes. Placing the PSD at a greater distance (r) from the sample will reduce the solid angle by a factor of r^2 . Therefore a larger area detector is needed to avoid a loss in efficiency. Additionally, a lower beam energy may be beneficial for peak separation as the time of flight increases at lower energies of the backscattered particles. Also, ultra high vacuum conditions may help by eliminating unwanted collisions of backscattered particles and reducing the energy spread of the signal.

3.8 Conclusions

We have constructed and demonstrated the performance of a high-resolution elemental identification spectrometer using a 30 keV He nano-beam time-of-flight system. In combination with advanced imaging capabilities, this allows us to determine the elemental composition of the samples with significantly higher sensitivity than offered by EDX in an SEM system. Further developments of the technique are straightforward and already underway which will bring enhanced sensitivity, improved detector design and more efficient element-specific scanning capability.

Chapter 4

Mitochondria Protection after Acute Ischemia Prevents Prolonged Upregulation of IL-1b and IL-18 and Arrests CKD

This chapter is based on a paper published in Journal of American Society of Nephrology⁸. My contributions to the paper include providing Helium Ion Microscopy imaging and characterization and optimization of the sample preparation protocols for the HIM. This chapter is a demonstration of highly specialized application of HIM technology to biological samples as outlined in earlier chapters.

4.1 Introduction

Patients who survive acute kidney injury (AKI) have a greater risk for chronic kidney disease (CKD)³³. Currently, treatment of CKD is limited to aggressive control of hypertension with inhibitors of the renin-angiotensin-aldosterone system and reducing nitrogen load to the kidney. Although there are a number of experimental interventions in clinical trials, they have to be administered before or shortly after the acute injury³⁴, and some are offset by serious adverse effects³⁵⁻³⁹. The Acute Dialysis Quality Initiative XIII Work Group recently concluded there are no therapeutic interventions specifically targeting progression from AKI to CKD⁴⁰.

Treatment Groups	Treatment Begins 1 mo after Ischemia	Study Terminates after 1.5 mo Drug Treatment	Study Terminates 6 mo after Treatment Termination
Saline	19	13	6
SS-31, 2 mg/kg per d	18	12	6

Table 4.1 Experimental study groups. All data presented as n. A total of 50 rats were included in this study. Rats that survived the acute ischemic challenge (n=37) were randomized to receive either saline or SS-31 for 1.5 months.

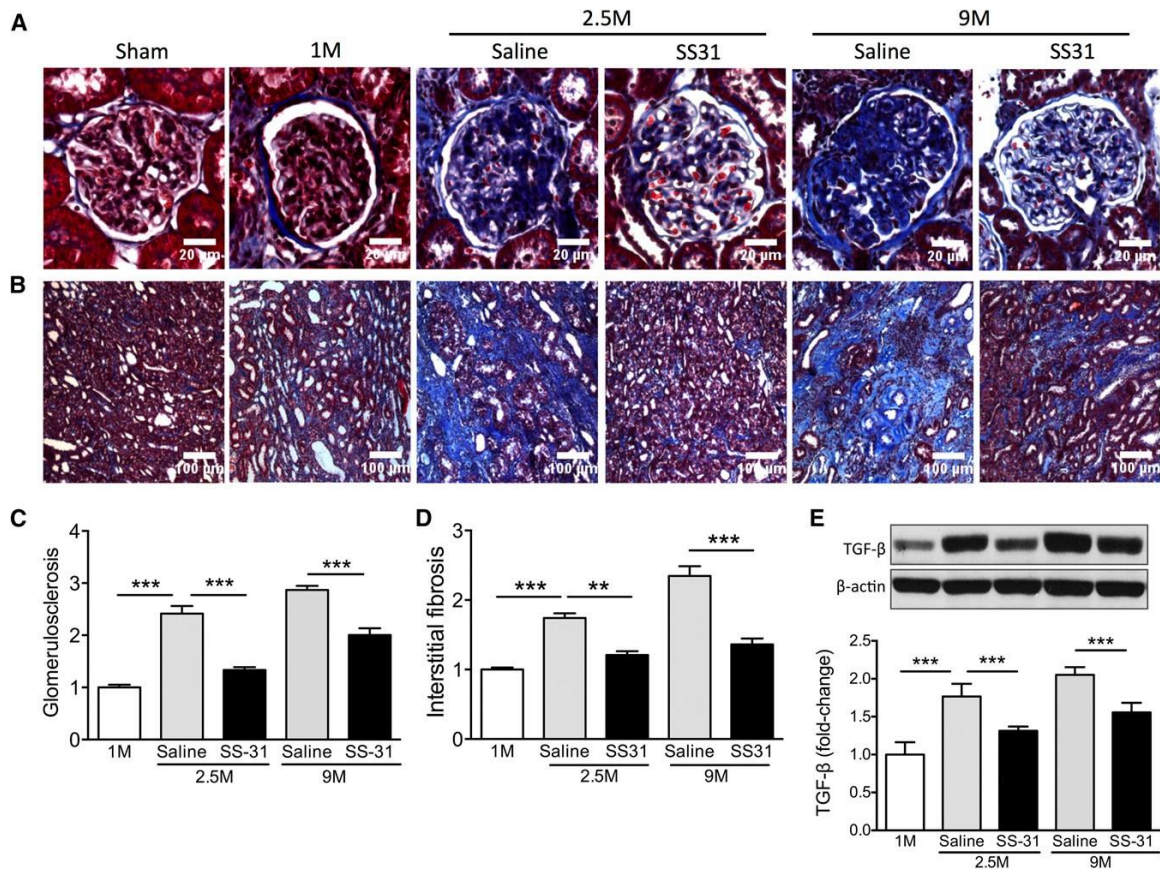


Figure 4.1 SS-31 halts progression of interstitial fibrosis and glomerulosclerosis after acute renal ischemia. Rats were treated with SS-31 (2 mg/kg per day) or saline for 1.5 months starting 1 month after acute ischemia. (A) Representative images of trichrome stain of the renal cortex showing progressive increase in glomerulosclerosis at 1 month (1M), 2.5 months (2.5M), and 9 months (9M) after acute ischemia. Treatment with SS-31 starting at 1M prevented progression of fibrosis at 2.5M, and protection was seen even 6 months after termination of treatment. (B) Representative images of trichrome stain of the inner stripe of the outer medulla (ISOM) showing prevention of fibrosis by SS-31 treatment. (C) Quantification of trichrome stain in glomeruli at various times after ischemia. Data shown as mean \pm SEM; n=4/ group; ***P,0.001. (D) Quantification of trichrome stain in ISOM at various times after ischemia. Data shown as mean \pm SEM; n=4/ group; **P,0.01; ***P,0.001. (E) Representative Western blot and densitometric analysis of TGF- β expression in renal cortical tissue. Data shown as mean \pm SEM; n=4/group; ***P,0.001.

Given the increasing global burden of CKD⁴¹, novel strategies that can halt the progression of CKD and restore normal renal structure and function are needed⁴⁰. Inflammation plays a critical role in the initiation and progression of renal fibrosis⁴⁰. Injured epithelial cells secrete proinflammatory cytokines to recruit inflammatory cells to sites of injury to drive tissue repair. Profibrotic cytokines, such as TGF- β , stimulate matrix-producing cells to produce extracellular matrix. Anti-fibrotic treatments have mostly targeted TGF- β , but TGF- β is a pleiotropic cytokine with vital anti-

inflammatory functions, and blocking TGF- β activity may incite immune activation⁴². It is thus imperative that novel targets be identified that can arrest the chronic inflammation and progressive fibrosis.

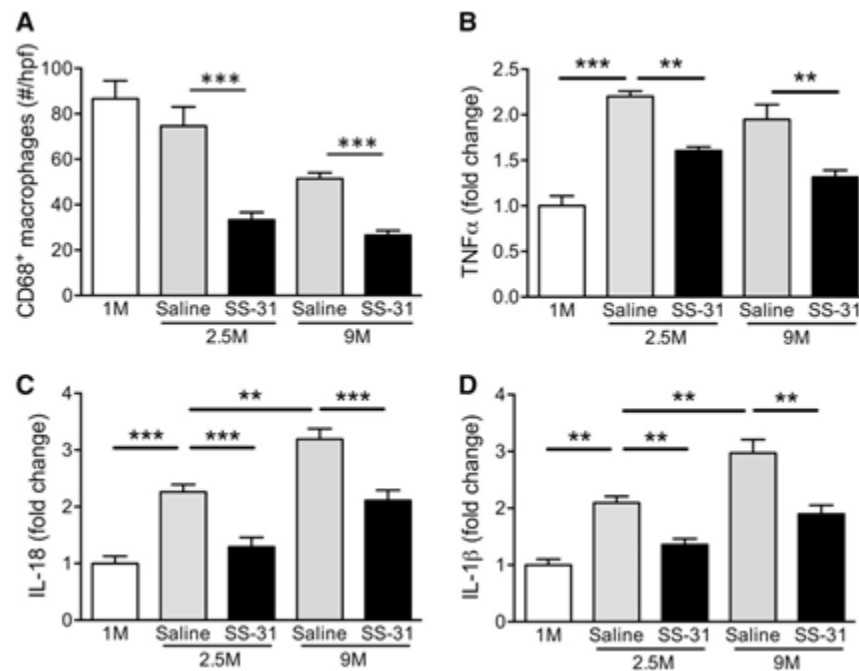


Figure 4.2 SS-31 reduces inflammation after acute renal ischemia. Rats were treated with SS-31 (2 mg/kg per day) or saline for 1.5 months starting 1 month after acute ischemia. (A) The number of CD68⁺ macrophages per glomerulus at various times after ischemia. The number shown reflects the average determined from ten glomeruli per sample and averaged. Data shown as mean \pm SEM; n=4/group; ***P,0.001. (B) Representative Western blot and densitometric analysis of TNF- α expression in renal cortical tissue at various times after acute ischemia. Data shown as mean \pm SEM; n=4/group; **P,0.01; ***P,0.001. (C) Representative Western blot and densitometric analysis of IL-18 expression in renal cortical tissue at various times after acute ischemia. Data shown as mean \pm SEM; n=4/group; **P,0.01; ***P,0.001. (D) Representative Western blot and densitometric analysis of IL-1 β expression in renal cortical tissue at various times after acute ischemia in saline and SS-31-treated rats, versus age-matched controls. Data shown as mean \pm SEM; n=4/group; **P,0.01.

The innate immune system has recently been implicated in both acute and chronic kidney injury⁴³⁻⁴⁴. Necrotic cells release danger-associated molecular patterns (DAMPs) that can trigger an inflammatory form of cell death mediated by Nod-like receptors (NLRs)⁴⁵. These NLRs form multimeric protein complexes termed inflammasomes, of which NLRP3 is the best understood for its involvement in chronic and acute kidney disease⁴⁶⁻⁴⁷. The NLRP3 inflammasome triggers

activation of caspase-1, which then processes the proinflammatory cytokines pro-IL-1b and pro-IL-18 into their bioactive mature forms. The inflammasome may be considered the final common pathway that sustains the inflammation–fibrosis cycle in CKD, and IL-1b and IL-18 represent potential therapeutic targets for CKD⁴⁸.

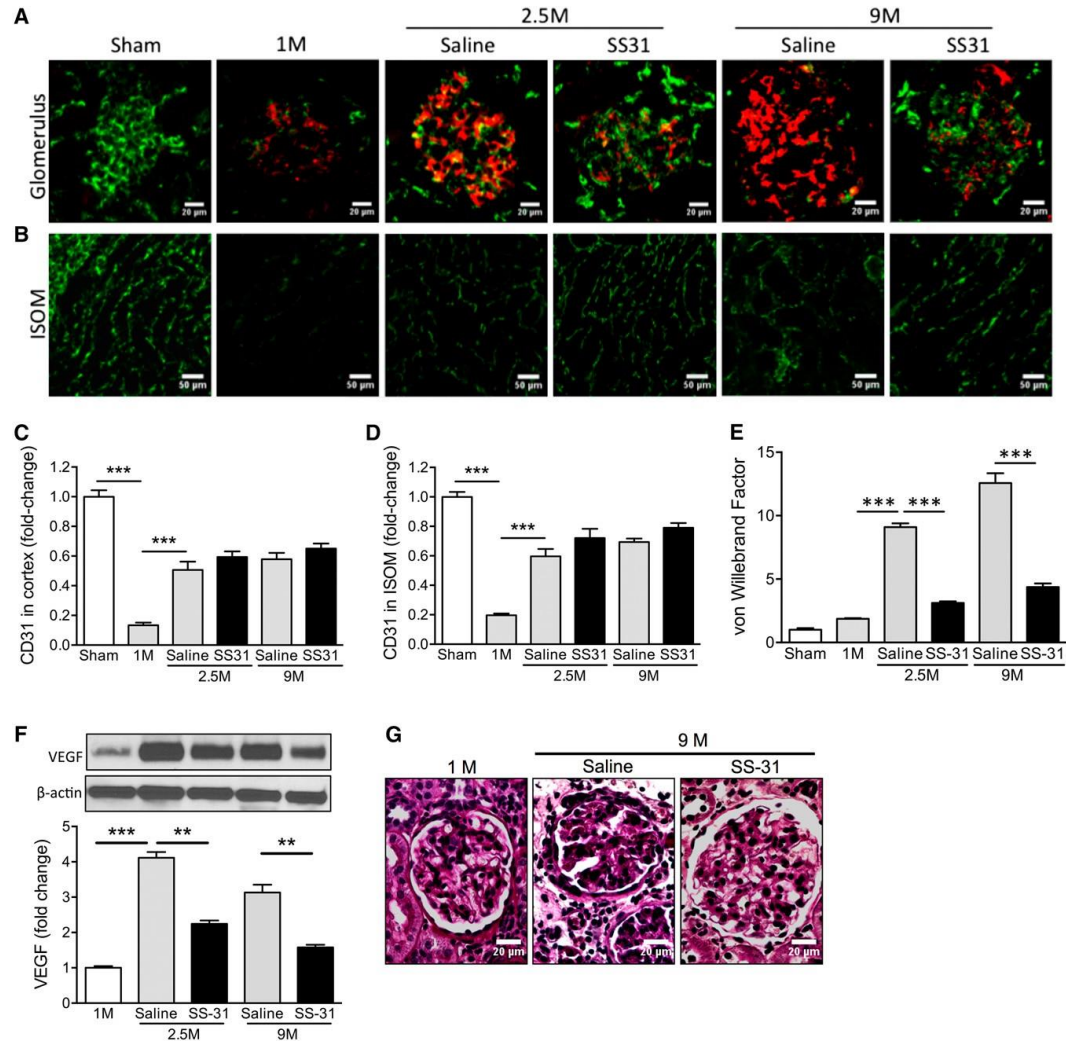


Figure 4.3 SS-31 reduces endothelial injury after acute ischemia. Rats were treated with SS-31 (2 mg/kg per day) or saline for 1.5 months starting 1 month after acute ischemia. (A) Representative microscopic images of glomeruli showing endothelial cell marker CD31 (green) and vWF (red) in saline- and SS-31-treated rats at 1 month (1M), 2.5 months (2.5M), and 9 months (9M) after ischemia. (B) Representative microscopic images of inner stripe of outer medulla (ISOM) showing CD31 (green) in saline and SS-31-treated rats at 1M, 2.5M, and 9M after ischemia. (C) Densitometric analysis of CD31 staining in renal cortex showing significant decrease in endothelial cell marker 1M after ischemia and partial recovery by 2.5M. SS-31 treatment had no effect on CD31 recovery. Data shown as mean±SEM; n=4/group; *** p < 0.001, ** p < 0.01.

Inflammasome activation in response to a variety of stimuli appears to converge upon mitochondrial reactive oxygen species (ROS)⁴⁹⁻⁵¹. Mitochondrial DNA and N-formyl peptides represent two other sources of mitochondrial DAMPs⁵².

Compounds that cause mitochondrial damage enhance NLRP3 activation, whereas compounds that reduce mitochondrial ROS inhibit inflammasome activation⁵³⁻⁵⁵. Further, NLRP3 appears to bind directly to cardiolipin, a phospholipid that is only expressed on the inner mitochondrial membrane, suggesting that mitochondrial damage and the translocation of cardiolipin to the outer mitochondrial membrane (OMM) may provide the docking signal for inflammasome assembly and activation⁵⁶. Ischemia causes mitochondrial injury⁵⁷, but it is not known if mitochondrial damage persists long after ischemia to account for sustained inflammasome activation.

SS-31 (also known as elamipretide) is a synthetic tetrapeptide (D-Arg-2969-dimethyl Tyr-Lys-Phe-NH₂) that selectively targets cardiolipin on the inner mitochondrial membrane to protect cristae curvature, stabilizes mitochondrial structure, facilitates electron transport, and minimizes ROS production⁵⁸⁻⁶⁰. SS-31 is very effective in minimizing ischemic AKI and preventing the development of interstitial fibrosis and glomerulosclerosis^{57, 61}.

It is not known if later administration of SS-31 can stop the progression of CKD. We conducted a 9-month study in rats subjected to bilateral renal ischemia. Significant mitochondrial damage was found in endothelial cells, podocytes, and proximal tubular cells 9 months after ischemia. Treatment with SS-31, starting 1 month after ischemia and maintained for 6 weeks, protected mitochondrial integrity and halted the progression of glomerulosclerosis and tubulointerstitial fibrosis. The protection by SS-31 was sustained for at least 6 months after treatment ended. Upregulation of IL-1b and IL-18 at 9 months after ischemia was normalized by

SS-31 treatment, suggesting that SS-31 reduced CKD by protecting mitochondria and preventing inflammasome activation.

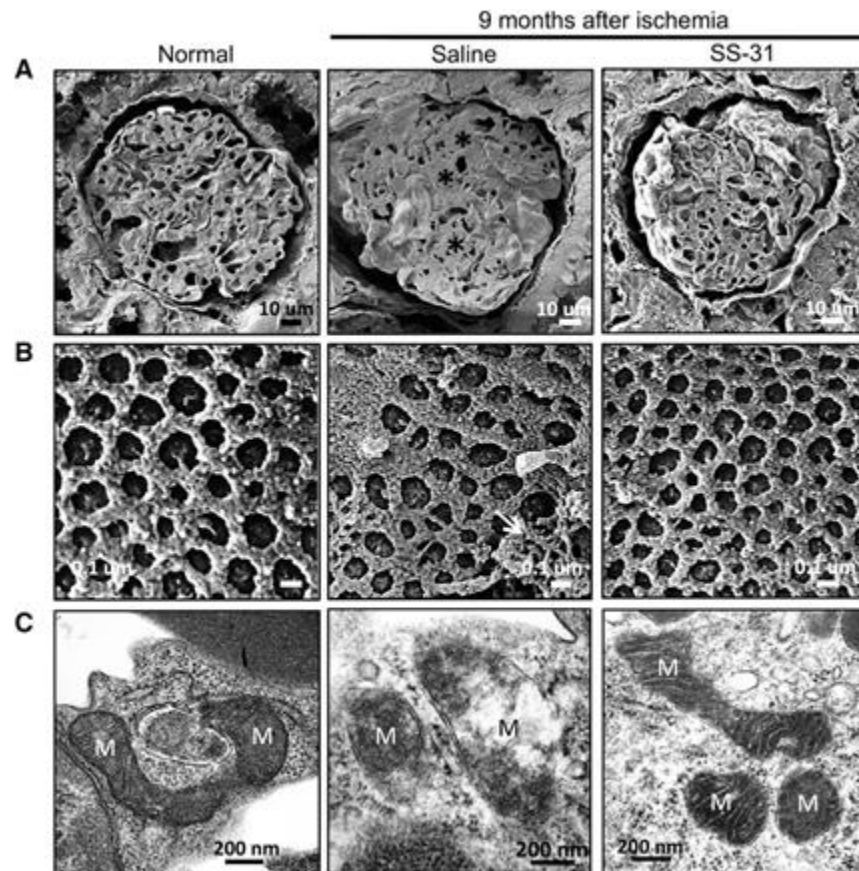


Figure 4.4 SS-31 reduces glomerular capillary compression and damage to endothelial fenestrations after acute ischemia. Rats were treated with SS-31 (2 mg/kg per day) or saline for 1.5 months starting 1 month after acute ischemia. Glomerular capillary structure was examined by HIM. (A) Representative cross-sectional images of glomeruli at 9M after acute ischemia from saline and SS-31-treated rats, compared with age-matched normal rats. Ischemia caused capillary compression because of mesangial expansion in saline-treated rats. Capillary loops are much more apparent in SS-31-treated rats and similar to image from normal rat. (B) Representative HIM images showing endothelial fenestrations from saline versus SS-31 rats compared with age-matched normal rats. Fenestrations are uniform in normal rats, whereas saline-treated rats show distorted fenestrations and adhesive material (white arrow). SS-31 treatment restored normal fenestration pattern. (C) Representative electron micrograph showing glomerular endothelial cell mitochondria from saline versus SS-31 rats at 2.5M after ischemia, compared with normal rat. Saline-treated ischemic cells show degenerative changes in mitochondria with disruption of cristae architecture, reduced matrix density, and some loss of OMM. SS-31 treatment restored normal endothelial mitochondria. M, mitochondria.

4.2 Results

SS-31 Reverses Tubulointerstitial Fibrosis and Glomerulosclerosis after Acute Ischemia

Adult rats (n=53) were subjected to bilateral renal ischemia for 45 minutes and then allowed to recover for 4 weeks. Mortality was approximately 30% with 45 minutes ischemia, but normal renal function was fully restored after 4 weeks⁶¹. Surviving animals (n=37) were randomly assigned to treatment with saline or SS-31 (2 mg/kg per day) for 1.5 months via a subcutaneously implanted osmotic pump (see Table 1).

Previously reported that this duration of ischemia results in tubular necrosis and significant increase in serum creatinine, blood urea nitrogen (BUN), and fractional excretion of Na⁺ and K⁺.²⁵ Although full recovery of renal function is achieved < 1 week after ischemia, interstitial fibrosis is seen in the outer medulla 1 month later⁶¹. In this study, we found progressive increase in interstitial fibrosis and glomerulosclerosis through 9 months after ischemia (Figure 1, A–D) that were associated with continuing increase in TGF-*b* expression in renal cortical tissue (Figure 4.1E). Six weeks of treatment with SS-31, starting 1 month after ischemia, significantly blunted the upregulation of TGF-*b* (Figure 4.1E) and halted the progression of interstitial fibrosis and glomerulosclerosis (Figure 4.1, A–D). This antifibrotic effect of SS-31 was sustained for > 6 months after treatment (Figure 4.1, A–D).

SS-31 Treatment Limits Inflammatory Response after Ischemia

My colleagues have previously reported > 15-fold increase in TNF-*a* and interstitial infiltration of lymphocytes and macrophages 1 month after acute ischemic injury⁶¹. Here we report further increase in TNF-*a* expression in renal cortical tissue and glomerular infiltration of CD68⁺ macrophages 2.5 months after acute ischemia (Figure 4.2, A and B). This inflammatory response remained high but began to decline by 9 months. SS-31 significantly reduced TNF-*a*

expression and macrophage infiltration at 2.5 months, and this effect was sustained for > 6 months after termination of treatment.

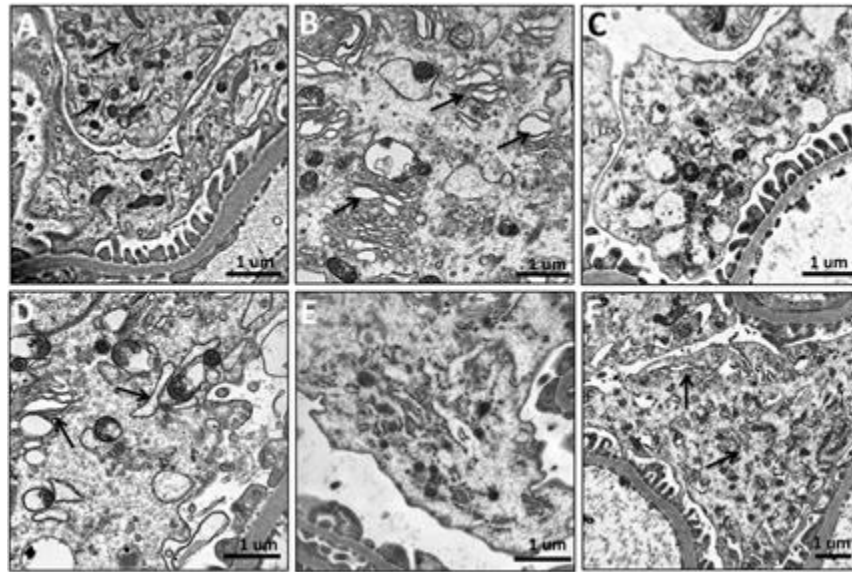


Figure 4.5 SS-31 prevents podocyte stress after acute ischemia. Rats were treated with SS-31 (2 mg/kg per day) or saline for 1.5 months starting 1 month after acute ischemia. Podocyte structure was examined by transmission electron microscopy. (A) Representative image of a normal podocyte showing dense cytoplasm containing large number of endoplasmic reticulum (ER; arrows) and mitochondria. (B) Representative image obtained 1 month after ischemia showing pronounced dilation of ER (arrows). (C) Representative image obtained 2.5 months after ischemia showing loss of cytoplasmic density and large number of vacuoles. (D) Representative image obtained 9 months after ischemia with numerous dilated ER (arrows). (E) Representative image obtained 2.5 months after ischemia following short-term SS-31 treatment showing normal cytoplasmic structures. (F) Representative image obtained from an SS-31-treated rat 9 months after ischemia showing persistent podocyte protection with normal ER (arrows).

The eventual decline in $\text{TNF-}\alpha$ and macrophage infiltration led us to question if inflammasome activation plays a role in sustaining the continual upregulation of $\text{TGF-}\beta$. The expression of IL-18 and $\text{IL-1}\beta$ continued to increase at 9 months after ischemia, but they were abolished by 6 weeks of SS-31 treatment (Figure 4.2, C and D).

SS-31 Reverses Endothelial Injury after Ischemia

Renal ischemia causes peritubular micro-vascular rarefaction that contributes to further tissue damage⁶¹⁻⁶³. There was significant loss of CD31 immunostaining in the renal cortex 1 month

after ischemia, primarily in the glomeruli (Figure 4.3, A and C). There was also significant loss of CD31 in the inner stripe of the outer medulla (Figure 4.3, B and D). Despite partial recovery of CD31 expression in the renal cortex by 2.5 months, there was persistent upregulation of vascular endothelial growth factor even 9 months after ischemia (Figure 4.3E), suggesting prolonged tissue hypoxia. The dramatic upregulation of vWF expression in post-ischemic glomeruli (Figure 4.3, A and F) indicates persistent endothelial injury after acute ischemia. vWF is a glycoprotein that mediates platelet adhesion to the subendothelium at sites of vascular injury, and it is normally not expressed in human glomeruli⁶⁴. No vWF expression in normal rat glomeruli was found, but vWF was clearly present in glomeruli at 1 month and progressively increased over 9 months after ischemia (Figure 4.3, A and F). Treatment with SS-31 did not improve CD31 expression (Figure 4.3, C and D), but significantly reduced vWF and vascular endothelial growth factor expression at 2.5 and 9 months, and the effect persisted for 6 months after treatment (Figure 4.3, E and F). Mesangial deposition of vWF is associated with mesangial matrix expansion and fibrin deposition⁶⁵, and periodic acid–Schiff staining showed that SS-31 prevented mesangial expansion at 9 months (Figure 4.3G).

SS-31 Protects Glomerular Capillary Loops and Fenestrations after Ischemia by Protecting Endothelial Mitochondria

We used helium ion microscopy (HIM) to further investigate damage to glomerular capillaries and endothelial fenestrations after acute ischemia. HIM provides subnanometer resolution images of biologic tissues with greater detail than scanning electron microscopy⁶⁶⁻⁶⁷. Figure 4.4A shows a representative cross-section of an age-matched (11 months) normal rat glomerulus with numerous capillary loops. In contrast, mesangial expansion and compressed capillary loops were observed 9 months after ischemia. SS-31 restored majority of capillary loops

and reduced mesangial volume. Closer examination of the capillary endothelial surface shows uniform fenestrations in a normal glomerulus (Figure 4.4B). In contrast, there was loss of fenestrations and extensive adhesive material on the endothelial surface 9 months after ischemia. SS-31 restored normal fenestrations and reduced adhesive material, consistent with reduction of vWF expression.

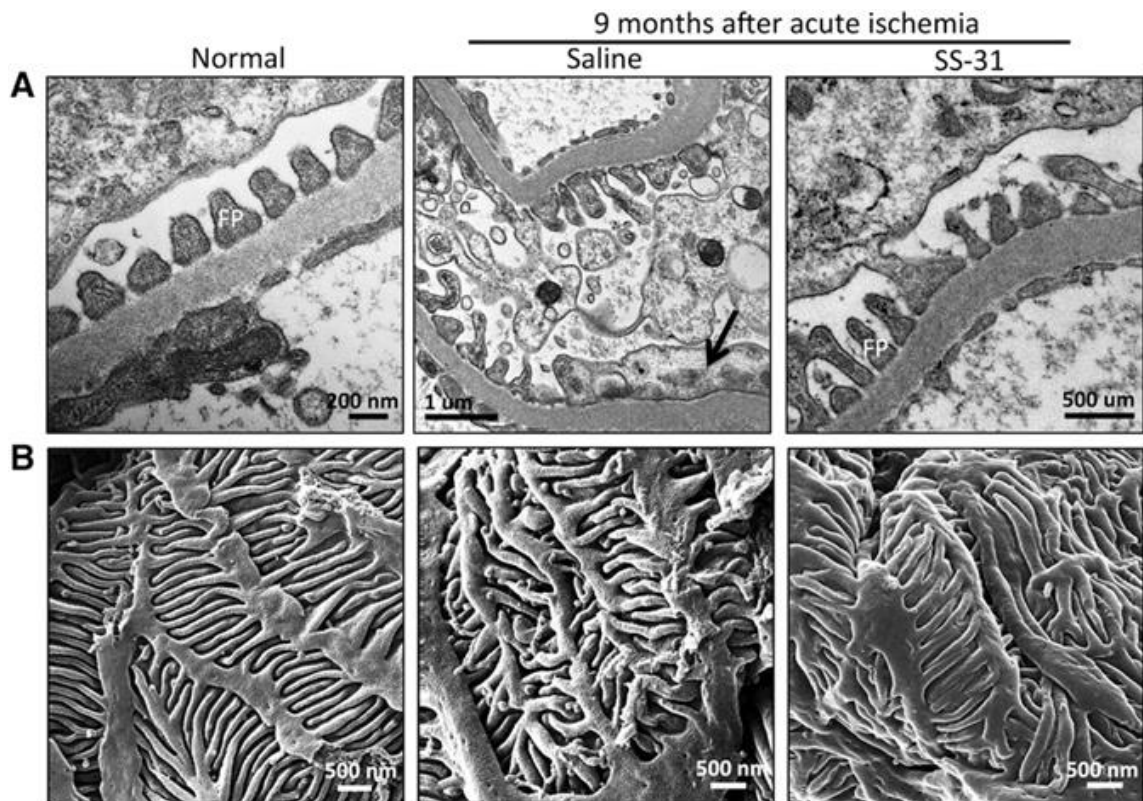


Figure 4.6 SS-31 preserves podocyte foot processes after acute ischemia. Rats were treated with SS-31 (2 mg/kg per day) or saline for 1.5 months starting 1 month after acute ischemia. Podocyte structure was examined 9 months after ischemia. (A) Representative images of podocyte foot processes obtained by transmission electron microscope. Podocyte swelling and foot process effacement are common 9 months after acute ischemia compared with age-matched control. Condensation of actin microfilaments can be seen in the flattened foot processes (black arrow). Short-term SS-31 treatment restores normal foot processes. (B) Representative images of podocyte foot processes obtained by helium ion microscope. In normal podocytes, the foot processes are long and tightly interdigitated. Ischemia resulted in shortened and deformed foot processes. Short-term SS-31 treatment restores normal structural organization of foot processes.

Ischemia causes extensive mitochondria damage in renal endothelial cells⁶¹. Normal glomerular endothelial mitochondria are elongated, with dense cristae membranes and a dark matrix (Figure 4.4C). Significant degenerative changes were still found in endothelial cells 2.5 months after ischemia, with loss of cristae membranes and matrix density, and evidence of rupture of the OMM. These degenerative changes were abolished by 6 weeks of treatment with SS-31.

SS-31 Prevents Podocyte Stress after Ischemia

Podocytes are secretory cells that contain a well developed Golgi system, many mitochondria, prominent lysosomes, and abundant endoplasmic reticulum (ER) responsible for the folding and trafficking of proteins (Figure 4.5A)⁶⁸. Transmission electron microscopy showed pronounced dilation of ER lumen, an indication of ER stress, in many podocytes 1 month after ischemia (Figure 4.5B) compared with sham rats (Figure 4.5A). By 2.5 months, the podocytes were highly vacuolated and there was a general loss of cytoplasmic density (Figure 4.5C). Podocyte stress was still apparent 9 months after ischemia (Figure 4.5D). However, 6 weeks of SS-31 restored normal ER structure (Figure 4.5E) and this persisted for at least 6 months after treatment (Figure 4.5F).

SS-31 Protects Podocyte Foot Processes after Ischemia

Podocytes have a complex cellular architecture with interdigitating foot processes maintained by a precise organization of actin filaments in the cellular cytoplasm. Podocyte swelling and effacement of foot processes have been reported after 45 minutes of ischemia in rats, but little is known about long-term changes after acute ischemia⁶⁹. Transmission electron microscopy revealed swollen podocytes and foot process effacement 9 months after acute

ischemia compared with age-matched controls (Figure 4.6A). Condensation of actin microfilaments can be seen in the flattened foot process. Short term SS-31 treatment restored normal foot processes. HIM provided a much clearer image of the damage to podocytes (Figure 4.6B). In normal podocytes, the foot processes are long and tightly interdigitated to provide an effective filtration barrier. Ischemia resulted in shortened and deformed foot processes that did not interdigitate well. Podocyte foot processes were normalized with SS-31 treatment.

SS-31 Reverses Ischemia-Induced Mitochondria Damage in Podocytes

Mitochondria play a major role in providing adenosine triphosphate (ATP) for maintaining the actin cytoskeleton in podocytes⁷⁰⁻⁷¹. The collapse of the podocyte actin cytoskeleton at 9 months suggests sustained mitochondrial damage after an acute event. Normal podocyte mitochondria are elongated with cristae membranes and a dark matrix (Figure 4.7A). One month after ischemia, mitochondria showed degenerative changes with loss of cristae membranes and matrix swelling (Figure 4.7B). These degenerative changes were extensive and persisted at 2.5 months, with some mitochondria showing destruction of the OMM (Figure 4.7C). At 9 months, most mitochondria were small with only remnants of cristae membranes and a clear matrix, whereas others underwent extensive proteolysis with just some residual matrix density (Figure 4.7, D–F). Six weeks of SS-31 treatment restored mitochondria structure (Figure 4.7G), and mitochondria remained normal even 9 months after ischemia (Figure 4.7H).

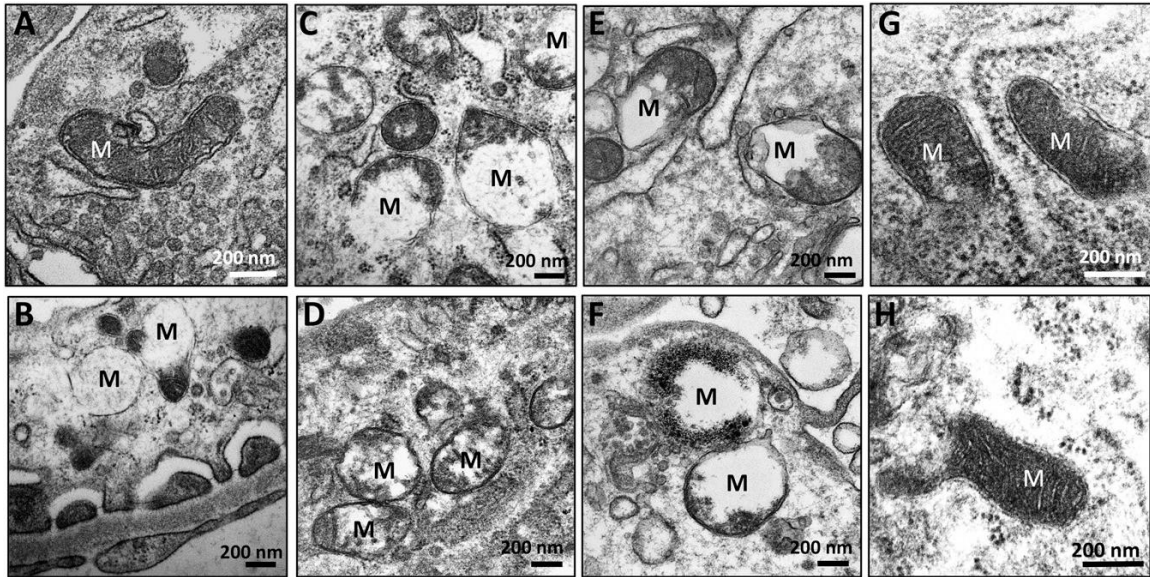


Figure 4.7 SS-31 reverses ischemia-induced mitochondria damage in podocytes. Rats were treated with SS-31 (2 mg/kg per day) or saline for 1.5 months starting 1 month after acute ischemia. Podocyte mitochondria were examined 9 months after ischemia using transmission electron microscopy. (A) Representative image from normal podocyte showing elongated mitochondria with cristae membranes and a dark matrix. (B) Representative image obtained 1 month after ischemia showing mitochondria with degenerative changes including loss of cristae membranes and matrix swelling. (C) Representative image obtained 2.5 months after ischemia showing persistent mitochondrial damage. (D–F) Representative images obtained 9 months after ischemia. Many mitochondria are small with remnants of cristae membranes and a clear matrix, whereas others have undergone extensive proteolysis. (G) Representative image obtained from an SS-31-treated rat 2.5 months after ischemia showing normal mitochondria cristae and matrix density. (H) Representative image from an SS-31-treated rat 9 months after ischemia showing normal podocyte mitochondria. M, mitochondria.

Persistent Upregulation of Autophagy in Podocytes after Ischemia

Accumulating evidence indicates that ER stress may trigger autophagy⁷². Postmitotic podocytes exhibit autophagy under basal conditions⁷³, but the effect of ischemia on podocyte autophagy is unknown. Autophagic vacuoles containing organelles and cytoplasmic contents can be seen in podocytes 1 month after ischemia (Figure 4.8A). Figure 4.8B shows an intact mitochondrion inside an autophagosome. Mitophagy is still upregulated 9 months after acute ischemia, with interaction between lysosomes and mitochondria (Figure 4.8, C and D). Autophagolysosomes containing digested material and myelin bodies are shown in Figure 4.8E.

Finally, Figure 4.8F shows an example of dilated ER wrapping around mitochondria to cause mitochondrial fission⁷⁴.

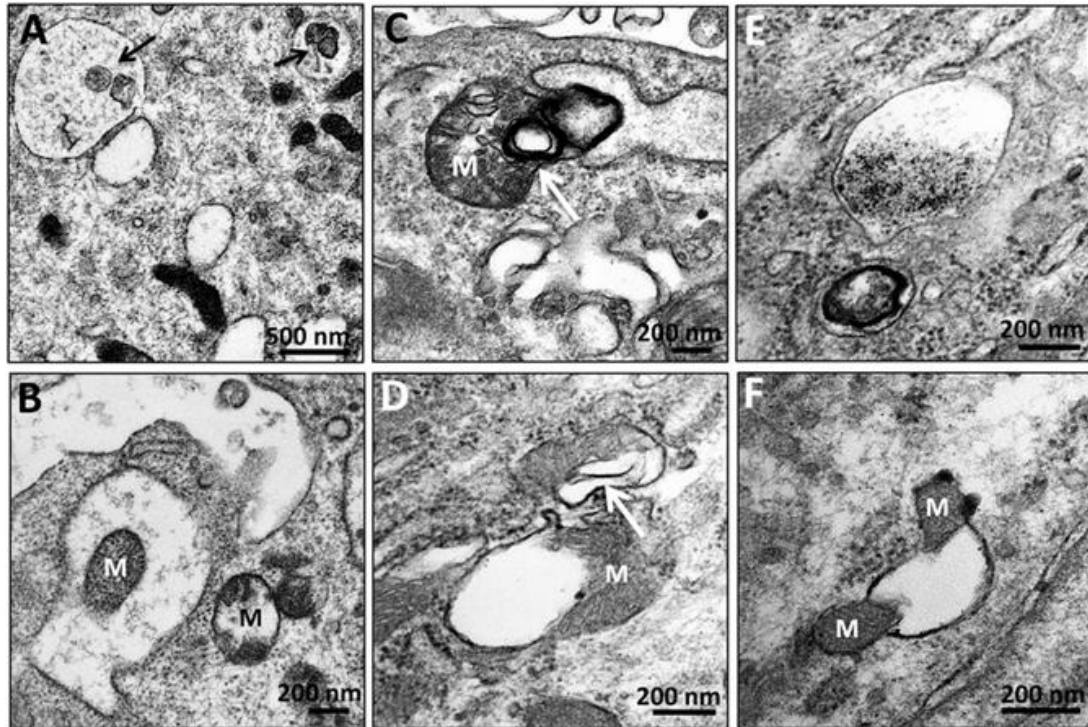


Figure 4.8 Persistent upregulation of autophagy in podocytes after acute ischemia. Rats were subjected to bilateral renal ischemia for 45 minutes and podocytes examined by transmission electron microscopy. (A) Autophagic vacuoles (arrows) containing organelles and cytoplasmic contents in podocytes 1 month after ischemia. (B) An intact mitochondrion (M) can be seen inside an autophagosome. (C and D) Interaction between lysosomes (arrows) and mitochondria (M) can be seen 9 months after ischemia. (E) Autophagolysosomes containing digested material and myelin bodies 9 months after ischemia. (F) Dilated endoplasmic reticulum wrapping around mitochondria (M) causing mitochondrial fission. M, mitochondria.

SS-31 Protects Proximal Tubule Mitochondria

Proximal tubules are highly susceptible to ischemic injury, with rapid loss of brush border and cell detachment⁵⁷⁻⁵⁸. However, tubular cells can regenerate, and brush provided a much clearer image of the damage to podocytes (Figure 4.6B). In normal podocytes, the foot processes are long and tightly interdigitated to provide an effective filtration barrier. Ischemia resulted in

shortened and deformed foot processes that did not interdigitate well. Podocyte foot processes were normalized with SS-31 treatment.

SS-31 Reverses Ischemia-Induced Mitochondria Damage in Podocytes

Mitochondria play a major role in providing ATP for maintaining the actin cytoskeleton in podocytes⁷⁰⁻⁷¹. The collapse of the podocyte actin cytoskeleton at 9 months suggests sustained mitochondrial damage after an acute event. Normal podocyte mitochondria are elongated with cristae membranes and a dark matrix (Figure 4.7A). One month after ischemia, mitochondria showed degenerative changes with loss of cristae membranes and matrix swelling (Figure 4.7B). These degenerative changes were extensive and persisted at 2.5 months, with some mitochondria showing destruction of the OMM (Figure 4.7C). At 9 months, most mitochondria were small with only remnants of cristae membranes and a clear matrix, whereas others underwent extensive proteolysis with just some residual matrix density (Figure 4.7, D–F). Six weeks of SS-31 treatment restored borders are intact 9 months after acute ischemia (Figure 4.9A). Unlike the elongated mitochondria found in normal proximal tubules, post-ischemic proximal tubule mitochondria are small and highly disorganized, and there is an abundance of lysosomes (Figure 4.9B). There is also evidence of mitophagy, with early and complete autophagosomes around mitochondria (Figure 4.9, C and D). Some autophagolysosomes contain cytoplasmic content or are completely homogenized (Figure 4.9, E and F). Autophagy was not observed in proximal tubules treated with SS-31.

In addition to mitophagy, some proximal tubule mitochondria appear relatively normal but have membrane vesicles in close apposition to the OMM (Figure 4.10, A–D). These vesicles may be dilated ER that are in close apposition to the OMM, commonly termed mitochondria-

associated membranes. These structures were not seen in rats that received SS-31 treatment (Figure 4.10, E and F).

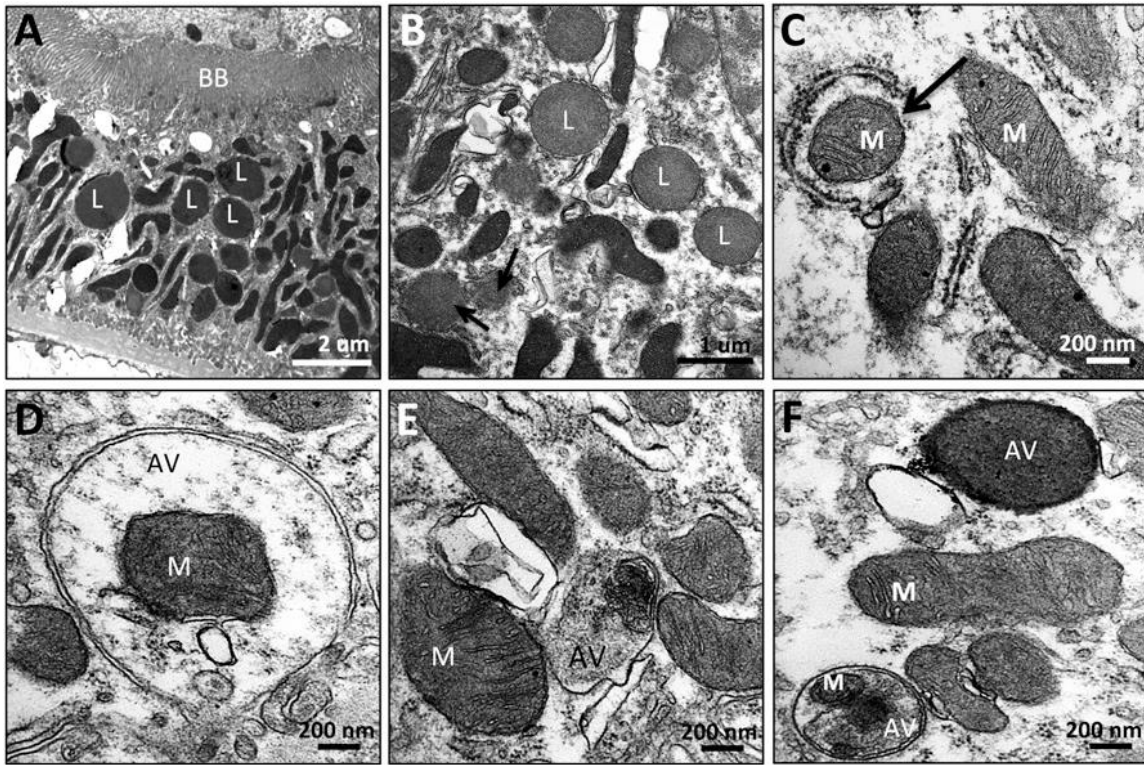


Figure 4.9 Mitophagy in proximal tubules after acute ischemia. Rats were treated with SS-31 (2 mg/kg per day) or saline for 1.5 months starting 1 month after acute ischemia. Proximal tubules were examined by transmission electron microscopy. (A and B) Representative images obtained 9 months after acute ischemia showing normal brush border (BB). Mitochondria are small and highly disorganized, and there is an abundance of lysosomes (L). (C and D) Representative images showing early and complete autophagic vesicles (AV) surrounding mitochondria (M). (E and F) Representative images showing autophagic vacuoles containing mitochondria and other cytoplasmic content.

4.3 Discussion

My colleagues previously reported peritubular and glomerular capillary loss, inflammation, tubulointerstitial fibrosis, and glomerulosclerosis 1 month after acute ischemia⁶¹. We confirm those earlier findings in this study, and further show persistent endothelial injury and microvascular rarefaction up to 9 months after acute ischemia, accompanied by podocyte damage, inflammation, and progressive glomerular and interstitial fibrosis. Although renal

function was not assessed in this study, significant proteinuria has been reported in rats 9 months after the same duration of ischemia⁷⁵.

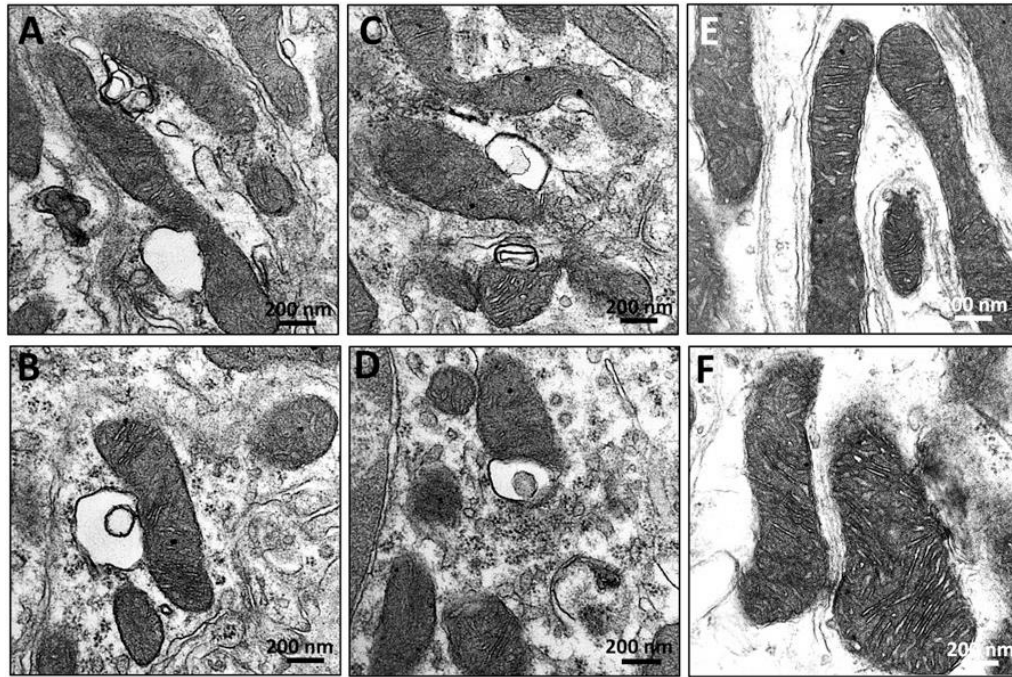


Figure 4.10 Mitochondria-associated membranes in proximal tubules after ischemia. Rats were treated with SS-31 (2 mg/kg per day) or saline for 1.5 months starting 1 month after acute ischemia. Proximal tubules were examined by transmission electron microscopy 9 months after ischemia. (A–D) Representative images showing membrane vesicles in close apposition to the OMM. (E and F) Representative images from SS-31-treated samples did not show these mitochondria-associated membranes.

Podocytes are terminally differentiated epithelial cells that form part of the filtration barrier. Even though there was no evidence of podocyte loss at 9 months, the cell bodies were swollen and foot processes were deformed and retracted, as revealed vividly by HIM. The complex structure of foot processes depends on ordered actin filament bundles, and the assembly and maintenance of the actin cytoskeleton require ATP⁷⁶. The breakdown of the actin cytoskeleton suggests bioenergetics failure in podocytes long after the acute ischemic insult. Ischemia causes mitochondrial swelling and loss of cristae membranes in all renal cells^{57-58, 61}, but it has not been appreciated that mitochondrial damage can persist for as long as 9 months. Damage to podocyte

mitochondria is extensive and most show loss of cristae membranes and homogenization, consistent with proteolytic degradation by mitochondrial proteases⁷⁷.

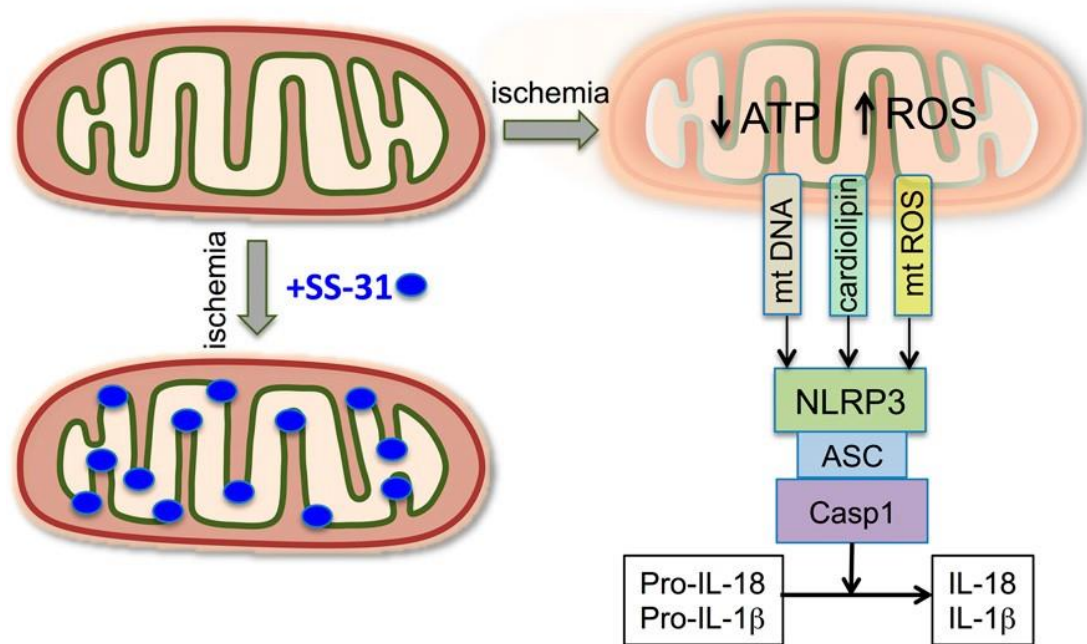


Figure 4.11 SS-31 protects mitochondrial integrity and prevents inflammasome activation and upregulation of IL-18 and IL-1b. Ischemia causes mitochondria damage resulting in decreased ATP production, increased ROS production, and cardiolipin peroxidation. Damage to mitochondrial membranes leads to the release of mitochondrial DNA (mt DNA), mitochondrial reactive oxygen species (mt ROS), and cardiolipin that are known to activate the NLRP3 inflammasome. The NLRP3 inflammasome, together with the adaptor protein (ASC), triggers activation of caspase-1 (Casp1), which then processes the proinflammatory cytokines pro-IL-1b and pro-IL-18 into their bioactive mature forms (IL-1b and IL-18). SS-31 (blue dots) targets cardiolipin, inhibits cardiolipin peroxidation, and protects mitochondrial cristae membrane. By preserving mitochondrial integrity, SS-31 not only preserves ATP production but also prevents NLRP3 inflammasome activation and normalizes IL-18 and IL-1b expression. ASC, Apoptosis-associated speck-like protein containing a caspase-recruitment domain.

The accumulation of damaged mitochondria in podocytes suggests that mitochondrial quality control remains impaired long after acute ischemia. Mitochondria undergo regular cycles of degradation and biogenesis in order to maintain an efficient supply of ATP to the cell. Mitophagy serves as a rapid removal mechanism for whole dysfunctional mitochondria or a large number of damaged mitochondria. Autophagosomes containing mitochondria and

autophagolysosomes were apparent in both podocytes and proximal tubules 9 months after ischemia. However, a large number of podocyte mitochondria appear to undergo proteolytic degradation suggesting that mitophagy might be impaired, and damaged proteins are eliminated by mitochondrial proteases⁷⁸.

Our results suggest that persistent mitochondrial damage underlies the progression of CKD, and this was confirmed with the mitoprotective agent SS-31. Treatment with SS-31 before ischemia protected endothelial and epithelial mitochondria, preserved peritubular and glomerular capillaries, and prevented inflammation and fibrosis⁶¹. Here we show that SS-31, started 1 month after ischemia, can repair mitochondria in endothelial cells, podocytes, and tubular cells. This led to restoration of peritubular and glomerular capillaries, preservation of podocyte architecture, suppression of inflammation, and fibrosis. SS-31 abolished the increase in TNF- α and TGF- β over the 6-week treatment interval. Remarkably, renal protection persisted for at least 6 months after termination of SS-31 treatment. No other experimental treatment has been shown to accomplish this when given so late after AKI. Most experimental treatments evaluated in animal studies are given prior to or shortly after acute injury, although the clinical reality is that most patients present with established disease.

SS-31 protects mitochondrial structure by interacting with cardiolipin on the inner mitochondrial membrane and protecting cristae structure^{58, 79-80}. Cardiolipin promotes membrane folding and promotes respiratory complexes to form supercomplexes to facilitate electron transfer, promote ATP synthesis, and reduce electron leak. Dysfunctional mitochondria generate ROS, and cardiolipin is particularly susceptible to lipid peroxidation. In the presence of ROS, cytochrome c acts as a peroxidase and causes cardiolipin peroxidation and cristae degradation. SS-31 acts as a multifunctional antioxidant by minimizing electron leak, scavenging excess electrons, and inhibiting cytochrome c peroxidase activity^{60, 79, 81}. SS-31 has been reported to

restore cardiolipin content and mitochondrial cristae structure, and improve mitochondrial energetics, in experimental models of chronic kidney and heart failure⁸²⁻⁸⁴. The recovery of podocyte bioenergetics allowed repair of the actin cytoskeleton and podocyte structure.

Inflammation plays a major role in sustaining fibrosis after acute injury. However, TNF- α and macrophage infiltration were already on the decline at 9 months. Inflammasome activation may be responsible for sustaining inflammation long after acute ischemia. Mitochondria play an integral role in the assembly and activation of the inflammasome^{46, 51}. Release of mitochondrial DNA, ROS, and cardiolipin from damaged mitochondria can activate the NLRP3 inflammasome (Figure 4.11)^{45, 55-56}. There was sustained increase in IL-18 and IL-1b expression 9 months after acute ischemia, supporting a role for inflammasome activation in the progression to CKD. Cardiolipin peroxidation causes the translocation of cardiolipin to the OMM where it has been proposed to serve as a docking site for inflammasome assembly, whereas mitochondrial ROS activates the inflammasome to produce caspase-1.^{46, 56} Mitochondria-associated membranes are also involved in the formation of the inflammasome⁸⁵, and they were prominent in proximal tubules 9 months after ischemia. By inhibiting mitochondrial ROS production, preventing cardiolipin peroxidation, and protecting mitochondrial cristae structure, SS-31 prevented the upregulation of IL-1b and IL-18 after acute renal ischemia (Figure 4.11). Inflammasome activation also contributes to renal inflammation and fibrosis in the mouse unilateral ureteral obstruction (UUO) model,^{46, 86} and SS-31 can prevent interstitial fibrosis after UUO.⁸⁷ SS-31 has also been reported to attenuate inflammasome activation in alveolar cells in response to mechanical ventilation⁸⁸, and in the brain of aging mice in response to isoflurane⁸⁹.

Several inhibitors of IL-1b and IL-18 are in clinical development, as well as inhibitors of the NLRP3 inflammasome and caspase-1⁹⁰⁻⁹¹. Targeting upstream of the inflammasome might prove more effective than single anticytokine therapies and carry less risk. SS-31 has been shown

to be highly effective in preventing acute and chronic kidney injury, including ischemia reperfusion injury, UUO, contrast dye, endotoxemia, and streptozotocin-induced diabetic kidney injury^{57, 61, 87, 92-94}. SS-31 has also been reported to reverse progressive CKD after chronic ischemia caused by renovascular stenosis, and reduce glomerulopathy and tubular injury caused by high-fat diet⁹⁵⁻⁹⁶. SS-31 (also known as MTP-131, elamipretide, and Bendavia) may represent a novel treatment for CKD in addition to BP control.

4.4 Concise Methods

Animals

The study was performed using male Sprague–Dawley rats (Charles River Laboratories, Wilmington, MA) weighing 250–300 g. Animals were housed in 12:12-hour light/dark cycle and allowed free access to water and standard rat chow. Care of the rats before and during the experimental procedures was conducted in accordance with the policies of the National Institutes of Health Guidelines for the Care and Use of Laboratory Animals. All protocols had received prior approval from the Weill Cornell Medical College Institutional Animal Care and Use Committee.

Materials and Materials

SS-31 was supplied by Stealth Peptides Inc.,
Newton Centre, MA. Unless otherwise specified, reagents and assay kits were purchased from Sigma-Aldrich (St. Louis, MO).

Ischemia-Reperfusion Experimental Protocol

Rats were anesthetized with ketamine/xylazine and bilateral renal ischemia was induced by application of nontraumatic microvascular clamps around both left and right renal pedicles for

45 minutes, as previously described in detail⁵⁷. After ischemia, the animals were allowed to recover for 1 month. Surviving rats were randomly assigned to 6 weeks of treatment with SS-31 (2.0 mg/kg per day) or saline by subcutaneously implanted osmotic pump (Alza, Cupertino, CA). Rats were euthanized either immediately after drug treatment or 6 months after termination of drug treatment. Kidneys were harvested for biochemical and histologic analysis. Kidney tissues were frozen at -80°C for Western blotting or embedded in OCT-cryostat sectioning medium containing 30% sucrose for immunohistochemistry. Other samples were fixed in 4% paraformaldehyde for paraffin sections and ultrastructural examination by transmission electron microscopy or HIM.

Renal Histopathology

Paraffin sections (3 mm) were stained with periodic acid–Schiff and examined by light microscopy (Nikon Eclipse TE2000-U). Masson trichrome staining was used to assess interstitial fibrosis and glomerulosclerosis.

Assessment of Renal Microvasculature

Microvascular density and endothelial injury were assessed by immunohistochemical staining of CD31 and vWF, respectively. Frozen OCT blocks were cut into 8 mm sections, fixed in acetone for 4–5 minutes at room temperature, and incubated with anti-mouse CD31 (BD Biosciences, San Jose, CA) and anti-rabbit vWF (Sigma-Aldrich) overnight at 4°C. Sections were then incubated with anti-mouse IgG-conjugated Alexa Fluor-488 (Invitrogen, Carlsbad, CA) or goat anti-rabbit IgG-conjugated with biotin (Vector Laboratories, Burlingame, CA), and then treated with streptavidin-conjugated Alexa Fluor-594 (Invitrogen) for 30 minutes at room temperature, covered with VECTASHIELD Mounting Medium with DAPI (Vector Laboratories), and imaged by

fluorescence microscopy (Nikon Eclipse TE2000-U). For each animal, ten representative glomeruli were selected in the renal cortex, and the green fluorescence intensity of the CD31 immunostain was quantified (ImageJ; National Institutes of Health) and averaged. Similarly, ten representative areas of the inner stripe of the outer medulla were quantified and averaged.

Assessment of Renal Inflammation

Macrophages were assessed by immunohistochemical staining of 4 mm paraffin sections for CD68. The kidney sections were incubated with anti-mouse CD68 (Abcam, Inc., Cambridge, MA) overnight at 4°C and incubated with HRP-conjugated anti-mouse IgG (Dako, Carpinteria, CA) for 30 minutes at room temperature, and color developed by DAB substrate kit (Vector Laboratories). The number of CD68+ cells were counted from five different fields for each sample and averaged.

The cytokines TNF- α , TGF- β 1, IL-18 and IL-1 β were quantified by Western blotting. Kidney homogenates were prepared according to standard protocol (Santa Cruz Biotechnology, Santa Cruz, CA), suspended in loading buffer, and subjected to 4%–15% SDS-PAGE. The resolved proteins were transferred to an Immuno-Blot polyvinylidene difluoride membrane (Bio-Rad, Hercules, CA). After electroblotting, the membrane was incubated overnight with primary antibodies against TNF- α (ab1793; Abcam, Inc.), TGF- β (sc-146; Santa Cruz Biotechnology), IL-18 (MAB521; R&D Systems, Minneapolis, MN), and IL-1 β (MB5011; R&D Systems). Membranes were further incubated for 1 hour with HRP-conjugated secondary antibodies (Dako). Protein bands were detected with an enhanced chemiluminescence detection system (Bio-Rad) and autoradiography. Bands were evaluated for integrated density values on Image Lab Software (Bio-Rad).

Transmission Electron Microscopy Pieces of renal tissue were fixed in 4% paraformaldehyde, postfixed in 1% osmium tetroxide, dehydrated in graded alcohols, and embedded in Epon. Ultrathin sections (200–400 Å) were cut on nickel grids, stained with uranyl acetate and lead citrate, and examined using a digital electron microscope (JEM-1400; JEOL Ltd.).

HIM

Kidney tissues were sectioned at 500 μ m on a Leica vibrating microtome. The slices were cut into smaller, wedge-shaped pieces so that they would remain flat during the drying process. Tissues were dehydrated through a graded PBS-MeOH series at 4°C, according to previously published methods⁶⁷. Tissues were subjected to critical point drying with CO₂. Dried samples were mounted on scanning electron microscope stubs using carbon sticky tabs and stored in a desiccator until imaging. HIM was carried out on the Carl Zeiss Orion Plus helium ion microscope (Carl Zeiss GmbH, Jena, Germany) operating at 30 keV acceleration voltage, with a beam current of approximately 0.5 pA. A 10 nm layer of Au was evaporated on the samples to minimize local charging effects. For all images taken, an electron flood gun was used for charge neutralization at an accelerating voltage of 900 eV. The vacuum reading in the analysis chamber was 2.3e-7 torr.

Statistical Analyses

Results are expressed as means \pm SEM. Statistical analysis was carried out using Prism software (GraphPad Software Inc., San Diego, CA). Multiple group comparisons were performed using ANOVA followed by a Tukey post hoc test. A P value, 0.05 was considered statistically significant.

Chapter 5

Biological control of aragonite formation in stony corals

This chapter is based on a paper published in Science (journal)⁹. My contributions to the paper include providing Helium Ion Microscopy imaging and characterization and optimization of the sample preparation protocols for the HIM. This chapter is a second demonstration (following chapter 4) of a specialized biological application of He ion microscopy, as described in earlier chapters.

5.1 Introduction

The detailed mechanism of coral biomineralization, *i.e.* the process by which stony corals precipitate their calcium carbonate skeletons in the form of aragonite, has been extensively discussed for decades without the emergence of a clear consensus⁹⁷⁻⁹⁹. There are two prevailing hypotheses. Geochemists generally advocate for an abiotic, physicochemical process¹⁰⁰⁻¹⁰¹ based on complex metabolic controls of calcifying fluid chemistry; while, in contrast, biologists plead for a biologically controlled process¹⁰²⁻¹⁰⁸ mediated by the skeletal organic matrix (SOM)¹⁰⁹⁻¹¹¹. The first scenario describes a spontaneous precipitation of aragonite due to an increase in the concentrations of calcium, dissolved inorganic carbon (DIC) species and pH at the calcification site compared to seawater¹¹²⁻¹¹⁸. Such a mechanism implies a homogeneous nucleation of the solid mineral phase, followed by a classical crystal growth *via* ion-by-ion attachment. The latter scenario depicts the SOM¹¹⁹⁻¹²⁴ (mostly proteins and sugars), in particular acidic proteins¹²⁵⁻¹²⁹, as directly responsible for the precipitation of aragonite¹¹¹. Such a

mechanism implies a heterogeneous nucleation of the solid mineral phase, potentially followed by a non-classical crystallization route¹³⁰ which is more likely to happen in natural biomaterials¹³¹.

An abiotic mineralization pathway would appear to be more sensitive to ocean acidification¹³² because it is directly related to carbonate chemistry. However, a biologically controlled process may be more robust because it catalyzes the formation of aragonite based on processes that are far from thermodynamic equilibrium. In this paper, we examine which of these two opposing paradigms occurs in stony corals. Our primary goal is to elucidate the mechanism of biomineralization and in so doing to predict if corals will maintain the ability to precipitate their skeletons in coming centuries. To this end, we have used the ubiquitous IndoPacific, stony coral *Stylophora pistillata* as a model for investigating the coral biomineralization process. The genome for this organism is completely sequenced¹³³, and a proteome for the skeletal organic matrix has been previously published¹²⁰. Here we applied a unique material science approach that combines structural, analytical and imaging tools rarely or never used for characterizing coral skeleton. The approach includes Raman spectroscopy and imaging, helium ion microscopy (HIM) and solid-state nuclear magnetic resonance (NMR) spectroscopy. The latter provides unprecedented insights into the relation between the mineral phase and the SOM across different spatial scales. Further, the ultra-high-resolution three-dimensional images collected by HIM reveal the crystallization pathway of coral aragonite.

5.2 Features common to all stony corals

Low magnification scanning electron micrographs of the skeletal architecture of *Stylophora pistillata* reveal juxtaposed cup-like structures (*i.e.* calices) whose calcareous walls constitute the corallites (Figure 5.1-A). The corallites are the sites in which the individual polyps

resided when the coral was alive; they are therefore the sites in which both the SOM is secreted and the mineral phase is initially deposited. A representative higher magnification image of a single corallite reveals “dark lines” structures observable along the different micro-orphological elements of the skeleton: the columella, the septa and the theca (Figure. 5.1-B). These sites, which appear to be enriched in organic molecules, correspond to the “centers of calcification” (COCs)¹³⁴, also termed “early mineralized zone” (EMZ)¹³⁵ or “deposits of Centers of Rapid Accretion” (dCRA)¹³⁶; are the initial sites of biomineralization¹³⁷⁻¹³⁹. Higher resolution micrographs

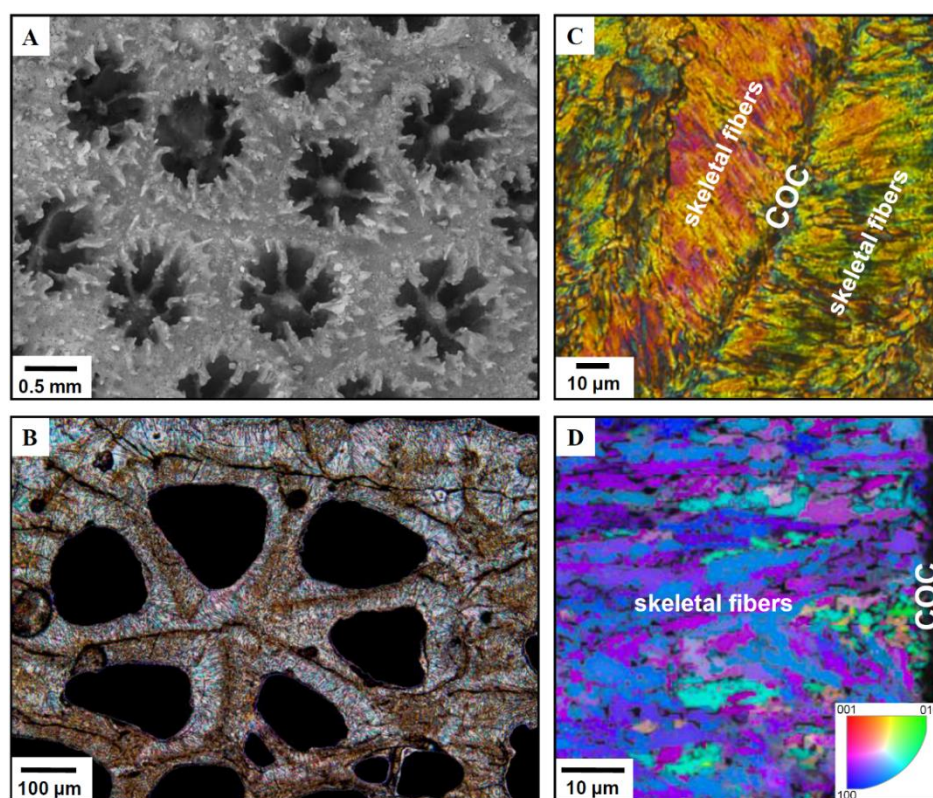


Figure 5.1 Morphological skeletal features common to all stony corals. (A) A combination of multiple scanning electron microscopy (SEM) micrographs obtained on the surface of an intact skeletal branch in which numerous corallites are observable. (B and C) Transmitted PLM micrographs from a polished thin section of coral skeleton. The region in (B) is an individual corallite, in which the surface normal corresponds to the vertical axis of the former calyx. The “dark-lines” discernible in the image correspond to COCs; while the region in (C) is a trabecula composed of skeletal fibers that radiate from the COC. (D) EBSD inverse pole figure orientation map of a trabecula from a polished thin section of coral skeleton.

using polarized light microscopy (PLM) and electron backscatter diffraction (EBSD) give direct evidence that acicular aragonite crystals are oriented outward from the COCs with homogeneous crystallographic orientations (Figures. 5.1; C & D). The latter form densely-packed, ordered structures called skeletal fibers, that are the building blocks of the skeleton. These images suggest that the skeletal fibers arise from the organic-matter-rich environments that constitute the COCs, implying that SOM is critical for initiating the deposition of the mineral phase.

5.3 Spatial distribution of the SOM and orientation of the skeletal fibers

To confirm that biomineralization is initiated in the COCs and involves the SOM, we first applied confocal Raman microscopy (CRM). This technique combines imaging and spectroscopic capabilities, and can provide crucial information for determining the spatial distribution of the SOM and the orientation of the skeletal fibers^{116, 140-141}. The orientation of the skeletal fibers was visualized with the help of two characteristic Raman bands of aragonite (Figures. 5.2; A1, A2 & B1, B2); while the spatial distribution of the SOM was mapped based on the fluorescence signal (Figures. 5.2; A3 & B3). These Raman maps were generated so that the brightest areas observable in the images coincide with the highest intensity of the considered band or signal. Two trabeculae are clearly observable, in which skeletal fibers radiate from relatively small areas displaying high fluorescence intensity that correspond to COCs. These correlative observations illustrate that, in this organism, the COCs have an elongated shape in the longitudinal axis and a round shape in the transverse axis. The concentric organic-rich layers around the COCs, which are barely visible in Figures. 5.2 (A3 & B3) (thickness, $\approx 1 \mu\text{m}$), are part of the incremental growth lines of the mineral phase within the skeletal fibers^{104, 135}.

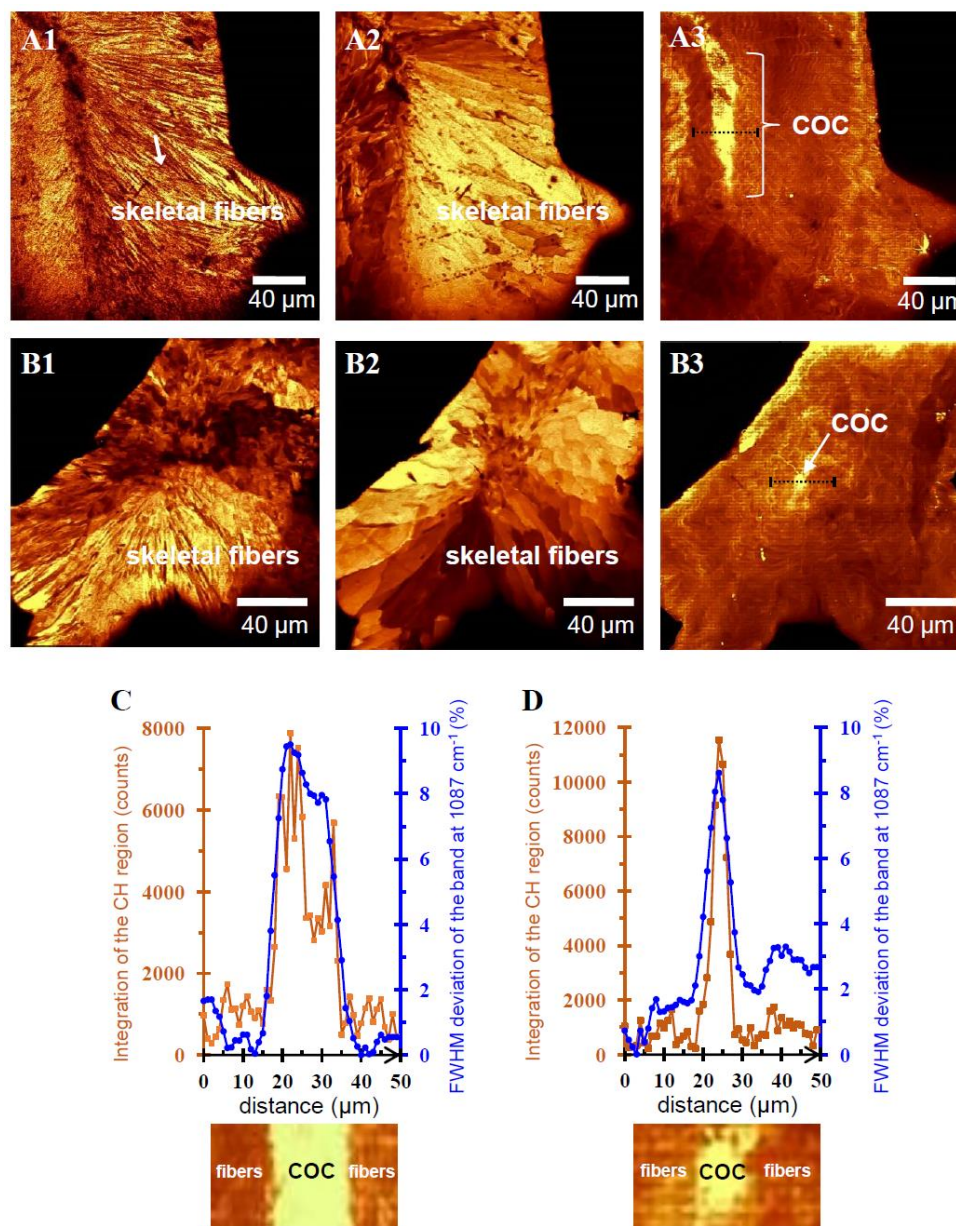


Figure. 5.2 Structural and chemical characterization of the centers of calcification. (A and B) CRM maps obtained from two polished cross sections of coral skeleton. These images show a representative section in the longitudinal plane (A), and the transverse plane (B) along a skeletal branch (*i.e.* perpendicular and parallel to the vertical axes of the calices, respectively). Three different Raman maps were generated, based on the relative intensity distribution of: two characteristic Raman bands of aragonite, *i.e.* the (v1) symmetric stretching mode of the CO_3^{2-} at 1087 cm^{-1} (1) and the translational lattice mode at 152 cm^{-1} (2); the background signal in the range $2400\text{--}2700\text{ cm}^{-1}$, related to the intrinsic fluorescence caused by the presence of organic compounds across the skeleton (3). (C and D) 50 μm long Raman spectroscopy profiles recorded across the trabeculae exposed in (A) and (B), respectively (dashed black lines). These profiles consist of 50 single Raman spectra recorded every 1 μm. The orange curves were obtained by integrating the signal of the $\text{sp}^3\text{ CH}_x$ stretching modes, while the blue curves were obtained by fitting the FWHM of the band ascribed to the (v1) symmetric stretching mode of the CO_3^{2-}

5.4 Chemical heterogeneity in the mineral phase

To further elucidate the spatial distribution of the SOM and its relation with the mineral phase, Raman spectroscopy profiles were recorded across the two trabeculae exposed by CRM (Figures. 5 . 2; C & D). In contrast with the time-consuming Raman maps that are composed of approximately 200,000 spectra each, the Raman profiles here were recorded with a long integration time (*i.e.* 40 sec vs 0.5 sec). These two profiles were recorded twice for both detecting the signal from the SOM and structurally characterizing the mineral phase. The presence of organic material across the skeleton was unambiguously revealed; there is a characteristic signal of the $\text{sp}^3 \text{CH}_x$ stretching modes in the region of $2850\text{-}3000 \text{ cm}^{-1}$. This signal, integrated for each of the 50 single Raman spectra (oranges curves), clearly demonstrates that the SOM is concentrated in the COCs. A broadening of the aragonite band at 1087 cm^{-1} , ascribed to the (ν_1) symmetric stretching mode of the CO_3^{2-} units, was found in the COCs compared to in the adjacent skeletal fibers. This band was fitted in each of the 50 single Raman spectra to extract the full width at half maximum (FWHM), and that parameter was traced across the COCs (blue curves). This analysis clearly indicates that there is a progressive broadening from the skeletal fibers to the middle of the COCs in which the FWHM deviation reaches up to approximately 10 %. This broadening is diagnostic of chemical heterogeneity in the mineral phase, and suggests the presence of “immature” aragonite particles which are spatially closely related to the SOM in the COCs.

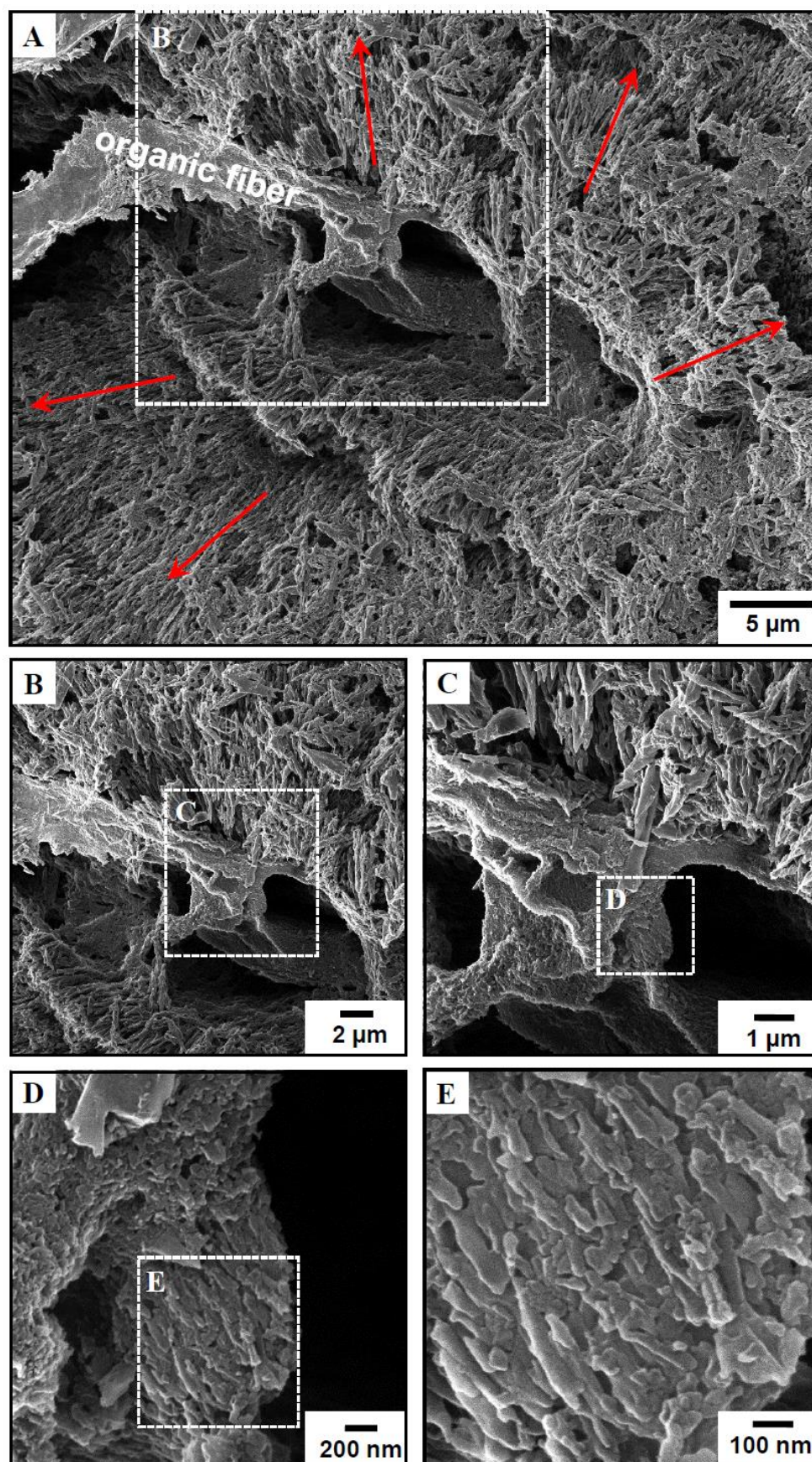


Figure. 5.3 Ultra-high-resolution three-dimensional images of organic material in a COC. (A, B, C, D and E) HIM micrographs obtained from the broken, but not polished, surface of a skeletal branch. The region in (A) is a trabecula composed of skeletal fibers that radiate (red arrows) from the COC. An organic fiber is observable in the COC exposed in (A). (B to E) are successive magnifications that progressively reveal the features of the organic fiber surface. The skeletal branch used here was transversely sectioned (*i.e.* parallel to the vertical axes of the calices), and then etched in a dilute aqueous solution of acetic acid upon weak agitation for 15 minutes

5.5 Relation between the initial mineral deposits and the SOM in the COCs

To further explore the role of the SOM in the COCs, we applied HIM which provides ultra-high three-dimensional resolution (Figure. 5.3). A COC is clearly identified given the direction of the radiating skeletal fibers (Figure. 5.3-A). In this image, the remaining organic material is observable in the form of a $\simeq 3 \mu\text{m}$ thick fiber that is extended perpendicular to the plane in which the aragonite crystals grow. Four successive magnifications micrographs clearly reveal the presence of nano-sized particles intercolated in the organic fiber surface (Figures. 5.3; B, C, D & E); while the crystals associated with the skeletal fibers observable here are micro-sized acicular aragonite crystals with a length that reaches up to several micrometers. These observations thereby suggest that the SOM concentrated in the COCs forms a solid organic substrate upon which the solid mineral phase is nucleated.

5.6 Detection of carbonates at the mineral-organic interface

We hypothesized that such heterogeneous nucleation event gives rise to atomic-scale spatial proximity between specific bio-organic molecules and the mineral phase exposed to the mineral- organic interface. To test this hypothesis, we applied solid-state NMR spectroscopy, which is one of the best suited techniques for elucidating the mineral-organic interface in hybrid materials¹⁴². One approach to spectroscopically examine this type of structures is based on the

^1H ^{13}C cross polarization (CP) experiment¹⁴³⁻¹⁴⁸. This experiment consists of a CP magnetization transfer from ^1H nuclei to nearby ^{13}C nuclei. The latter leads to the detection of carbon species localized in hydrogen-rich chemical environments; namely the organic matrix and the inorganic carbonates exposed to the mineral-organic interface (*i.e.* the interfacial carbonates). In parallel, the inorganic carbonates constituting the internal structure of the mineral particles (*i.e.* the bulk of the carbonates) can be selectively exposed using a single pulse ^{13}C NMR experiment. The latter leads to the detection of all the ^{13}C spins present in the skeleton, and thus gives rise to a ^{13}C quantitative spectrum as soon as the relaxation delay (d1) used is long enough to allow the signals to relax fully. We applied this approach to an intact and living coral branch with its polyps that was totally hydrated during the analysis, as well as from a skeletal branch that was dried and powdered.

The quantitative spectra of the bulk of the carbonates display a single resonance; the latter is symmetric and centered at $\delta(^{13}\text{C}) = 171.0$ ppm which is characteristic of crystalline aragonitic environments¹⁴⁹. In contrast, the interfacial carbonates spectra display a much broader resonance which is dissymmetric, and whose maximum intensity is slightly lower (*i.e.* $\delta(^{13}\text{C}) = 170.7$ ppm). The broadening strongly implies that the interfacial carbonates form highly disordered environments. They could potentially take the form of a few nanometers thick amorphous surface layer^{146, 150} that surrounds the aragonite crystals. This is the first evidence of the presence of such disordered environments in coral aragonite, and the extremely rigorous experiments conducted here on a living coral demonstrate that they do not originate from an artifactual precipitation caused by the drying process.

To further understand the nature of these disordered environments, we prepared two different, protein-free, synthetic aragonite samples *in vitro* following the protocol described by

Wang *et al.*¹⁵¹. One was precipitated from $\text{CaCl}_2 \cdot 2\text{H}_2\text{O} + ^{13}\text{C}$ -urea (called aragonite-1); while the second was precipitated from sea water + ^{13}C -urea (called aragonite-2). X-ray diffraction (XRD) observations clearly show that aragonite is the only crystalline phase. We also applied ^{13}C -based NMR experiments, and the important width of the resonances in the cross-polarized spectra compared to the resonances in the quantitative spectra clearly demonstrates the presence of analogous highly-disordered environments in these protein-free synthetic aragonites. These observations confirm that the disordered environments detected in coral skeleton are inorganic carbonates.

5.7 Investigation into the mineral-organic interface

These disordered carbonates were used as a starting point for further investigating into the interfacial regions to probe the presence of neighboring bio-organic molecules. To do this, we employed the two-dimensional (2D) ^1H ^{13}C NMR Heteronuclear Correlation (HetCor) experiment (Figure. 5.4). The latter is a 2D version of the ^1H ^{13}C CP experiment, and reveals both the ^1H and ^{13}C chemical environments of hydrogen-bearing species. This approach can reveal the spatial proximities among the various hydrogen and carbon species in the SOM and in the interfacial regions. These spatial proximities are detected in the form of correlation peaks in the 2D ^1H ^{13}C NMR HetCor spectra, in which the carbon environments (displayed along the horizontal dimension, F2 dimension) are correlated with their respective hydrogen environments (displayed along the vertical dimension, F1 dimension). Three 2D ^1H ^{13}C NMR HetCor experiments were recorded using three different CP times: $t_{\text{cp}} = 1, 4$ and 8 ms. The normalized one-dimensional (1D) ^1H and ^{13}C projections of the F1 and F2 dimensions, respectively, are shown in Figures. 5.4 (A & B). Evidence of skeletal proteins

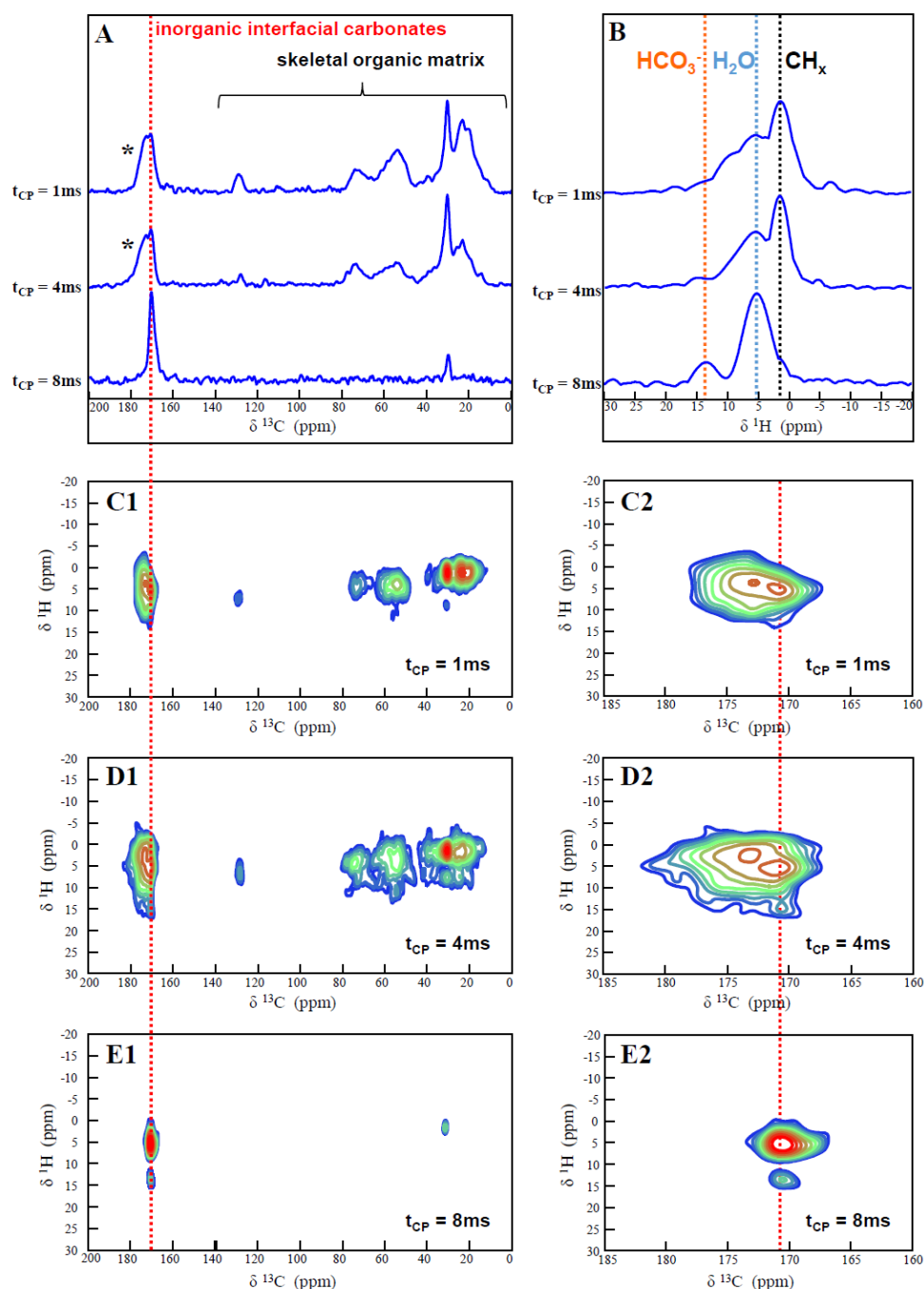


Figure 5.4 Spatial correlations between proton and carbon species in coral skeleton. **(A and B)** Normalized 1D ^1H and ^{13}C projections of the F1 and F2 dimensions, respectively, extracted from the 2D ^1H & ^{13}C NMR HetCor spectra displayed in **(C1, D1 and E1)**. The latter were recorded with three different CP times, $t_{CP} = 1\text{ ms}$ (C1), $t_{CP} = 4\text{ ms}$ (D1) and $t_{CP} = 8\text{ ms}$ (E1). **(C2, D2 and E2)** Enlargements of the interfacial carbonates regions observable at 170.70 ppm in the ^{13}C dimension (red dashed lines) extracted from (C1), (D1) and (E1), respectively. These solid-state NMR experiments were recorded from an entire skeletal branch that was powdered prior to be inserted into the rotor

and sugars is observable in the form of: (i) various ^{13}C resonances of the proteins' side chains in the aliphatic carbon region (in the range of $\delta(^{13}\text{C}) = 10\text{-}65$ ppm) and in the aromatic carbon region ($\delta(^{13}\text{C}) = 130$ ppm); (ii) an intense ^{13}C resonance from amide, carbonyl and carboxylate groups which belong to proteins in the range of $\delta(^{13}\text{C}) = 172\text{-}180$ ppm (see the black asterisk); as well as (iii) a broad ^{13}C resonance centered at $\delta(^{13}\text{C}) = 73$ ppm from sugar ring carbons.

The method employed here is a powerful spectral editing tool for enhancing (short CP time, *i.e.* $t_{\text{cp}} = 1$ ms) or suppressing (long CP time, *i.e.* $t_{\text{cp}} = 8$ ms) the signal from the SOM. The corresponding 1D ^1H projections (Figure. 5.4-B) display the signals of the hydrogen species whose ^1H spins have transferred their magnetization to neighboring ^{13}C spins during the CP magnetization transfer. These projections can thus be used to evaluate the nature of the hydrogen species bound to the SOM, *i.e.* aliphatic hydrogens and water molecules detected at $\delta(^1\text{H}) = 1.2$ ppm and $\delta(^1\text{H}) = 5.2$ ppm, respectively (observed at $t_{\text{cp}} = 1$ ms); as well as the hydrogen species present in the interfacial regions, *i.e.* water molecules and hydrogen-carbonate ions detected at $\delta(^1\text{H}) = 5.2$ ppm and $\delta(^1\text{H}) = 14.2$ ppm, respectively (observed at $t_{\text{cp}} = 8$ ms). These indirect observations were confirmed with the help of the different 2D ^1H ^{13}C NMR HetCor spectra (Figures. 5.4; C1, D1 & E1), from which the interfacial regions have been enlarged (Figures. 5.4; C2, D2 & E2). As evidenced above, the hydrogen and carbon environments of the interfacial regions are individually exposed with a long CP time, $t_{\text{cp}} = 8$ ms (Figure. 5.4-E2). The presence of two correlation peaks both observable at 170.70 ppm in the ^{13}C dimension demonstrates the presence of at least two different inorganic carbonate species, attributed to CO_3^- ions near H_2O (observable at $\delta(^1\text{H}) = 5.2$ ppm) and HCO_3^- ions (observable at $\delta(^1\text{H}) = 14.2$ ppm) according to their chemical shifts in the ^1H dimension. The 2D ^1H ^{13}C NMR HetCor experiment was also applied to the two protein-free synthetic aragonites. A ^1H signal centered around 1.2 ppm is also detected in the highly-disordered environments of both aragonite-1 and aragonite-2. The latter cannot be

attributed here to aliphatic hydrogens given the absence of proteins, but might rather be due to the presence of hydroxyl ions¹⁵². Moreover, hydrogen-carbonate ions in disordered environments are also evidenced in the synthetic aragonite sample precipitated from sea water, aragonite-2. These results, respectively, confirm and suggest the presence of HCO_3^- and OH^- ions within the mineral phase associated with the interfacial regions of coral skeleton.

These HCO_3^- ions were used as a starting point for probing the presence of neighboring bioorganic molecules. Whereas the rare, comparable studies in the literature present only two extreme CP times to selectively expose the organic material or the interfacial carbonates in nacre^{143, 145}, an intermediate CP time (*i.e.* $t_{\text{cp}} = 4$ ms) is presented here. This CP time enables to simultaneously expose both the various ^{13}C signals from the SOM and the ^1H signal from the HCO_3^- ions. The F2-slice taken at the hydrogen-carbonate ions position at $\delta(^1\text{H}) = 14.2$ ppm in F1 is sufficiently spectrally separated from the water molecules position (*i.e.* $\delta(^1\text{H}) = 5.2$ ppm), and therefore reveals the ^{13}C chemical environments in the interfacial regions. This F2-slice exhibits the expected ^{13}C resonance of the interfacial carbonates (at $\delta(^{13}\text{C}) = 170.70$ ppm), as well as the ^{13}C resonance from the amide, carbonyl and carboxylate groups which belong to proteins (in the range of $\delta(^{13}\text{C}) = 172\text{-}180$ ppm). These results suggest a close spatial proximity between some proteins and the mineral phase in coral skeleton, and are consistent with the precipitation of aragonite by coral acid-rich proteins¹¹¹. Given the nature of the interactions involved in the CP magnetization transfer (*i.e.* heteronuclear $^1\text{H} - ^{13}\text{C}$ dipolar couplings), these proteins might be strongly bound to, and/or may even be trapped within the highly-disordered calcium carbonate environments in the interfacial regions. These features are totally consistent with a heterogeneous nucleation of the solid mineral phase driven by the skeletal proteins.

5.8 Precipitation pathway of coral aragonite

Given their undetermined age when observed in COCs from a broken surface, we explored the nature of the initial mineral deposits at the surface of the coral skeleton. In this direction, HIM observations were obtained from an intact corallite, on both the top of a growing columella and on the edge of a growing septum (Figure. 5.5). The highest magnification micrographs clearly demonstrate the presence of spherical nano-sized particles with a diameter of about 40-50 nm. Further, confocal Raman spectroscopy was applied, in which the laser was directed to the top of a growing columella from an intact skeletal branch. The band at 1087 cm^{-1} , ascribed to the (ν_1) symmetric stretching mode of the CO_2^{3-} units, is broader and is shifted towards lower wavenumbers than for well crystallized aragonite (obtained from the skeletal fibers exposed by CRM, see the white arrow in Figure. 5.2; A1). These features are typical of the presence of amorphous material, and were observed for the stable biogenic amorphous calcium carbonate (ACC) in sternal deposits of the crustacea *Porcellio scaber*¹⁵³. Solid-state NMR spectroscopy was also applied, in which the surface of a skeletal branch was first mechanically collected, and then this surface fraction and the underlying fraction of the skeletal branch (called here, the “core” fraction) were analyzed separately. Single pulse ^{13}C NMR spectra were recorded under quantitative conditions (*i.e.* $d_1 = 5000\text{ sec}$). The ^{13}C resonance from the surface fraction (FWHM = 1.45 ppm) is wider than the ^{13}C resonance from the core fraction (FWHM = 1.29 ppm).

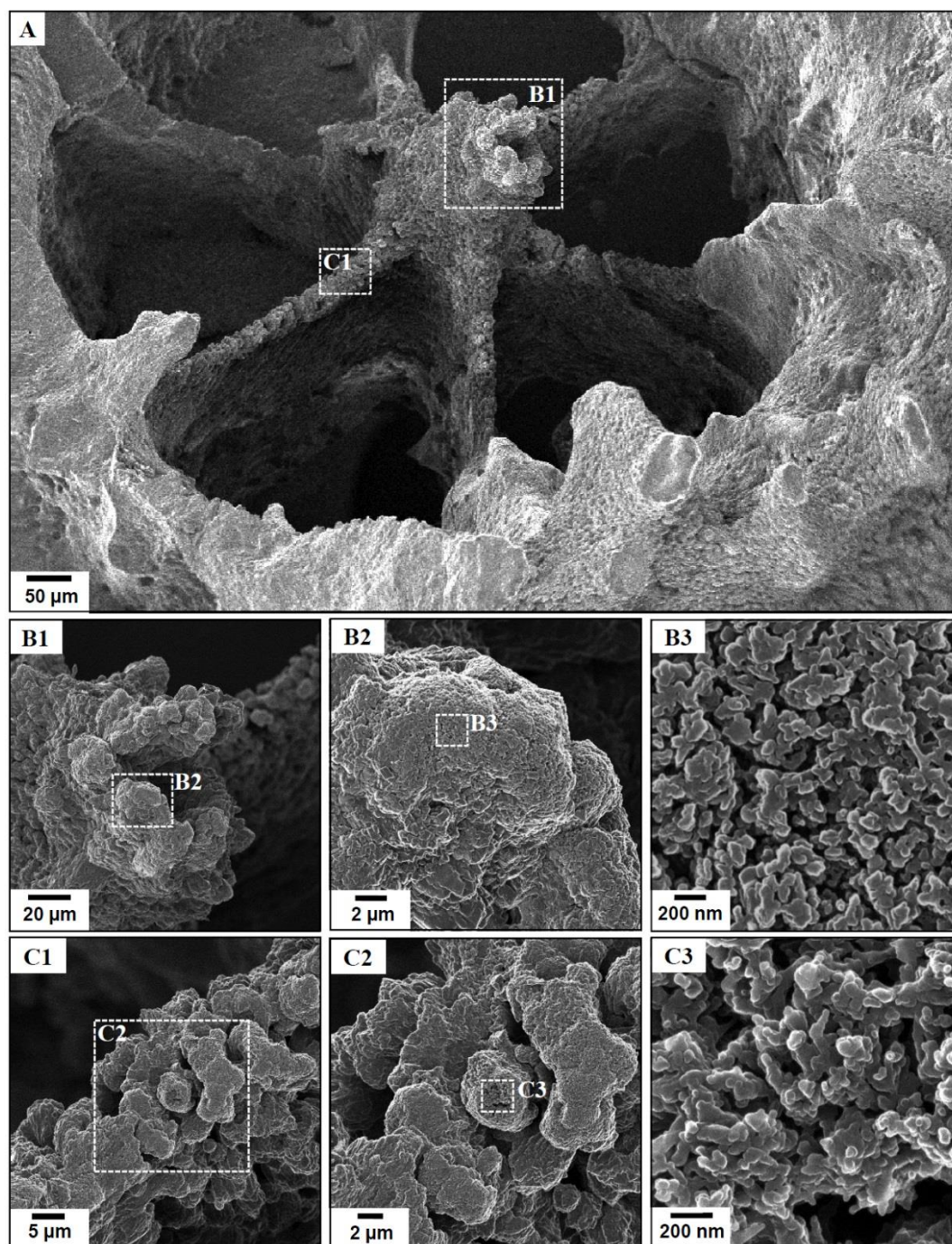


Figure 5.5 Observations of the initial mineral deposits in coral skeleton. HIM micrographs obtained on the surface of an intact skeletal branch. The region in (A) is a corallite, in which a growing columella and six growing septa are observable. (B1 to B3) and (C1 to C3) are successive magnifications that progressively reveal the morphology and size of the mineral particles at the top of the growing columella and on the edge of one of the growing septa, respectively.

This increase of the ^{13}C chemical shift distribution in the surface region is consistent with the presence of a small fraction of amorphous material. These interrelated investigations clearly demonstrate that ACC is a precursor phase for coral aragonite. Regarding the presence of “immature” aragonite particles in COCs revealed by Raman spectroscopy from cross-sections, it is now reasonable to assume that they correspond to ACC particles which are not fully converted into aragonite.

5.9 Transformation from ACC to aragonite

The transformation from ACC to aragonite was explored by analyzing COC regions by HIM (Figure 5.6). A COC and the adjoining skeletal fibers are clearly visible in Figure 5.6-A, in which the concentric layers (thickness, $\approx 7\ \mu\text{m}$, (Figure 5.7) correspond to the incremental growth lines of the mineral phase previously exposed by CRM. A higher resolution micrograph displays the orientations of the acicular aragonite crystals extended radially over 360° outward from the COC (Figure 5.5-B). In addition, very low angular distances between adjacent aragonite crystals, and a continuity between the successive layers (Figure 1-D), strongly suggest that the coral skeleton accretion operates *via* a spherulitic growth mechanism. Three successive images of increasing magnification, both in the COC (Figures 5.5; C1 to C3) and in the adjoining skeletal fibers (Figures 5.5; D1 to D3), make visible the chemical heterogeneity in the mineral phase previously highlighted by Raman spectroscopy. The COCs are filled up of randomly arranged, densely packed, spherical nano-sized particles with a diameter of about 40-50 nm (*i.e.* initially ACC nanoparticles); whereas the adjoining skeletal fibers are composed of micro-sized acicular aragonite crystals with homogeneous crystallographic orientations (Figures. 5.1-D & 5.7).

Further, the highest magnification micrograph reveals that the surface of the aragonite crystals is not smooth and exhibits the presence of spherical nanoparticles; and the latter have similar size

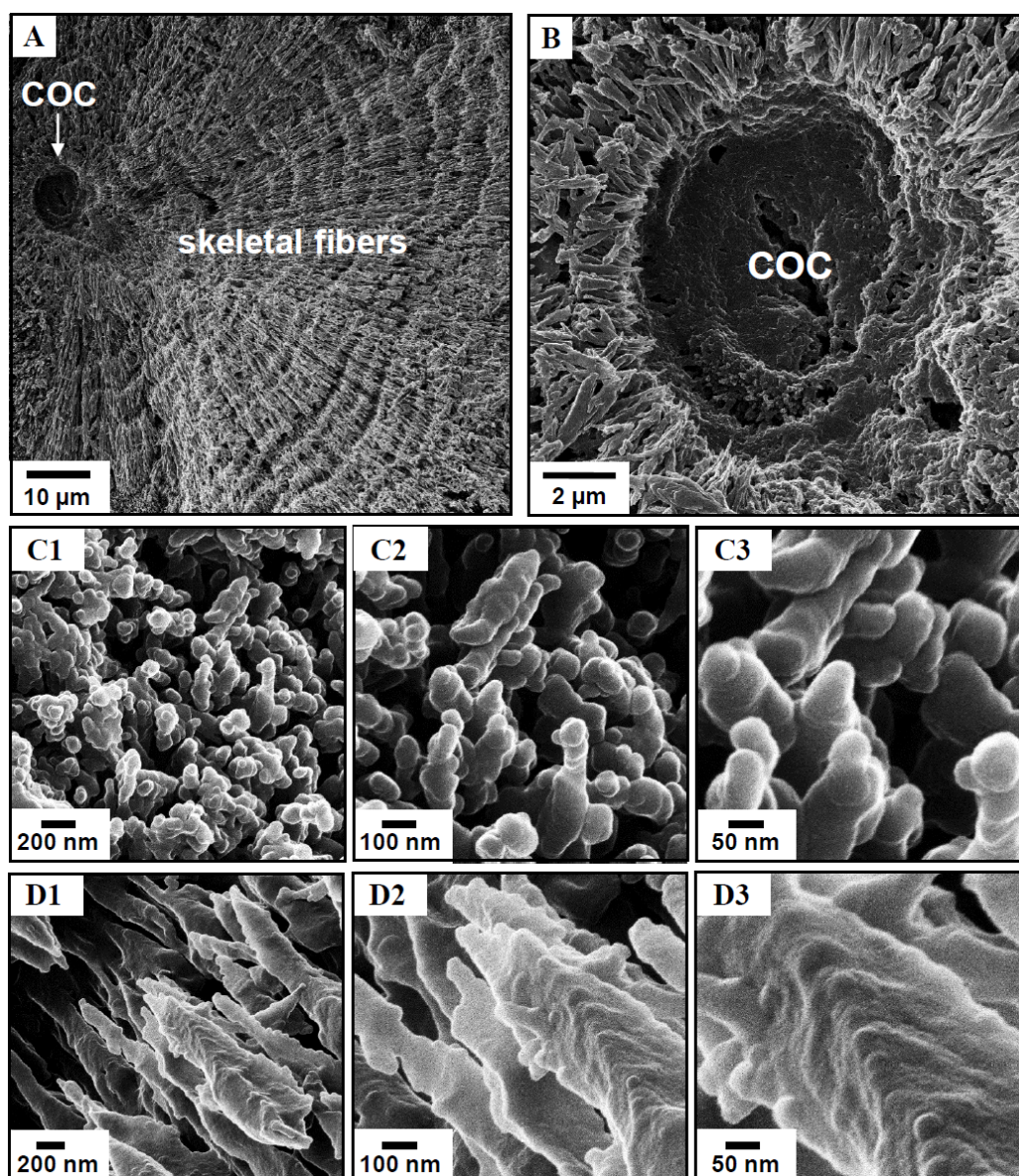


Figure 5.6 Ultra-high-resolution three-dimensional images of the trabecula units. (A, B, C1, C2, C3, D1, D2 and D3) HIM micrographs obtained from the broken, but not polished, surface of a skeletal branch. The region in (A) is a trabecula composed of skeletal fibers that radiate from the COC; while the region in (B) is a higher magnification of the COC observable in (A). (C1, C2 and C3) are successive magnifications of the mineral particles present in the COC observable in (A); while (D1, D2 and D3) are successive magnifications of the acicular aragonite crystals present in the skeletal fibers exposed in (A). These observations were made on the surface of a skeletal branch that was slightly etched in an aqueous solution of formic acid 1 % for 10 seconds.

with the nanoparticles observed in the COC. The edge of a COC, where the adjoining skeletal fibers start to form was closely examined (Figure. 5.8). This section reveals a clear spatio-temporal evolution of the mineral structure, showing initially deposited, ACC nanoparticles in the COC (top), nascent aragonite crystals in the middle, and more “mature”, acicular aragonite crystals on the bottom. Further, transmission electron microscopy (TEM) images confirm that the aragonite crystals have an irregular surface, and the selected area electron diffraction (SAED) patterns clearly show that they are polycrystalline (Figure 5.10). All these information indicate that ACC nanoparticles are initially deposited in the COCs; they further aggregate and serve as building blocks for constructing aragonite crystal structures. These observations provide clear evidence that coral aragonite crystals grow by aggregation of amorphous nanoparticles.

5.10 Chemical composition of the initial mineral deposits

Cathodoluminescence microscopy (CLM), backscattered electron (BSE) imaging and wavelength dispersive X-ray spectroscopy (WDS) mapping were coupled in an electron microprobe (Figure 5.8). CLM reveals the localization of the COCs, and enables WDS maps to show variations in the chemical composition across the trabeculae (COC vs. skeletal fibers). The dashed-line rectangles illustrate the region formerly investigated by CRM in which an elongated COC was clearly evidenced in the upper-left side (Figure. 5.2-A). The elongated white regions of the CLM image thus correspond to COCs (Figure. 5.9-A); and the latter coincide with magnesium-rich regions according to the WDS map (Figure. 5.9-B). Further, a HIM micrograph confirms the presence of spherical nanoparticles in a COC exposed both by CLM and

CRM (Figure. 5.9-C). These observations and measurements indicate that the initial mineral deposits consist of magnesium-rich ACC (Mg-ACC) nanoparticles. This confirms former observations in corals¹⁵⁴⁻¹⁵⁵ and supports the hypothesis that Mg stabilizes ACC¹⁵⁶⁻¹⁵⁷.

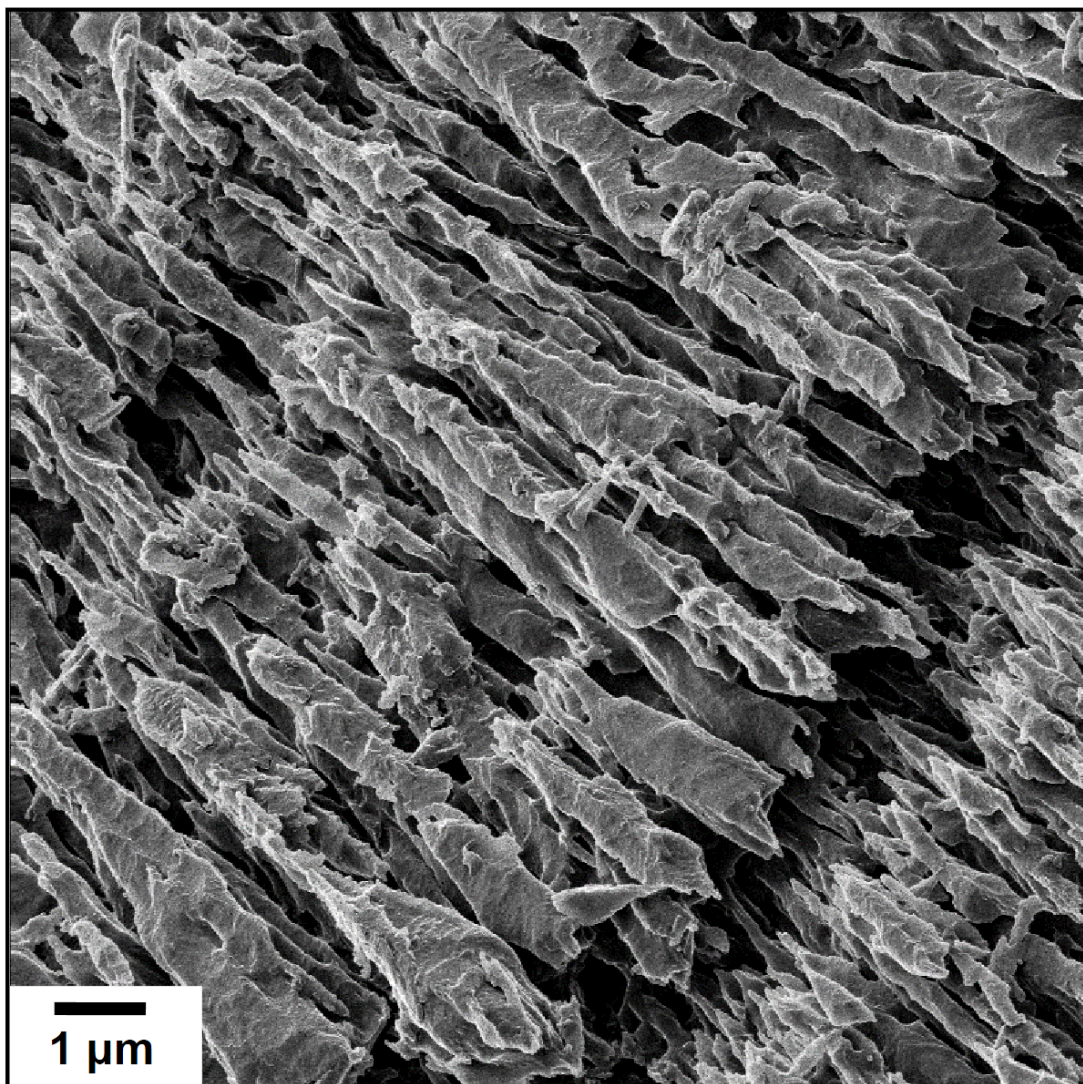


Figure 5.7 Observation of an incremental growth line of the mineral phase. HIM micrograph of highly ordered, acicular aragonite crystals that form skeletal fibers. These observations were made on the surface of a skeletal branch that was slightly etched in an aqueous solution of formic acid 1 % for 10 seconds.

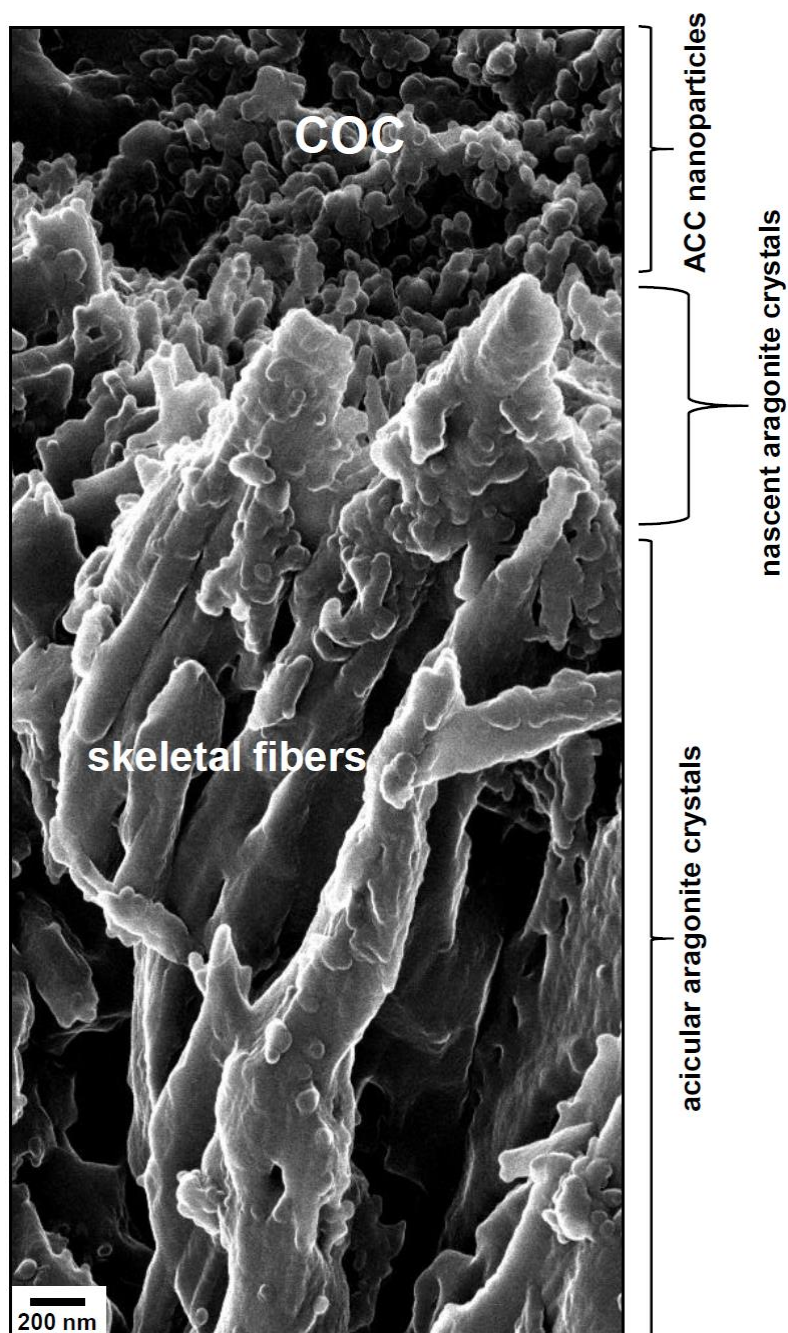


Figure 5.8 Ultra-high-resolution three-dimensional images of the crystal growth process. HIM micrograph from a restricted area of a trabecula composed of skeletal fibers (bottom region) that arise from the COC (top region). These observations were obtained from the broken, but not polished, surface of a skeletal branch. The latter was transversely sectioned (*i.e.* parallel to the vertical axes of the calices), and then slightly etched in an aqueous solution of formic acid 1 % for 10 seconds

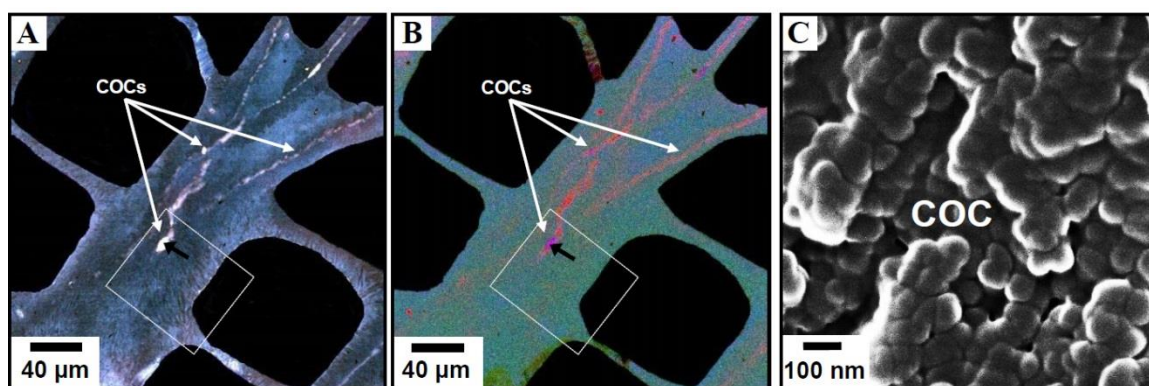


Figure 5.9 Variations in the chemical composition across the trabeculae. (A) Microphotograph of a coral skeleton region under CLM (blue, wavelength = 371-445 nm). (B) BGR (Blue-Green-Red) composite maps obtained from the same region imaged in (A). Blue = BSE image; Green = Calcium K α X-ray map; Red = Mg K α X-ray maps. (C) HIM micrograph from a COC exposed in (A) and (B), see the black arrows. The dashed-line rectangles in (A) and (B) illustrate the region formerly investigated by CRM (see Fig. A1, A2 & A3). These observations and measurements were obtained from a polished cross section of coral skeleton. The latter was prepared from a skeletal branch that was longitudinally sectioned (*i.e.* perpendicular to the vertical axes of the calices).

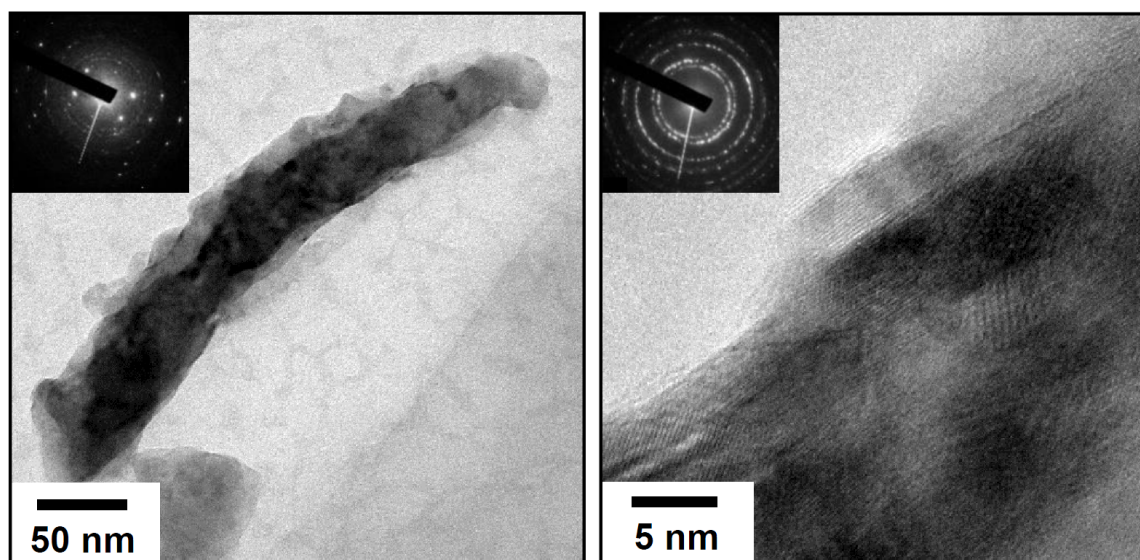


Figure 5.10 High-resolution observations of a coral aragonite crystal. Bright field TEM micrographs and corresponding SAED patterns of a coral aragonite crystal.

5.11 Conclusions

Our results provide the basic steps in the crystallization pathway of aragonite in a stony coral (Figure. 5.11). The process is initiated at the centers of calcification by the secretion of an organic matrix by the animal, leading to the formation of magnesium-rich amorphous calcium carbonate (Mg-ACC) nanoparticles. Our results strongly suggest that proteins are bound to, and/or trapped within the highly-disordered calcium carbonate environments in the interfacial regions. Our solid-state nuclear magnetic resonance data further suggest that the nucleation process is almost certainly catalyzed by coral acid rich proteins¹²⁰, which are present in the centers of calcification¹⁵⁸, and can precipitate aragonite directly from sea water¹¹¹. As more and more Mg-ACC particles are formed, they migrate from the center of calcification, lose Mg, and grow to become acicular aragonite crystals by aggregation of amorphous nanoparticles. These acicular crystals are highly ordered and aligned perpendicular to the axis of the center of calcification. Our observations strongly suggest the presence of a solid organic substrate, in the form of fibers, upon which a heterogeneous nucleation of the solid mineral phase occurs. In the working model presented in Figure. 5.11, we therefore considered an extracellular precipitation of the mineral phase. We hypothesize that the other option, an intracellular precipitation of the mineral phase¹⁵⁹⁻¹⁶⁰, would release the mineral and its associated skeletal organic material uniformly across the skeleton. This scenario is inconsistent with the “two-step model”¹⁰⁴ and the “layered model”¹³⁶ of skeletal growth in which “the entire septal skeleton is composed of superimposed layers of mineral and organic-enriched phases”¹³⁶. We propose that the organic-enriched phases, reported as “concentric organic-rich layers around the centers of calcification” in the present study, are traces of the organic substrate upon which the Mg-ACC particles have initially nucleated that are drained into the incremental growth lines within the skeletal fibers during skeletogenesis.

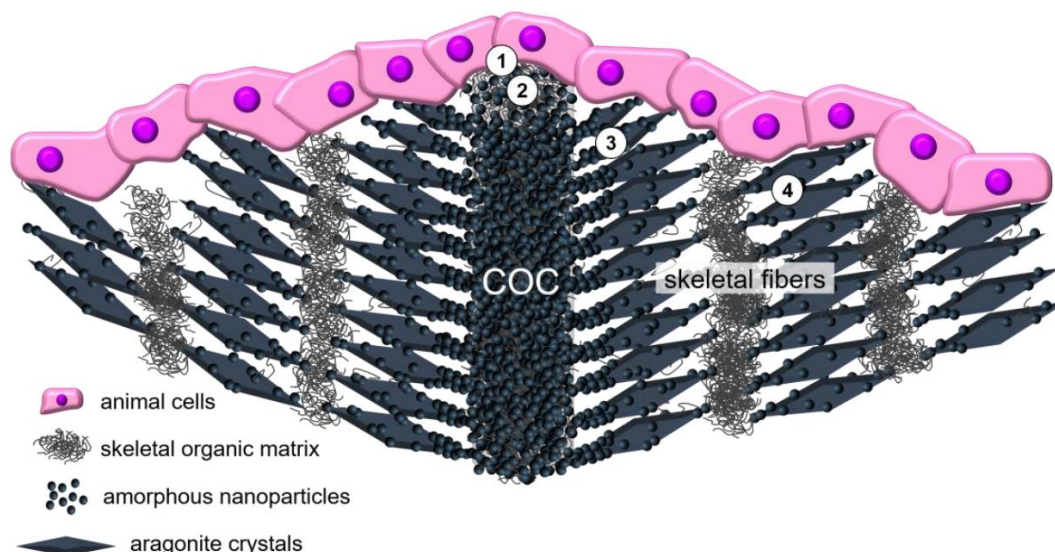


Figure 5.11 A working model, based on our experimental results, for biomineralization in stony corals. (1) Secretion of the SOM by the animal cells at the calcification site beneath the aboral tissue of the polyps, *i.e.* at the calcifying interface between the calcicoblastic ectodermal cells and the skeleton. (2) Precipitation of Mg-ACC nanoparticles mediated by the SOM. (1) and (2) steps might happen simultaneously. (3) Growth of acicular aragonite crystals by aggregation of amorphous nanoparticles. (4) Formation of the skeletal fibers *via* the “layered model” (40) of skeletal growth.

Finally, our results strongly suggest that the ability of corals to calcify is biologically controlled and relatively robust. As such, the biological reaction is far from thermodynamic equilibrium and the hence biomineralization in stony corals is not simply related to the equilibrium saturation state of carbonate ions, nor is it simply related to bulk pH of seawater¹⁶¹. This conclusion is further supported by the fossil record of scleractinian corals. These organisms survived the Paleocene-Eocene thermal maximum, which was associated with a very large increase in atmospheric CO₂¹⁶². Indeed, scleractinian corals radiated in the Eocene¹⁶³. While corals undoubtedly will be endangered in coming decades and centuries by thermal stress and eutrophication^{161, 164}, the results presented here and elsewhere¹¹¹ suggest that their ability to form aragonite structures will largely be uncompromised.

Citations

1. Spaldin, N. A., Fundamental Materials Research and the Course of Human Civilization. *cond-mat.mtrl-sci*.
2. Laboratory, N. R. e., Best Research Cell Efficiencies. **2017**.
3. Torrecillas, R.; Moya, J. S.; Diaz, L. A.; Bartolome, J. F.; Fernandez, A.; Lopez-Esteban, S., Nanotechnology in joint replacement. *Wiley interdisciplinary reviews. Nanomedicine and nanobiotechnology* **2009**, *1* (5), 540-52.
4. Park, J.; Kim, J.; Kim, S.-Y.; Cheong, W. H.; Jang, J.; Park, Y.-G.; Na, K.; Kim, Y.-T.; Heo, J. H.; Lee, C. Y.; Lee, J. H.; Bien, F.; Park, J.-U., Soft, smart contact lenses with integrations of wireless circuits, glucose sensors, and displays. *Science Advances* **2018**, *4* (1).
5. Moore, G. E., Cramming more components onto integrated circuits, Reprinted from Electronics, volume 38, number 8, April 19, 1965, pp.114 ff. *IEEE Solid-State Circuits Society Newsletter* **2006**, *11* (3), 33-35.
6. *Helium Ion Microscopy*. Springer International Publishing: 2016.
7. Everhart, T. E.; Thornley, R. F. M., Wide-band detector for micro-microampere low-energy electron currents. *Journal of Scientific Instruments* **1960**, *37* (7), 246.
8. Szeto, H. H.; Liu, S.; Soong, Y.; Seshan, S. V.; Cohen-Gould, L.; Manichev, V.; Feldman, L. C.; Gustafsson, T., Mitochondria Protection after Acute Ischemia Prevents Prolonged Upregulation of IL-1 β and IL-18 and Arrests CKD. *Journal of the American Society of Nephrology* **2017**, *28* (5), 1437-1449.
9. Von Euw, S.; Zhang, Q.; Manichev, V.; Murali, N.; Gross, J.; Feldman, L. C.; Gustafsson, T.; Flach, C.; Mendelsohn, R.; Falkowski, P. G., Biological control of aragonite formation in stony corals. *Science* **2017**, *356* (6341), 933-938.
10. Sina, M.; Alvarado, J.; Shobukawa, H.; Alexander, C.; Manichev, V.; Feldman, L.; Gustafsson, T.; Stevenson, K. J.; Meng, Y. S., Direct Visualization of the Solid Electrolyte Interphase and Its Effects on Silicon Electrochemical Performance. *Advanced Materials Interfaces* **2016**, *3* (20), 1600438-n/a.
11. Livengood, R.; Tan, S.; Greenzweig, Y.; Notte, J.; McVey, S., Subsurface damage from helium ions as a function of dose, beam energy, and dose rate. *Journal of Vacuum Science & Technology B: Microelectronics and Nanometer Structures Processing, Measurement, and Phenomena* **2009**, *27* (6), 3244-3249.
12. Luo, F.; Manichev, V.; Li, M.; Mitchson, G.; Yakshinskiy, B.; Gustafsson, T.; Johnson, D.; Garfunkel, E. In *Helium ion beam lithography (HIBL) using HafSOx as the resist*, SPIE Advanced Lithography, SPIE: 2016; p 9.
13. Cybart, S. A.; Cho, E. Y.; Wong, T. J.; Wehlin, B. H.; Ma, M. K.; Huynh, C.; Dynes, R. C., Nano Josephson superconducting tunnel junctions in YBa₂Cu₃O_{7- δ} directly patterned with a focused helium ion beam. *Nature Nanotechnology* **2015**, *10*, 598.
14. Melli, M.; Polyakov, A.; Gargas, D.; Huynh, C.; Scipioni, L.; Bao, W.; Ogletree, D. F.; Schuck, P. J.; Cabrini, S.; Weber-Bargioni, A., Reaching the Theoretical Resonance Quality Factor Limit in Coaxial Plasmonic Nanoresonators Fabricated by Helium Ion Lithography. *Nano Letters* **2013**, *13* (6), 2687-2691.
15. Sidorkin, V.; Veldhoven, E. v.; Drift, E. v. d.; Alkemade, P.; Salemink, H.; Maas, D., Sub-10-nm nanolithography with a scanning helium beam. *Journal of Vacuum Science & Technology*

B: Microelectronics and Nanometer Structures Processing, Measurement, and Phenomena **2009**, 27 (4), L18-L20.

16. Li, M.; Manichev, V.; Yu, F.; Hutchison, D.; Nyman, M.; Gustafsson, T.; Feldman, L. C.; Garfunkel, E. L. In *Novel Sn-based photoresist for high aspect ratio patterning*, SPIE Advanced Lithography, SPIE: 2018; p 8.
17. Heckman, C.; Kanagasundaram, S.; Cayer, M.; Paige, J., Preparation of cultured cells for scanning electron microscope. **2007**.
18. Yin, S., In Coral Skeletons, Microscopic Portraits of Resilience? *New York Times* **2017**.
19. 2017, J. June's sharpest science shots, selected by Nature's photo team.
<https://www.nature.com/news/party-slugs-pseudo-saturn-and-a-dancing-moon-rover-1.22236>.
20. Watt, F.; Osipowicz, T.; Choo, T. F.; Orlic, I.; Tang, S. M., Nuclear microprobe analysis and imaging: Current state of the art performances. *Nuclear Instruments and Methods in Physics Research Section B: Beam Interactions with Materials and Atoms* **1998**, 136-138, 313-317.
21. Banford, A. P., The transport of charged particle beams. **1966**.
22. Bell, D. C.; Lemme, M. C.; Stern, L. A.; Williams, J. R.; Marcus, C. M., Precision cutting and patterning of graphene with helium ions. *Nanotechnology* **2009**, 20 (45), 455301.
23. Petrov, Y. V.; Vyvenko, O. F.; Bondarenko, A. S., Scanning helium ion microscope: Distribution of secondary electrons and ion channeling. *Journal of Surface Investigation. X-ray, Synchrotron and Neutron Techniques* **2010**, 4 (5), 792-795.
24. ESTAR. <https://physics.nist.gov/PhysRefData/Star/Text/ESTAR.html>.
25. Joy, D. C., *Helium Ion Microscopy*. Springer-Verlag New York: 2013.
26. Lin, Y.; Joy, D. C., A new examination of secondary electron yield data. *Surface and Interface Analysis* **2005**, 37 (11), 895-900.
27. High Resolution Chemical Imaging on the Helium Ion Microscope. In *European Microscopy Congress 2016: Proceedings*.
28. Dowsett, D.; Audinot, J.-N.; Vollnhals, F.; Eswara, S.; Wirtz, T., High Resolution Chemical Imaging on the Helium Ion Microscope. In *European Microscopy Congress 2016: Proceedings*, Wiley-VCH Verlag GmbH & Co. KGaA: 2016.
29. Klingner, N.; Heller, R.; Hlawacek, G.; Borany, J. v.; Notte, J.; Huang, J.; Facsko, S., Nanometer scale elemental analysis in the helium ion microscope using time of flight spectrometry. *Ultramicroscopy* **2016**, 162, 91-97.
30. Ortec, Totally Depleted Silicon Surface Barrier Radiation Detector <http://www.ortec-online.com/products/radiation-detectors/silicon-charged-particle-radiation-detectors/si-charged-particle-radiation-detectors-for-research-applications/b-series>.
31. Rogers, A. M.; Sanetullaev, A.; Lynch, W. G.; Tsang, M. B.; Lee, J.; Bazin, D.; Coupland, D.; Henzl, V.; Henzlova, D.; Kilburn, M.; Wallace, M. S.; Youngs, M.; Delaunay, F.; Famiano, M.; Shapira, D.; Jones, K. L.; Schmitt, K. T.; Sun, Z. Y., Tracking rare-isotope beams with microchannel plates. *Nuclear Instruments and Methods in Physics Research Section A: Accelerators, Spectrometers, Detectors and Associated Equipment* **2015**, 795, 325-334.
32. Focused Ion Beam Sputtering Yield Calculator.
<https://www.asu.edu/clas/csss/NUE/FIBSputterCalcYamamura.html>.
33. Coca, S. G.; Singanamala, S.; Parikh, C. R., Chronic kidney disease after acute kidney injury: a systematic review and meta-analysis. *Kidney international* **2012**, 81 (5), 442-8.
34. Kaushal, G. P.; Shah, S. V., Challenges and advances in the treatment of AKI. *Journal of the American Society of Nephrology : JASN* **2014**, 25 (5), 877-83.
35. Gobe, G. C.; Bennett, N. C.; West, M.; Colditz, P.; Brown, L.; Vesey, D. A.; Johnson, D. W., Increased progression to kidney fibrosis after erythropoietin is used as a treatment for acute kidney injury. *American Journal of Physiology-Renal Physiology* **2014**, 306 (6), F681-F692.

36. Dagher, P. C.; Mai, E. M.; Hato, T.; Lee, S. Y.; Anderson, M. D.; Karozos, S. C.; Mang, H. E.; Knipe, N. L.; Plotkin, Z.; Sutton, T. A., The p53 inhibitor pifithrin- α can stimulate fibrosis in a rat model of ischemic acute kidney injury. *American journal of physiology. Renal physiology* **2012**, 302 (2), F284-91.
37. Haase, V. H., Hypoxia-inducible factor signaling in the development of kidney fibrosis. *Fibrogenesis & tissue repair* **2012**, 5 (Suppl 1), S16.
38. Kelsen, S.; He, X.; Chade, A. R., Early superoxide scavenging accelerates renal microvascular rarefaction and damage in the stenotic kidney. *American journal of physiology. Renal physiology* **2012**, 303 (4), F576-83.
39. Kohan, D. E.; Barton, M., Endothelin and Endothelin Antagonists in Chronic Kidney Disease. *Kidney international* **2014**, 86 (5), 896-904.
40. Basile, D. P.; Bonventre, J. V.; Mehta, R.; Nangaku, M.; Unwin, R.; Rosner, M. H.; Kellum, J. A.; Ronco, C., Progression after AKI: Understanding Maladaptive Repair Processes to Predict and Identify Therapeutic Treatments. *Journal of the American Society of Nephrology : JASN* **2016**, 27 (3), 687-97.
41. Hill, N. R.; Fatoba, S. T.; Oke, J. L.; Hirst, J. A.; O'Callaghan, C. A.; Lasserson, D. S.; Hobbs, F. D. R., Global Prevalence of Chronic Kidney Disease – A Systematic Review and Meta-Analysis. *PLOS ONE* **2016**, 11 (7), e0158765.
42. Varga, J.; Pasche, B., Transforming growth factor beta as a therapeutic target in systemic sclerosis. *Nature reviews. Rheumatology* **2009**, 5 (4), 200-6.
43. Goncalves, G. M.; Castoldi, A.; Braga, T. T.; Camara, N. O., New roles for innate immune response in acute and chronic kidney injuries. *Scandinavian journal of immunology* **2011**, 73 (5), 428-35.
44. Anders, H. J.; Schaefer, L., Beyond tissue injury-damage-associated molecular patterns, toll-like receptors, and inflammasomes also drive regeneration and fibrosis. *Journal of the American Society of Nephrology : JASN* **2014**, 25 (7), 1387-400.
45. Iyer, S. S.; Pulskens, W. P.; Sadler, J. J.; Butter, L. M.; Teske, G. J.; Ulland, T. K.; Eisenbarth, S. C.; Florquin, S.; Flavell, R. A.; Leemans, J. C.; Sutterwala, F. S., Necrotic cells trigger a sterile inflammatory response through the Nlrp3 inflammasome. *Proceedings of the National Academy of Sciences of the United States of America* **2009**, 106 (48), 20388-20393.
46. Vilaysane, A.; Chun, J.; Seamone, M. E.; Wang, W.; Chin, R.; Hirota, S.; Li, Y.; Clark, S. A.; Tschopp, J.; Trpkov, K.; Hemmelgarn, B. R.; Beck, P. L.; Muruve, D. A., The NLRP3 inflammasome promotes renal inflammation and contributes to CKD. *Journal of the American Society of Nephrology : JASN* **2010**, 21 (10), 1732-44.
47. Kurts, C.; Panzer, U.; Anders, H.-J.; Rees, A. J., The immune system and kidney disease: basic concepts and clinical implications. *Nature Reviews Immunology* **2013**, 13, 738.
48. Turner, C. M.; Arulkumaran, N.; Singer, M.; Unwin, R. J.; Tam, F. W., Is the inflammasome a potential therapeutic target in renal disease? *BMC nephrology* **2014**, 15, 21.
49. Tschopp, J.; Schroder, K., NLRP3 inflammasome activation: The convergence of multiple signalling pathways on ROS production? *Nature reviews. Immunology* **2010**, 10 (3), 210-5.
50. van Bruggen, R.; Koker, M. Y.; Jansen, M.; van Houdt, M.; Roos, D.; Kuijpers, T. W.; van den Berg, T. K., Human NLRP3 inflammasome activation is Nox1-4 independent. *Blood* **2010**, 115 (26), 5398-400.
51. Zhou, R.; Yazdi, A. S.; Menu, P.; Tschopp, J., A role for mitochondria in NLRP3 inflammasome activation. *Nature* **2011**, 469 (7329), 221-5.
52. West, A. P.; Shadel, G. S.; Ghosh, S., Mitochondria in innate immune responses. *Nature reviews. Immunology* **2011**, 11 (6), 389-402.

53. Jabaut, J.; Ather, J. L.; Taracanova, A.; Poynter, M. E.; Ckless, K., Mitochondria-targeted drugs enhance Nlrp3 inflammasome-dependent IL-1 β secretion in association with alterations in cellular redox and energy status. *Free radical biology & medicine* **2013**, *60*, 233-45.
54. Heid, M. E.; Keyel, P. A.; Kamga, C.; Shiva, S.; Watkins, S. C.; Salter, R. D., Mitochondrial reactive oxygen species induces NLRP3-dependent lysosomal damage and inflammasome activation. *Journal of immunology (Baltimore, Md. : 1950)* **2013**, *191* (10), 5230-8.
55. Nakahira, K.; Haspel, J. A.; Rathinam, V. A.; Lee, S. J.; Dolinay, T.; Lam, H. C.; Englert, J. A.; Rabinovitch, M.; Cernadas, M.; Kim, H. P.; Fitzgerald, K. A.; Ryter, S. W.; Choi, A. M., Autophagy proteins regulate innate immune responses by inhibiting the release of mitochondrial DNA mediated by the NALP3 inflammasome. *Nature immunology* **2011**, *12* (3), 222-30.
56. Iyer, S. S.; He, Q.; Janczy, J. R.; Elliott, E. I.; Zhong, Z.; Olivier, A. K.; Sadler, J. J.; Knepper-Adrian, V.; Han, R.; Qiao, L.; Eisenbarth, S. C.; Nauseef, W. M.; Cassel, S. L.; Sutterwala, F. S., Mitochondrial cardiolipin is required for Nlrp3 inflammasome activation. *Immunity* **2013**, *39* (2), 311-323.
57. Szeto, H. H.; Liu, S.; Soong, Y.; Wu, D.; Darrah, S. F.; Cheng, F. Y.; Zhao, Z.; Ganger, M.; Tow, C. Y.; Seshan, S. V., Mitochondria-targeted peptide accelerates ATP recovery and reduces ischemic kidney injury. *Journal of the American Society of Nephrology : JASN* **2011**, *22* (6), 1041-52.
58. Birk, A. V.; Liu, S.; Soong, Y.; Mills, W.; Singh, P.; Warren, J. D.; Seshan, S. V.; Pardee, J. D.; Szeto, H. H., The mitochondrial-targeted compound SS-31 re-energizes ischemic mitochondria by interacting with cardiolipin. *Journal of the American Society of Nephrology : JASN* **2013**, *24* (8), 1250-61.
59. Szeto, H. H.; Liu, S.; Soong, Y.; Birk, A. V., Improving mitochondrial bioenergetics under ischemic conditions increases warm ischemia tolerance in the kidney. *American journal of physiology. Renal physiology* **2015**, *308* (1), F11-21.
60. Zhao, K.; Zhao, G. M.; Wu, D.; Soong, Y.; Birk, A. V.; Schiller, P. W.; Szeto, H. H., Cell-permeable peptide antioxidants targeted to inner mitochondrial membrane inhibit mitochondrial swelling, oxidative cell death, and reperfusion injury. *The Journal of biological chemistry* **2004**, *279* (33), 34682-90.
61. Liu, S.; Soong, Y.; Seshan, S. V.; Szeto, H. H., Novel cardiolipin therapeutic protects endothelial mitochondria during renal ischemia and mitigates microvascular rarefaction, inflammation, and fibrosis. *American journal of physiology. Renal physiology* **2014**, *306* (9), F970-80.
62. Sutton, T. A.; Fisher, C. J.; Molitoris, B. A., Microvascular endothelial injury and dysfunction during ischemic acute renal failure. *Kidney international* **2002**, *62* (5), 1539-49.
63. Basile, D. P.; Donohoe, D.; Roethe, K.; Osborn, J. L., Renal ischemic injury results in permanent damage to peritubular capillaries and influences long-term function. *American journal of physiology. Renal physiology* **2001**, *281* (5), F887-99.
64. Pusztaszeri, M. P.; Seelentag, W.; Bosman, F. T., Immunohistochemical expression of endothelial markers CD31, CD34, von Willebrand factor, and Fli-1 in normal human tissues. *The journal of histochemistry and cytochemistry : official journal of the Histochemistry Society* **2006**, *54* (4), 385-95.
65. Nakayama, T.; Sato, W.; Yoshimura, A.; Zhang, L.; Kosugi, T.; Campbell-Thompson, M.; Kojima, H.; Croker, B. P.; Nakagawa, T., Endothelial von Willebrand factor release due to eNOS deficiency predisposes to thrombotic microangiopathy in mouse aging kidney. *The American journal of pathology* **2010**, *176* (5), 2198-208.
66. Ward, B. W.; Notte, J. A.; Economou, N. P., Helium ion microscope: A new tool for nanoscale microscopy and metrology. *Journal of Vacuum Science & Technology B:*

Microelectronics and Nanometer Structures Processing, Measurement, and Phenomena **2006**, 24 (6), 2871-2874.

67. Rice, W. L.; Van Hoek, A. N.; Păunescu, T. G.; Huynh, C.; Goetze, B.; Singh, B.; Scipioni, L.; Stern, L. A.; Brown, D., High Resolution Helium Ion Scanning Microscopy of the Rat Kidney. *PLOS ONE* **2013**, 8 (3), e57051.

68. Pavenstadt, H.; Kriz, W.; Kretzler, M., Cell biology of the glomerular podocyte. *Physiological reviews* **2003**, 83 (1), 253-307.

69. Wagner, M. C.; Rhodes, G.; Wang, E.; Pruthi, V.; Arif, E.; Saleem, M. A.; Wean, S. E.; Garg, P.; Verma, R.; Holzman, L. B.; Gattone, V.; Molitoris, B. A.; Nihalani, D., Ischemic Injury to Kidney Induces Glomerular Podocyte Effacement and Dissociation of Slit Diaphragm Proteins Neph1 and ZO-1. *Journal of Biological Chemistry* **2008**, 283 (51), 35579-35589.

70. Abe, Y.; Sakairi, T.; Kajiyama, H.; Shrivastav, S.; Beeson, C.; Kopp, J. B., Bioenergetic characterization of mouse podocytes. *American journal of physiology. Cell physiology* **2010**, 299 (2), C464-76.

71. Imasawa, T.; Rossignol, R., Podocyte energy metabolism and glomerular diseases. *The international journal of biochemistry & cell biology* **2013**, 45 (9), 2109-18.

72. Cybulsky, A. V., The intersecting roles of endoplasmic reticulum stress, ubiquitin-proteasome system, and autophagy in the pathogenesis of proteinuric kidney disease. *Kidney international* **2013**, 84 (1), 25-33.

73. Hartleben, B.; Godel, M.; Meyer-Schwesinger, C.; Liu, S.; Ulrich, T.; Kobler, S.; Wiech, T.; Grammer, F.; Arnold, S. J.; Lindenmeyer, M. T.; Cohen, C. D.; Pavenstadt, H.; Kerjaschki, D.; Mizushima, N.; Shaw, A. S.; Walz, G.; Huber, T. B., Autophagy influences glomerular disease susceptibility and maintains podocyte homeostasis in aging mice. *The Journal of clinical investigation* **2010**, 120 (4), 1084-96.

74. Marchi, S.; Patergnani, S.; Pinton, P., The endoplasmic reticulum-mitochondria connection: one touch, multiple functions. *Biochimica et biophysica acta* **2014**, 1837 (4), 461-9.

75. Barrera-Chimal, J.; Perez-Villalva, R.; Ortega, J. A.; Sanchez, A.; Rodriguez-Romo, R.; Durand, M.; Jaisser, F.; Bobadilla, N. A., Mild ischemic injury leads to long-term alterations in the kidney: amelioration by spironolactone administration. *International journal of biological sciences* **2015**, 11 (8), 892-900.

76. Janmey, P. A.; Hvidt, S.; Oster, G. F.; Lamb, J.; Stossel, T. P.; Hartwig, J. H., Effect of ATP on actin filament stiffness. *Nature* **1990**, 347, 95.

77. Koppen, M.; Langer, T., Protein degradation within mitochondria: versatile activities of AAA proteases and other peptidases. *Critical reviews in biochemistry and molecular biology* **2007**, 42 (3), 221-42.

78. Langer, T.; Kaser, M.; Klanner, C.; Leonhard, K., AAA proteases of mitochondria: quality control of membrane proteins and regulatory functions during mitochondrial biogenesis. *Biochemical Society transactions* **2001**, 29 (Pt 4), 431-6.

79. Birk, A. V.; Chao, W. M.; Bracken, C.; Warren, J. D.; Szeto, H. H., Targeting mitochondrial cardiolipin and the cytochrome c/cardiolipin complex to promote electron transport and optimize mitochondrial ATP synthesis. *Br J Pharmacol* **2014**, 171 (8), 2017-28.

80. Szeto, H. H.; Birk, A. V., Serendipity and the discovery of novel compounds that restore mitochondrial plasticity. *Clinical pharmacology and therapeutics* **2014**, 96 (6), 672-83.

81. Birk, A. V.; Chao, W. M.; Liu, S.; Soong, Y.; Szeto, H. H., Disruption of cytochrome c heme coordination is responsible for mitochondrial injury during ischemia. *Biochimica et biophysica acta* **2015**, 1847 (10), 1075-84.

82. Shi, J.; Dai, W.; Hale, S. L.; Brown, D. A.; Wang, M.; Han, X.; Kloner, R. A., Bendavia restores mitochondrial energy metabolism gene expression and suppresses cardiac fibrosis in the border zone of the infarcted heart. *Life sciences* **2015**, *141*, 170-8.
83. Sabbah, H. N.; Gupta, R. C.; Kohli, S.; Wang, M.; Hachem, S.; Zhang, K., Chronic Therapy With Elamipretide (MTP-131), a Novel Mitochondria-Targeting Peptide, Improves Left Ventricular and Mitochondrial Function in Dogs With Advanced Heart Failure. *Circulation. Heart failure* **2016**, *9* (2), e002206.
84. Eirin, A.; Ebrahimi, B.; Kwon, S. H.; Fiala, J. A.; Williams, B. J.; Woollard, J. R.; He, Q.; Gupta, R. C.; Sabbah, H. N.; Prakash, Y. S.; Textor, S. C.; Lerman, A.; Lerman, L. O., Restoration of Mitochondrial Cardiolipin Attenuates Cardiac Damage in Swine Renovascular Hypertension. *Journal of the American Heart Association* **2016**, *5* (6).
85. van Vliet, A. R.; Verfaillie, T.; Agostinis, P., New functions of mitochondria associated membranes in cellular signaling. *Biochimica et biophysica acta* **2014**, *1843* (10), 2253-62.
86. Bani-Hani, A. H.; Leslie, J. A.; Asanuma, H.; Dinarello, C. A.; Campbell, M. T.; Meldrum, D. R.; Zhang, H.; Hile, K.; Meldrum, K. K., IL-18 neutralization ameliorates obstruction-induced epithelial-mesenchymal transition and renal fibrosis. *Kidney international* **2009**, *76* (5), 500-11.
87. Mizuguchi, Y.; Chen, J.; Seshan, S. V.; Poppas, D. P.; Szeto, H. H.; Felsen, D., A novel cell-permeable antioxidant peptide decreases renal tubular apoptosis and damage in unilateral ureteral obstruction. *American journal of physiology. Renal physiology* **2008**, *295* (5), F1545-53.
88. Wu, J.; Li, H.; Sun, X.; Zhang, H.; Hao, S.; Ji, M.; Yang, J.; Li, K., A Mitochondrion-Targeted Antioxidant Ameliorates Isoflurane-Induced Cognitive Deficits in Aging Mice. *PLOS ONE* **2015**, *10* (9), e0138256.
89. Wu, J.; Yan, Z.; Schwartz, D. E.; Yu, J.; Malik, A. B.; Hu, G., Activation of NLRP3 inflammasome in alveolar macrophages contributes to mechanical stretch-induced lung inflammation and injury. *Journal of immunology (Baltimore, Md. : 1950)* **2013**, *190* (7), 3590-9.
90. Baldwin, A. G.; Brough, D.; Freeman, S., Inhibiting the Inflammasome: A Chemical Perspective. *Journal of Medicinal Chemistry* **2016**, *59* (5), 1691-1710.
91. Ozaki, E.; Campbell, M.; Doyle, S. L., Targeting the NLRP3 inflammasome in chronic inflammatory diseases: current perspectives. *Journal of inflammation research* **2015**, *8*, 15-27.
92. Duan, S. B.; Yang, S. K.; Zhou, Q. Y.; Pan, P.; Zhang, H.; Liu, F.; Xu, X. Q., Mitochondria-targeted peptides prevent on contrast-induced acute kidney injury in the rats with hypercholesterolemia. *Renal failure* **2013**, *35* (8), 1124-9.
93. Li, G.; Wu, J.; Li, R.; Yuan, D.; Fan, Y.; Yang, J.; Ji, M.; Zhu, S., Protective Effects of Antioxidant Peptide SS-31 Against Multiple Organ Dysfunctions During Endotoxemia. *Inflammation* **2016**, *39* (1), 54-64.
94. Hou, Y.; Li, S.; Wu, M.; Wei, J.; Ren, Y.; Du, C.; Wu, H.; Han, C.; Duan, H.; Shi, Y., Mitochondria-targeted peptide SS-31 attenuates renal injury via an antioxidant effect in diabetic nephropathy. *American journal of physiology. Renal physiology* **2016**, *310* (6), F547-59.
95. Szeto, H. H.; Liu, S.; Soong, Y.; Alam, N.; Prusky, G. T.; Seshan, S. V., Protection of mitochondria prevents high-fat diet-induced glomerulopathy and proximal tubular injury. *Kidney international* **2016**, *90* (5), 997-1011.
96. Eirin, A.; Ebrahimi, B.; Zhang, X.; Zhu, X. Y.; Woollard, J. R.; He, Q.; Textor, S. C.; Lerman, A.; Lerman, L. O., Mitochondrial protection restores renal function in swine atherosclerotic renovascular disease. *Cardiovascular research* **2014**, *103* (4), 461-72.
97. Allemand, D.; Tambutté, É.; Zoccola, D.; Tambutté, S., Coral Calcification, Cells to Reefs. In *Coral Reefs: An Ecosystem in Transition*, Dubinsky, Z.; Stambler, N., Eds. Springer Netherlands: Dordrecht, 2011; pp 119-150.

98. Allemand, D.; Ferrier-Pagès, C.; Furla, P.; Houlbrèque, F.; Puverel, S.; Reynaud, S.; Tambutté, É.; Tambutté, S.; Zoccola, D., Biomineralisation in reef-building corals: from molecular mechanisms to environmental control. *Comptes Rendus Palevol* **2004**, 3 (6), 453-467.
99. Geochemical Perspectives on Coral Mineralization. *Reviews in Mineralogy and Geochemistry* **2003**, 54 (1), 151-187.
100. Barnes, D. J., Coral skeletons: an explanation of their growth and structure. *Science (New York, N.Y.)* **1970**, 170 (3964), 1305-8.
101. Constantz, B. R., Coral Skeleton Construction: A Physiochemically Dominated Process. *PALAIOS* **1986**, 1 (2), 152-157.
102. Cuif, J.-P.; Bendounan, A.; Dauphin, Y.; Nouet, J.; Sirotti, F., Synchrotron-based photoelectron spectroscopy provides evidence for a molecular bond between calcium and mineralizing organic phases in invertebrate calcareous skeletons. *Analytical and Bioanalytical Chemistry* **2013**, 405 (27), 8739-8748.
103. Cuif, J. P.; Dauphin, Y., The Environment Recording Unit in coral skeletons – a synthesis of structural and chemical evidences for a biochemically driven, stepping-growth process in fibres. *Biogeosciences* **2005**, 2 (1), 61-73.
104. Cuif, J.-P.; Dauphin, Y., The two-step mode of growth in the scleractinian coral skeletons from the micrometre to the overall scale. *Journal of Structural Biology* **2005**, 150 (3), 319-331.
105. Falini, G.; Fermani, S.; Goffredo, S., Coral biomineralization: A focus on intra-skeletal organic matrix and calcification. *Seminars in cell & developmental biology* **2015**, 46, 17-26.
106. Johnston, I. S., The Ultrastructure of Skeletogenesis in Hermatypic Corals. In *International Review of Cytology*, Bourne, G. H.; Danielli, J. F., Eds. Academic Press: 1980; Vol. 67, pp 171-214.
107. Puverel, S.; Tambutté, E.; Zoccola, D.; Domart-Coulon, I.; Bouchot, A.; Lotto, S.; Allemand, D.; Tambutté, S., Antibodies against the organic matrix in scleractinians: a new tool to study coral biomineralization. *Coral Reefs* **2005**, 24 (1), 149-156.
108. Tambutté, S.; Tambutté, E.; Zoccola, D.; Allemand, D., Organic Matrix and Biomineralization of Scleractinian Corals. In *Handbook of Biomineralization*, Wiley-VCH Verlag GmbH: 2008; pp 243-259.
109. Clode, P. L.; Marshall, A. T., Low temperature FESEM of the calcifying interface of a scleractinian coral. *Tissue & cell* **2002**, 34 (3), 187-98.
110. Clode, P. L.; Marshall, A. T., Calcium associated with a fibrillar organic matrix in the scleractinian coral *Galaxea fascicularis*. *Protoplasma* **2003**, 220 (3-4), 153-61.
111. Mass, T.; Drake, J. L.; Haramaty, L.; Kim, J. D.; Zelzion, E.; Bhattacharya, D.; Falkowski, P. G., Cloning and characterization of four novel coral acid-rich proteins that precipitate carbonates in vitro. *Current biology : CB* **2013**, 23 (12), 1126-31.
112. Al-Horani, F. A.; Al-Moghrabi, S. M.; de Beer, D., The mechanism of calcification and its relation to photosynthesis and respiration in the scleractinian coral *Galaxea fascicularis*. *Marine Biology* **2003**, 142 (3), 419-426.
113. Allison, N.; Cohen, I.; Finch, A. A.; Erez, J.; Tudhope, A. W., Corals concentrate dissolved inorganic carbon to facilitate calcification. *Nature Communications* **2014**, 5, 5741.
114. Holcomb, M.; Venn, A. A.; Tambutté, E.; Tambutté, S.; Allemand, D.; Trotter, J.; McCulloch, M., Coral calcifying fluid pH dictates response to ocean acidification. *Scientific Reports* **2014**, 4, 5207.
115. Venn, A.; Tambutté, E.; Holcomb, M.; Allemand, D.; Tambutté, S., Live Tissue Imaging Shows Reef Corals Elevate pH under Their Calcifying Tissue Relative to Seawater. *PLOS ONE* **2011**, 6 (5), e20013.

116. Wall, M.; Ragazzola, F.; Foster, L. C.; Form, A.; Schmidt, D. N., pH up-regulation as a potential mechanism for the cold-water coral *Lophelia pertusa* to sustain growth in aragonite undersaturated conditions. *Biogeosciences* **2015**, *12* (23), 6869-6880.
117. Al-Horani, F. A.; Al-Moghrabi, S. M.; de Beer, D., Microsensor study of photosynthesis and calcification in the scleractinian coral, *Galaxea fascicularis*: active internal carbon cycle. *Journal of Experimental Marine Biology and Ecology* **2003**, *288* (1), 1-15.
118. Marshall, A. T.; Clode, P. L.; Russell, R.; Prince, K.; Stern, R., Electron and ion microprobe analysis of calcium distribution and transport in coral tissues. *Journal of Experimental Biology* **2007**, *210* (14), 2453-2463.
119. Ramos-Silva, P.; Kaandorp, J.; Huisman, L.; Marie, B.; Zanella-Cleon, I.; Guichard, N.; Miller, D. J.; Marin, F., The skeletal proteome of the coral *Acropora millepora*: the evolution of calcification by co-option and domain shuffling. *Molecular biology and evolution* **2013**, *30* (9), 2099-112.
120. Drake, J. L.; Mass, T.; Haramaty, L.; Zelzion, E.; Bhattacharya, D.; Falkowski, P. G., Proteomic analysis of skeletal organic matrix from the stony coral *Stylophora pistillata*. *Proceedings of the National Academy of Sciences of the United States of America* **2013**, *110* (10), 3788-93.
121. Reggi, M.; Fermani, S.; Landi, V.; Sparla, F.; Caroselli, E.; Gizzi, F.; Dubinsky, Z.; Levy, O.; Cuif, J.-P.; Dauphin, Y.; Goffredo, S.; Falini, G., Biomineralization in Mediterranean Corals: The Role of the Intraskelatal Organic Matrix. *Crystal Growth & Design* **2014**, *14* (9), 4310-4320.
122. Falini, G.; Reggi, M.; Fermani, S.; Sparla, F.; Goffredo, S.; Dubinsky, Z.; Levi, O.; Dauphin, Y.; Cuif, J.-P., Control of aragonite deposition in colonial corals by intra-skeletal macromolecules. *Journal of Structural Biology* **2013**, *183* (2), 226-238.
123. Sancho-Tomas, M.; Fermani, S.; Goffredo, S.; Dubinsky, Z.; Garcia-Ruiz, J. M.; Gomez-Morales, J.; Falini, G., Exploring coral biomineralization in gelling environments by means of a counter diffusion system. *CrystEngComm* **2014**, *16* (7), 1257-1267.
124. Goffredo, S.; Vergni, P.; Reggi, M.; Caroselli, E.; Sparla, F.; Levy, O.; Dubinsky, Z.; Falini, G., The Skeletal Organic Matrix from Mediterranean Coral *Balanophyllia europaea* Influences Calcium Carbonate Precipitation. *PLOS ONE* **2011**, *6* (7), e22338.
125. Puverel, S.; Tambutte, E.; Pereira-Mouries, L.; Zoccola, D.; Allemand, D.; Tambutte, S., Soluble organic matrix of two Scleractinian corals: partial and comparative analysis. *Comparative biochemistry and physiology. Part B, Biochemistry & molecular biology* **2005**, *141* (4), 480-7.
126. Cuif, J. P.; Dauphin, Y.; Freiwald, A.; Gautret, P.; Zibrowius, H., Biochemical markers of zooxanthellae symbiosis in soluble matrices of skeleton of 24 Scleractinia species. *Comparative Biochemistry and Physiology Part A: Molecular & Integrative Physiology* **1999**, *123* (3), 269-278.
127. Young, S. D., Organic material from scleractinian coral skeletons—I. Variation in composition between several species. *Comparative Biochemistry and Physiology Part B: Comparative Biochemistry* **1971**, *40* (1), 113-120.
128. Mitterer, R. M., Amino Acid Composition and Metal Binding Capability of the Skeletal Protein of Corals. *Bulletin of Marine Science* **1978**, *28* (1), 173-180.
129. Constantz, B.; Weiner, S., Acidic macromolecules associated with the mineral phase of scleractinian coral skeletons. *Journal of Experimental Zoology* **1988**, *248* (3), 253-258.
130. De Yoreo, J. J.; Gilbert, P. U. P. A.; Sommerdijk, N. A. J. M.; Penn, R. L.; Whitelam, S.; Joester, D.; Zhang, H.; Rimer, J. D.; Navrotsky, A.; Banfield, J. F.; Wallace, A. F.; Michel, F. M.; Meldrum, F. C.; Cölfen, H.; Dove, P. M., Crystallization by particle attachment in synthetic, biogenic, and geologic environments. *Science (New York, N.Y.)* **2015**, *349* (6247).

131. Niederberger, M.; Colfen, H., Oriented attachment and mesocrystals: Non-classical crystallization mechanisms based on nanoparticle assembly. *Physical Chemistry Chemical Physics* **2006**, 8 (28), 3271-3287.
132. Jokiel, P. L.; Jury, C. P.; Kuffner, I. B., Coral Calcification and Ocean Acidification. In *Coral Reefs at the Crossroads*, Hubbard, D. K.; Rogers, C. S.; Lipps, J. H.; Stanley, J. G. D., Eds. Springer Netherlands: Dordrecht, 2016; pp 7-45.
133. Bhattacharya, D.; Agrawal, S.; Aranda, M.; Baumgarten, S.; Belcaid, M.; Drake, J. L.; Erwin, D.; Foret, S.; Gates, R. D.; Gruber, D. F.; Kamel, B.; Lesser, M. P.; Levy, O.; Liew, Y. J.; MacManes, M.; Mass, T.; Medina, M.; Mehr, S.; Meyer, E.; Price, D. C.; Putnam, H. M.; Qiu, H.; Shinzato, C.; Shoguchi, E.; Stokes, A. J.; Tambutté, S.; Tchernov, D.; Voolstra, C. R.; Wagner, N.; Walker, C. W.; Weber, A. P. M.; Weis, V.; Zelzion, E.; Zoccola, D.; Falkowski, P. G., Comparative genomics explains the evolutionary success of reef-forming corals. *eLife* **2016**, 5, e13288.
134. III. Microscopic and systematic study of madreporarian types of corals. *Philosophical Transactions of the Royal Society of London. Series B, Containing Papers of a Biological Character* **1896**, 187, 83-345.
135. Cuif, J.-P.; Dauphin, Y.; Doucet, J.; Salome, M.; Susini, J., XANES mapping of organic sulfate in three scleractinian coral skeletons. *Geochimica et Cosmochimica Acta* **2003**, 67 (1), 75-83.
136. Stolarski, J., Three-dimensional micro- and nanostructural characteristics of the scleractinian coral skeleton: A biocalcification proxy. *Acta Palaeontologica Polonica* **2003**, 48 (4), 497-530.
137. W. B. Bryan, D. H., *Spherulitic crystallization as a mechanism of skeletal growth in the hexacorals*. 1941; Vol. 2.
138. Cohen, A. L.; Layne, G. D.; Hart, S. R.; Lobel, P. S., Kinetic control of skeletal Sr/Ca in a symbiotic coral: Implications for the paleotemperature proxy. *Paleoceanography* **2001**, 16 (1), 20-26.
139. Cuif, J.-P.; Dauphin, Y., Microstructural and physico-chemical characterization of 'centers of calcification' in septa of some Recent scleractinian corals. *Paläontologische Zeitschrift* **1998**, 72 (3), 257-269.
140. Nehrke, G.; Nouet, J., Confocal Raman microscope mapping as a tool to describe different mineral and organic phases at high spatial resolution within marine biogenic carbonates: case study on *Nerita undata* (Gastropoda, Neritopsina). *Biogeosciences* **2011**, 8 (12), 3761-3769.
141. Wall, M.; Nehrke, G., Reconstructing skeletal fiber arrangement and growth mode in the coral *Porites lutea* (Cnidaria, Scleractinia): a confocal Raman microscopy study. *Biogeosciences* **2012**, 9 (11), 4885-4895.
142. Bonhomme, C.; Gervais, C.; Laurencin, D., Recent NMR developments applied to organic-inorganic materials. *Progress in Nuclear Magnetic Resonance Spectroscopy* **2014**, 77, 1-48.
143. Ben Shir, I.; Kababya, S.; Katz, I.; Pokroy, B.; Schmidt, A., Exposed and Buried Biomineral Interfaces in the Aragonitic Shell of *Perna canaliculus* Revealed by Solid-State NMR. *Chemistry of Materials* **2013**, 25 (22), 4595-4602.
144. Gertman, R.; Ben Shir, I.; Kababya, S.; Schmidt, A., In Situ Observation of the Internal Structure and Composition of Biomineralized *Emiliana huxleyi* Calcite by Solid-State NMR Spectroscopy. *Journal of the American Chemical Society* **2008**, 130 (40), 13425-13432.
145. Jager, C.; Colfen, H., Fine structure of nacre revealed by solid state ¹³C and ¹H NMR. *CrystEngComm* **2007**, 9 (12), 1237-1244.

146. Nassif, N.; Pinna, N.; Gehrke, N.; Antonietti, M.; Jäger, C.; Cölfen, H., Amorphous layer around aragonite platelets in nacre. *Proceedings of the National Academy of Sciences of the United States of America* **2005**, *102* (36), 12653-12655.
147. Seto, J.; Ma, Y.; Davis, S. A.; Meldrum, F.; Gourrier, A.; Kim, Y.-Y.; Schilde, U.; Sztucki, M.; Burghammer, M.; Maltsev, S.; Jäger, C.; Cölfen, H., Structure-property relationships of a biological mesocrystal in the adult sea urchin spine. *Proceedings of the National Academy of Sciences* **2012**, *109* (10), 3699-3704.
148. Takahashi, K.; Yamamoto, H.; Onoda, A.; Doi, M.; Inaba, T.; Chiba, M.; Kobayashi, A.; Taguchi, T.; Okamura, T.-a.; Ueyama, N., Highly oriented aragonite nanocrystal-biopolymer composites in an aragonite brick of the nacreous layer of *Pinctada fucata*. *Chemical Communications* **2004**, (8), 996-997.
149. Nebel, H.; Neumann, M.; Mayer, C.; Epple, M., On the Structure of Amorphous Calcium Carbonate—A Detailed Study by Solid-State NMR Spectroscopy. *Inorganic Chemistry* **2008**, *47* (17), 7874-7879.
150. Brown, E.; Rixen, T.; Kröger, R., Acicular building blocks in the corallites of *Porites lutea*. *Journal of Physics: Conference Series* **2010**, *241* (1), 012026.
151. Wang, L.; Sondi, I. I.; Matijevic, E., Preparation of Uniform Needle-Like Aragonite Particles by Homogeneous Precipitation. *Journal of colloid and interface science* **1999**, *218* (2), 545-553.
152. Sideris, P. J.; Nielsen, U. G.; Gan, Z.; Grey, C. P., Mg/Al Ordering in Layered Double Hydroxides Revealed by Multinuclear NMR Spectroscopy. *Science (New York, N.Y.)* **2008**, *321* (5885), 113-117.
153. Wehrmeister, U.; Jacob, D. E.; Soldati, A. L.; Loges, N.; Häger, T.; Hofmeister, W., Amorphous, nanocrystalline and crystalline calcium carbonates in biological materials. *Journal of Raman Spectroscopy* **2011**, *42* (5), 926-935.
154. Finch, A. A.; Allison, N., Mg structural state in coral aragonite and implications for the paleoenvironmental proxy. *Geophysical Research Letters* **2008**, *35* (8), n/a-n/a.
155. Meibom, A.; Cuif, J.-P.; Hillion, F.; Constantz, B. R.; Juillet-Leclerc, A.; Dauphin, Y.; Watanabe, T.; Dunbar, R. B., Distribution of magnesium in coral skeleton. *Geophysical Research Letters* **2004**, *31* (23), n/a-n/a.
156. Loste, E.; Wilson, R. M.; Seshadri, R.; Meldrum, F. C., The role of magnesium in stabilising amorphous calcium carbonate and controlling calcite morphologies. *Journal of Crystal Growth* **2003**, *254* (1), 206-218.
157. Raz, S.; Hamilton, P. C.; Wilt, F. H.; Weiner, S.; Addadi, L., The Transient Phase of Amorphous Calcium Carbonate in Sea Urchin Larval Spicules: The Involvement of Proteins and Magnesium Ions in Its Formation and Stabilization. *Advanced Functional Materials* **2003**, *13* (6), 480-486.
158. Mass, T.; Drake, J. L.; Peters, E. C.; Jiang, W.; Falkowski, P. G., Immunolocalization of skeletal matrix proteins in tissue and mineral of the coral *Stylophora pistillata*. *Proceedings of the National Academy of Sciences* **2014**, *111* (35), 12728-12733.
159. Kawaguti, S.; Sato, K., Electron microscopy on the polyp of staghorn corals with special reference to its skeleton formation. *Biological Journal of Okayama University* **1968**, *14*, 87-98.
160. HAYES, R. L.; GOREAU, N. I., INTRACELLULAR CRYSTAL-BEARING VESICLES IN THE EPIDERMIS OF SCLERACTINIAN CORALS, *ASTRANGIA DANA*E (AGASSIZ) AND *PORITES PORITES* (PALLAS). *The Biological Bulletin* **1977**, *152* (1), 26-40.
161. Hughes, T. P.; Baird, A. H.; Bellwood, D. R.; Card, M.; Connolly, S. R.; Folke, C.; Grosberg, R.; Hoegh-Guldberg, O.; Jackson, J. B. C.; Kleypas, J.; Lough, J. M.; Marshall, P.; Nyström, M.;

Palumbi, S. R.; Pandolfi, J. M.; Rosen, B.; Roughgarden, J., Climate Change, Human Impacts, and the Resilience of Coral Reefs. *Science (New York, N.Y.)* **2003**, *301* (5635), 929-933.

162. Penman, D. E.; Hönisch, B.; Zeebe, R. E.; Thomas, E.; Zachos, J. C., Rapid and sustained surface ocean acidification during the Paleocene-Eocene Thermal Maximum. *Paleoceanography* **2014**, *29* (5), 357-369.

163. Stanley, G. D., The evolution of modern corals and their early history. *Earth-Science Reviews* **2003**, *60* (3), 195-225.

164. Hoegh-Guldberg, O.; Mumby, P. J.; Hooten, A. J.; Steneck, R. S.; Greenfield, P.; Gomez, E.; Harvell, C. D.; Sale, P. F.; Edwards, A. J.; Caldeira, K.; Knowlton, N.; Eakin, C. M.; Iglesias-Prieto, R.; Muthiga, N.; Bradbury, R. H.; Dubi, A.; Hatziolos, M. E., Coral reefs under rapid climate change and ocean acidification. *Science (New York, N.Y.)* **2007**, *318* (5857), 1737-42.